Fast boundary element formulations for electromagnetic modelling in biological tissues

John Erick Ortiz Guzman

IMT Atlantique
Bretagne-Pays de la Loire
École Mines-Télécom

UNIVERSITE BRETAGNE LOIRE

THÈSE / IMT Atlantique

sous le sceau de l'Université Bretagne Loire

pour obtenir le grade de

DOCTEUR D'IMT Atlantique

Spécialité : Génie électrique

École Doctorale Mathématiques et STIC

Présentée par

John Erick Ortiz Guzman

Préparée dans le département Micro-ondes

Laboratoire Cerl

Fast Boundary Element Formulations for Electromagnetic Modelling in Biological Tissues

Thèse soutenue le 24 novembre 2017

devant le jury composé de :

Valérie Burdin
Professeur, IMT Atlantique / présidente

Jan Fostier
Professeur, Université de Gand - Belgique / rapporteur

Giuseppe Vecchi
Professeur, Politecnico di Torino - Italie / rapporteur

Guido Valerio
Maître de conférences, Université Pierre et Marie Curie / examinateur

François Rousseau
Professeur, IMT Atlantique / examinateur

Francesco Andriulli
Professeur, IMT Atlantique / directeur de thèse

a mi madre, quien me hizo ser lo que soy

Acknowledgements

After three years of PhD, I have many people in my mind without whom would not have been possible to reach this point.

First, I want to say thanks to my advisor, Francesco Andriulli, who inspired me with his passion for science. He was always willing to help me and to guide me in this scientific journey.

I arrived to France knowing no one, but with time I made really good friends. They listened all my crazy talks without running. To them, I say thanks. To Axelle, the craziest French friend that I made, by far. She gave me an unconditional support through all this time. To Johana, a friend like few, she has been always there, in the shiny moments and especially in the dark ones. To my bad influence, my roomie Marcia. The kindest person that I know and the cheerfullest as well. She made my life an eternal party. Thanks to Adrien, or as we know him the "dangerously silly" boy, even if he likes Linux. To Lyes, a really good friend that always gave me a hand with the scientific challenges. To the newbies in the lab, Maxime, Tiffany and Andrea.

But this journey started in Colombia, and I have many people in my country that made it possible. Thanks to my professor in Bogota, Javier Araque, he gave my first contact with science and thanks to him I could come to France. All my friends in Colombia always give me their support beyond the distance. Thanks to my good friends, Sebastian, Ambar and Nataly. With them I always

can be myself, without restrictions, without masks. Special thanks to my girlfriend, Natalia, for being always by my side no matter what. She gave me the strength to continue until the end.

Nothing of these would have been possible without the support of my family. Thanks to my mother, Alicia, the reason why I'm who I'm. She always has believed in me. To my father, Ignacio, thanks to him I always can see the bright side of the things. And to my brother, Oscar, thanks for being the best model that I could have had.

Abstract

This thesis presents several new techniques for rapidly converging boundary element solutions of electromagnetic problems. A special focus has been given to formulations that are relevant for electromagnetic solutions in biological tissues both at low and high frequencies. More specifically, as pertains the low-frequency regime, this thesis presents new schemes for preconditioning and accelerating the Forward Problem in Electroencephalography (EEG). The regularization strategy leveraged on a new Calderon formula, obtained in this thesis work, while the acceleration leveraged on an Adaptive-Cross-Approximation paradigm. As pertains the higher frequency regime, with electromagnetic dosimetry applications in mind, the attention of this work focused on the study and regularization of the Poggio-Miller-Chang-Harrington-Wu-Tsai (PMCHWT) integral equation via hierarchical techniques. In this effort, a complete analysis of the equation for both simply and non-simply connected geometries has been obtained. This allowed to design a new hierarchical basis regularization strategy to obtain an equation for penetrable media which is stable in a wide spectrum of frequencies. A final part of this thesis work presents a propaedeutic discretization framework and associated computational library for 2D Calderon research which will enable our future investigations in tomographic imaging.

This thesis is organized as follows: the first chapter presents some background material, sets the notation, and introduces the main EEG formulation ana-

lyzed here, the symmetric scheme, together with the PMCHWT integral equation. The symmetric formulation of EEG forward problem is a well-known and widespread equation thanks to the high level of accuracy that it delivers. However, this equation is first kind in nature and gives rise to ill-conditioned problems when the discretization density or the brain conductivity contrast increases, resulting in numerical instabilities and increasingly slow solutions, as this chapter will explain. As briefly delineated already, the PMCHWT integral equation is used to solve scattering problems involving penetrable media. The PMCHWT operator comprises the electric field integral operator (EFIO) and the magnetic field integral operator (MFIO) and, thereby, it inherits some of the properties of these operators. In particular, if the frequency or the average edge length of the mesh decreases, then the condition number of the system matrix of the discretized PMCHWT operator grows.

The second chapter presents a new regularized symmetric formulation for the EEG forward problem, which solves both high contrast conductivity and high mesh discretization, ill-conditioning problems. The new scheme is obtained by leveraging on Calderon identities which allow to introduce a dual symmetric equation that, combined with the standard one, results in a second kind operator, which is both stable and well-conditioned under all the above mentioned conditions. The new formulation presented can be easily integrated into existing EEG imaging packages since it can be obtained with the same computational technology required by the standard symmetric formulation. The performance of the new scheme is substantiated by both theoretical developments and numerical results which corroborate the theory and show the practical impact of the new technique.

In Chapter 3 the implementation of a fast solver for the Calderon-Symmetric

formulation is detailed. The fast solver is based on the Adaptive Cross Approximation (ACA), a kernel-free low-rank compression. This yields a storage and computational complexity of $O(N \log(N))$ (where N is the number of unknowns). The method is described in detail together with the impact of this fast solver on the Calderon-Symmetric formulation. Numerical results show the effectiveness of the algorithm for this case.

Chapter 4 analyses and solves the ill-conditioning problems of the PMCHWT. To this end, we first consider the direct application of hierarchical basis preconditioners, developed for the Electric Field Integral Equation (EFIE), to the PMCHWT. It is notably found that, whereas for the EFIE a diagonal preconditioner can be used for obtaining the hierarchical basis scaling factors, this strategy is catastrophic in the case of the PMCHWT since it leads to a severely ill-conditioned PMCHWT system in the case of multiply connected geometries. We then proceed to a theoretical analysis of the effect of hierarchical bases on the PMCHWT operator for which we obtain the correct scaling factors and a provably effective preconditioner for both low frequencies and mesh refinements. Numerical results will corroborate the theory and show the effectiveness of the new approach.

In Chapter 5 it is presented a propaedeutic discretization framework and associated computational library for 2D Calderon research which will enable our future investigations in tomographic imaging. To this end, we first define the EFIE operators in 2D for both polarizations, transverse magnetic (TM) and transverse electric (TE). Then, we present some different discretizations of the operators adapted to Calderon techniques on both standard and dual grids. The framework is validated by building all four primal/dual combination of Calderon preconditioners.

Chapter 6 presents some conclusions and avenues for future research.

Résumé

Dans cette thèse nous présentons de nouvelles méthodes permettant l'accélération de la résolution de différents problèmes électromagnétiques. Nos contributions se concentrent sur deux formulations spécifiques: la formulation symétrique pour le problème direct de l'électroencéphalographie (EEG) et la formulation intégrale Poggio-Miller-Chang-Harrington-Wu-Tsai (PMCHWT) utilisée pour modéliser la dispersion par des diélectriques, en particulier dans le domaine de la dosimétrie.

Dans le chapitre 1 nous établissons le contexte nécessaire à la compréhension de nos travaux. Nous commençons par présenter la méthode aux éléments de frontière (BEM), qui est l'une des principales méthodes numériques utilisées pour résoudre les équations integro-différentielles en n'utilisant que les frontières du domaine. Nous rappelons ensuite les équations de Maxwell et certaines de leurs dérivations. Dans le cas de problèmes statiques, pour lesquels les champs électriques et magnétiques sont découplés, nous utilisons l'équation de Poisson

$$\nabla \cdot (\sigma \nabla V) = \nabla \cdot \mathcal{J}_i. \tag{1}$$

Dans le domaine fréquentiel nous dérivons les équations d'onde

$$\nabla \times \nabla \times \mathbf{E} - k^2 \mathbf{E} = -jk\eta \mathbf{J} \tag{2a}$$

$$\nabla \times \nabla \times \mathbf{H} - k^2 \mathbf{H} = \nabla \times \mathbf{J}. \tag{2b}$$

L'équation (1) est utilisée pour résoudre le problème direct de l'EEG. Nous présentons trois des méthodes existantes permettant de résoudre ce problème, les formulations *simple*

couche, *double couche* et *symétrique*. Les équations (2) sont utilisées pour la dérivation de l'équation PMCHWT.

Une solution aux problèmes de mauvais conditionnement, liés au contraste de conductivité élevé et à la finesse de discrétisation, de la formulation symétrique est proposée dans le chapitre 2. Les équations de la formulation symétrique sont

$$\sigma_{i+1}^{-1}\left(v_{i+1}\right)_{\Gamma_i} - \sigma_i^{-1}\left(v_i\right)_{\Gamma_i} = D_{i,i-1}V_{i-1} - 2D_{ii}V_i + D_{i,i+1}V_{i+1} \\ - \sigma_i^{-1}S_{i,i-1}p_{i-1} + \left(\sigma_i^{-1} + \sigma_{i+1}^{-1}\right)S_{ii}p_i - \sigma_{i+1}^{-1}S_{i,i+1}p_{i+1} \quad (3)$$

et

$$\left(\partial_n v_{i+1}\right)_{\Gamma_i} - \left(\partial_n v_i\right)_{\Gamma_i} = \sigma_i N_{i,i-1}V_{i-1} - \left(\sigma_i + \sigma_{i+1}\right)N_{ii}V_i + \sigma_{i+1}N_{i,i+1}V_{i+1} \\ - D_{i,i-1}^{*}p_{i-1} + 2D_{ii}^{*}p_i - D_{i,i+1}^{*}p_{i+1} \quad (4)$$

où les opérateurs D, D^*, S et N sont définis comme suit

$$(D\Phi)(r) = \int_{\partial\Omega} \partial_{n'}G(r,r')\Phi(r')dr' \ , \ D : H^{1/2} \to H^{1/2} \quad (5a)$$

$$(S\Psi)(r) = \int_{\partial\Omega} G(r,r')\Psi(r')dr' \ , \ S : H^{-1/2} \to H^{1/2} \quad (5b)$$

$$(N\Phi)(r) = \int_{\partial\Omega} \partial_n\partial_{n'}G(r,r')\Phi(r')dr' \ , \ N : H^{1/2} \to H^{-1/2} \quad (5c)$$

$$(D^*\Psi)(r) = \int_{\partial\Omega} \partial_n G(r,r')\Phi(r')dr' \ , \ D^* : H^{-1/2} \to H^{-1/2}. \quad (5d)$$

À partir de ces équations nous pouvons définir l'opérateur symétrique

$$Z = \begin{bmatrix} \alpha_1 N_{11} & -2D_{11}^{*} & -\sigma_2 N_{12} & D_{12}^{*} & & & & \\ -2D_{11} & \beta_1 S_{11} & D_{12} & -\sigma_2^{-1}S_{12} & & & & \\ -\sigma_2 N_{21} & D_{21}^{*} & \alpha_2 N_{22} & -2D_{22}^{*} & \cdots & & & \\ D_{21} & -\sigma_2^{-1}S_{21} & -2D_{22} & \beta_2 S_{22} & \cdots & & & \\ & & \vdots & \vdots & \ddots & & & \\ & & & & & \alpha_{N-1}N_{N-1,N-1} & 2D_{N-1,N-1}^{*} & -\sigma_N N_{N-1,N} \\ & & & & & -2D_{N-1,N-1} & \beta_{N-1}S_{N-1,N-1} & D_{N-1,N} \\ & & & & & -\sigma_N N_{N,N-1} & D_{N,N-1} & \sigma_N N_{N,N} \end{bmatrix} \quad (6)$$

En utilisant les identités de Calderón nous pouvons construire un préconditionneur de Calderón

$$C = \begin{bmatrix} c_{11}S_{11} & c_{12}D_{11} & c_{13}S_{12} & c_{14}D_{12} & 0 & 0 & 0 \\ c_{21}D^*_{11} & c_{22}N_{11} & c_{23}D^*_{12} & c_{24}N_{12} & 0 & 0 & 0 \\ c_{31}S_{21} & c_{32}D_{21} & c_{33}S_{22} & c_{34}D_{22} & c_{35}S_{23} & c_{36}D_{23} & 0 \\ c_{41}D^*_{21} & c_{42}N_{21} & c_{43}D^*_{22} & c_{44}N_{22} & c_{45}D^*_{23} & c_{46}N_{23} & 0 \\ 0 & 0 & c_{53}S_{32} & c_{54}D_{32} & c_{55}S_{33} & c_{56}D_{33} & \cdots \\ 0 & 0 & c_{63}D^*_{32} & c_{64}N_{32} & c_{65}D^*_{33} & c_{66}N_{33} & \cdots \\ 0 & 0 & 0 & 0 & \vdots & \vdots & \ddots \end{bmatrix}, \tag{7}$$

où les coefficients constants c_{ij} représentant les conductivités sont les mêmes que dans (6). En multipliant C et Z nous obtenons un opérateur du second ordre, qui est donc bien conditionné par rapport à la finesse de discrétisation.

Cependant, le conditionnement de CZ dépend toujours du contraste de conductivité. Une solution pour ce problème est de régulariser l'opérateur Z et son préconditionneur C par rapport aux conductivités en utilisant un opérateur diagonal Q dont les éléments Q_{ii} sont

$$\begin{cases} Q_{ii} = \dfrac{1}{\sqrt{max(\sigma_i, \sigma_{i+1})}} & \text{si } i \text{ est impair} \\ Q_{ii} = \sqrt{min(\sigma_i, \sigma_{i+1})} & \text{si } i \text{ est pair} \end{cases} \tag{8}$$

Après avoir discretisé l'opérateur Z dans le maillage d'origine et le préconditionneur C dans le maillage dual, la matrice Calderon-Symétrique est

$$\mathbf{Z}_c = \mathbf{Q}\tilde{\mathbf{C}}\mathbf{Q}\mathbf{G}^{-1}\mathbf{Q}\mathbf{Z}\mathbf{Q}, \tag{9}$$

où $\mathbf{G}$ est la matrice de Gram faisant le lien entre les deux discrétisations. Les termes de cette matrice sont

$$[\mathbf{G}_{2i-1}]_{kl} = \int_{\mu_{\tilde{P}_{1k}}} (\tilde{P_{0l}})\, P_{1k}(r) dr \tag{10a}$$

$$[\mathbf{G}_{2i}]_{kl} = \int_{t_k} (\tilde{P_{1l}})\, P_{0k}(r) dr. \tag{10b}$$

La nouvelle formulation de Calderon, régularisée et symétrique, est, dans un premier temps, testée dans le cas de trois sphères homogènes, concentriques et de rayons respectifs

0.8, 0.9 et 1. Les conductivités normalisées des trois différents domaines sont respectivement 1, 0.0125 et 1. Nous commençons par vérifier que la précision est conservée après application du préconditionneur, comme illustrée dans les figures 1 et 2. Nous vérifions

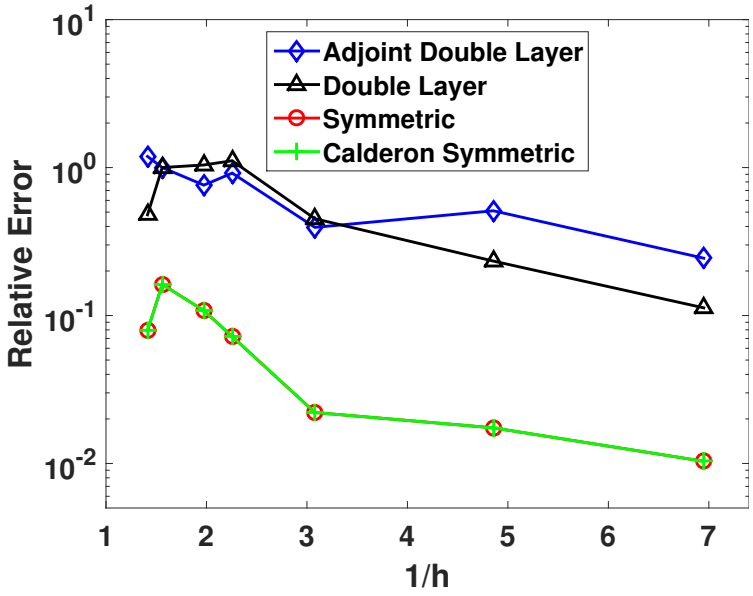

Figure 1: Erreur relative en fonction de la finesse de discrétisation. h est la longueur moyenne des cellules.

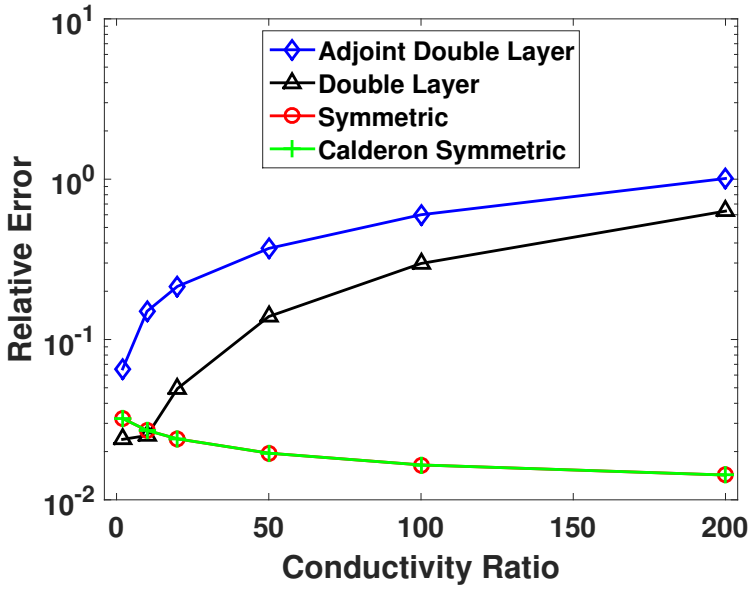

Figure 2: Erreur relative en fonction du ratio de conductivité σ_r.

ensuite le bon conditionnement de la nouvelle formulation. Les figures 3 et 4 représentent

le conditionnement en fonction de la finesse de discrétisation et du ratio de conductivité. Dans les deux cas le conditionnement reste constant pour notre formulation. Enfin, la

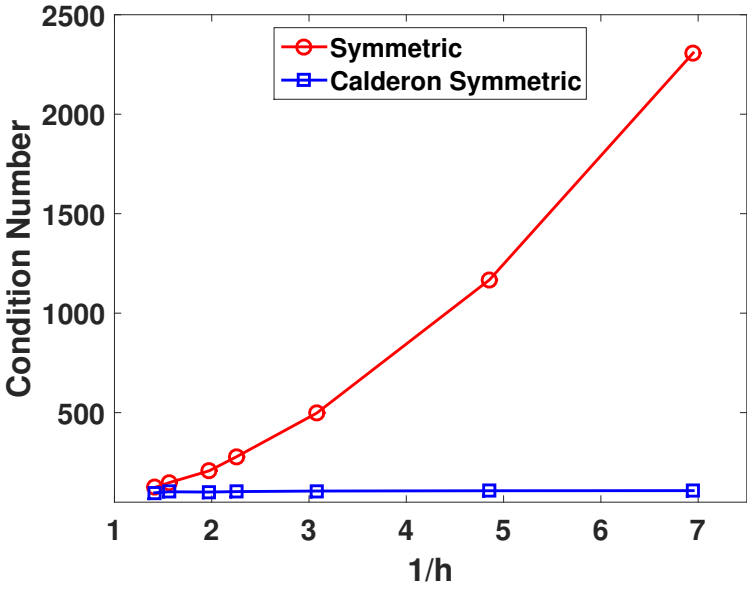

Figure 3: Conditionnement en fonction de la finesse de discrétisation.

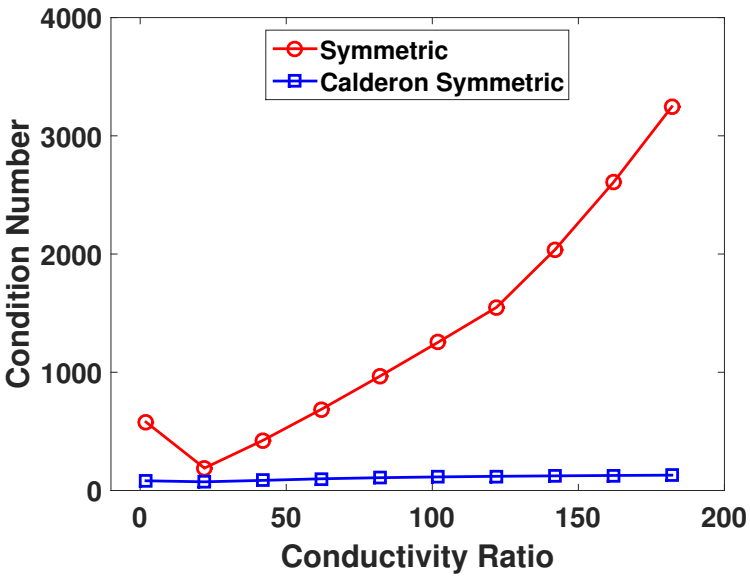

Figure 4: Conditionnement en fonction du ratio de conductivité σ_r.

nouvelle formulation est testée dans un cas réaliste en utilisant le modèle de tête obtenu à partir de données IRM illustré en figure 5. Une étude comparative de la convergence des formulations symétrique et Calderón-Symétrique est présentée en figure 6. Nous pouvons

constater la convergence rapide de la formulation préconditionnée qui démontre son bon conditionnement.

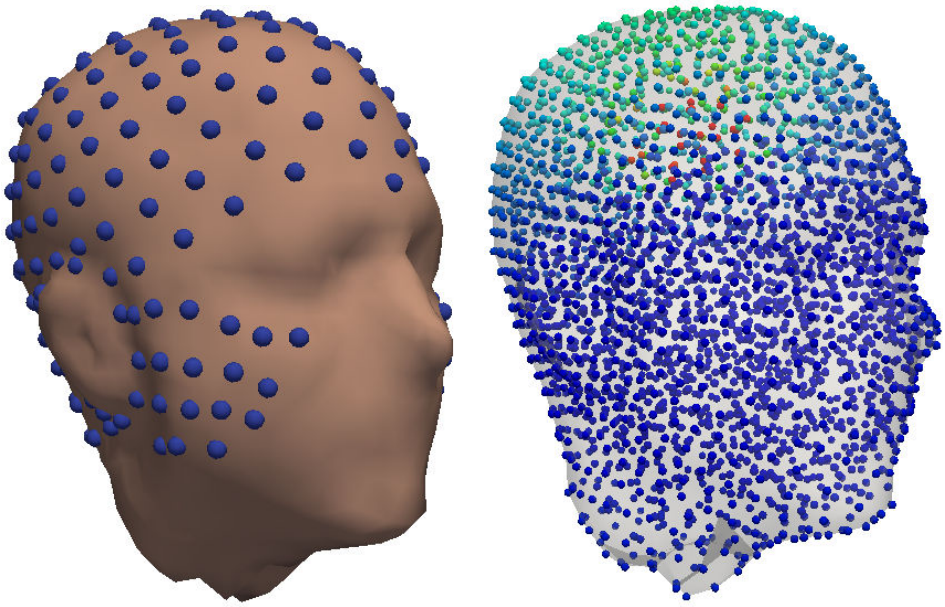

(a) Modèle de tête et positions des électodes de l'EEG.

(b) Potentiels électriques calculés.

Figure 5: Modèle de tête obtenu à partir de données IRM.

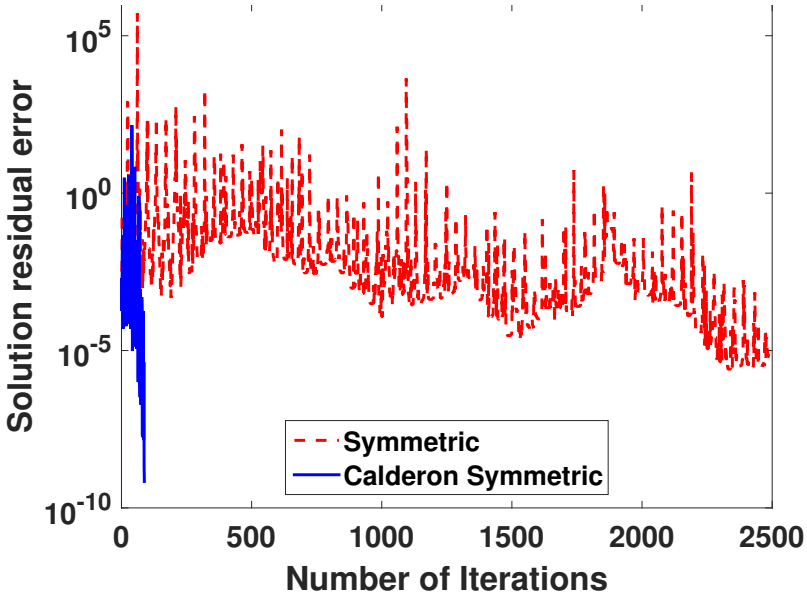

Figure 6: Convergence du solveur itératif pour les approches symétriques préconditionnée et non préconditionnée.

Méthode	Mémoire (Go)	Opérateur Temps (s)	Solution Temps (s)	Leadfield Temps (h)
Inv. Directe Symétrique dense	16.234	10845.67	54609.99	18.19
CGS Symétrique Dense	16.234	10845.67	7294.61	45.56
CGS Symétrique Compressée	1.254	1436.63	2322.89	13.95
CGS Calderon-Symétrique Compressée	2.542	7888.86	62.40	2.56

Table 1: Information sur la mémoire et temps de calcul nécessaire à la génération d'une matrice de *leadfield* en utilisant la méthode par réciprocité.

Dans le chapitre 3 nous présentons une technique rapide de résolution de la formulation Calderón-Symétrique. Cette technique est basée sur la méthode «adaptive cross approximation » (ACA) qui est basée sur une méthode, indépendante du noyau, de compression de matrice à faible rang. Cette technique permet d'atteindre une complexité algorithmique en $O(N\log(N))$ (où N est le nombre d'inconnues). Pour vérifier l'efficacité de la technique rapide combinée à la formulation Calderón-Symétrique, nous avons simulé un modèle de tête très détaillé contenant le scalp, le crâne et le cerveau respectivement discrétisés avec 11850, 11616 et 22948 triangles. À partir de ce modèle nous avons construit une matrice de *leadfield* faisant correspondre 1500 dipôles à 21 électrodes en utilisant le théorème de réciprocité. La table 1 présente, dans quatre cas différents, le temps nécessaire au calcul de l'opérateur, à la résolution du problème direct et au calcul du *leadfield* complet. Nous pouvons constater que, bien que le temps de calcul de l'opérateur Calderón-Symétrique est plus important que pour l'opérateur symétrique compressé, la vitesse de convergence de la méthode proposée permet le calcul du *leadfield* complet en 2.56 h, soit dix fois plus rapidement que sans préconditionnement. Cela compense largement la surcharge calculatoire causée par le calcul du préconditionneur.

Dans le chapitre 4 nous présentons une stratégie de préconditionnement du PMCHWT s'appuyant sur l'utilisation de bases hiérarchiques, prenant en compte aussi bien les géométries

à connection simple et à connexions multiples. L'opérateur PMCHWT est donné par

$$Z = \begin{bmatrix} \mathcal{T}_i^k/\eta_i + \mathcal{T}_o^k/\eta_o & -(\mathcal{K}^{k_i} + \mathcal{K}_o^k) \\ (\mathcal{K}_i^k + \mathcal{K}_o^k) & \eta_i \mathcal{T}^{k_i} + \eta_o \mathcal{T}_o^k, \end{bmatrix}$$

avec

$$\begin{aligned} \mathcal{T}^\kappa &= \mathrm{i}\kappa \mathcal{T}_\mathrm{A}^\kappa + 1/(\mathrm{i}\kappa)\mathcal{T}_\Phi^\kappa \\ \mathcal{T}_\mathrm{A}^\kappa \boldsymbol{f} &= \hat{\boldsymbol{n}} \times \int_\Gamma G(\boldsymbol{r}, \boldsymbol{r}')\boldsymbol{f}(\boldsymbol{r}')\mathrm{d}S(\boldsymbol{r}') \\ \mathcal{T}_\Phi^\kappa \boldsymbol{f} &= -\hat{\boldsymbol{n}} \times \nabla_\Gamma \int_\Gamma G(\boldsymbol{r}, \boldsymbol{r}')\nabla'_\Gamma \cdot \boldsymbol{f}(\boldsymbol{r}')\mathrm{d}S(\boldsymbol{r}'), \\ \mathcal{K}^\kappa \boldsymbol{f} &= -\hat{\boldsymbol{n}} \times \int_\Gamma \nabla_\Gamma G(\boldsymbol{r}, \boldsymbol{r}') \times \boldsymbol{f}(\boldsymbol{r}')\mathrm{d}S(\boldsymbol{r}'), \end{aligned}$$

Après discrétisation avec des fonctions RWG, nous obtenons la matrice du PMCHWT

$$\mathbf{Z} = \begin{bmatrix} \mathcal{T}_i^k/\eta_i + \mathcal{T}_o^k/\eta_o & -(\mathcal{K}^{k_i} + \mathcal{K}_o^k) \\ (\mathcal{K}_i^k + \mathcal{K}_o^k) & \eta_i \mathcal{T}^{k_i} + \eta_o \mathcal{T}_o^k. \end{bmatrix} \tag{11}$$

Pour régulariser le mauvais conditionnement dû aux basses fréquences et aux fines discrétisations nous multiplions $\mathbf{Z}$ à droite et à gauche par un préconditionneur hiérarchique

$$\boldsymbol{L}^\mathrm{T} \boldsymbol{Z} \boldsymbol{R} \boldsymbol{y} = \boldsymbol{L}^\mathrm{T} [\boldsymbol{h}; \boldsymbol{e}], \quad \text{avec } \boldsymbol{j} = \boldsymbol{R}\boldsymbol{y}\,. \tag{12}$$

où $\boldsymbol{L}$ et $\boldsymbol{R}$ sont définis comme suit:

$$\boldsymbol{L} = [\mathrm{diag}(\boldsymbol{L}_k, \boldsymbol{L}_k)], \quad \boldsymbol{R} = [\mathrm{diag}(\boldsymbol{R}_k \boldsymbol{R}_k)], \tag{13}$$

avec

$$\begin{aligned} \boldsymbol{L}_k &= \left[\boldsymbol{H}_\Lambda \boldsymbol{D}_{\hat{\boldsymbol{H}}^\Lambda}/\sqrt{k} \quad \boldsymbol{H}_\mathrm{qH}\sqrt{\beta} \quad i\boldsymbol{H}_\Sigma \boldsymbol{D}_{\hat{\boldsymbol{\Sigma}}}\sqrt{k} \right] \\ \boldsymbol{R}_k &= \left[\boldsymbol{H}_\Lambda \boldsymbol{D}_{\hat{\boldsymbol{H}}^\Lambda}/\sqrt{k} \quad \boldsymbol{H}_\mathrm{qH}\sqrt{\alpha} \quad i\boldsymbol{H}_\Sigma \boldsymbol{D}_{\hat{\boldsymbol{\Sigma}}}\sqrt{k} \right]. \end{aligned}$$

Le comportement fréquentiel de l'équation préconditionnée est alors

$$\boldsymbol{L}^\mathrm{T} \boldsymbol{Z} \boldsymbol{R} = \begin{bmatrix} 1 & \sqrt{\alpha}\sqrt{k} & k & k & k\sqrt{k}\sqrt{\alpha} & 1 \\ \sqrt{\beta}\sqrt{k} & \sqrt{\alpha\beta}k & \sqrt{\beta}k\sqrt{k} & \sqrt{\beta}k\sqrt{k} & \sqrt{\alpha\beta} & \sqrt{\beta}\sqrt{k} \\ k & k\sqrt{k}\sqrt{\alpha} & 1 & 1 & \sqrt{k}\sqrt{\alpha} & k \\ k & k\sqrt{k}\sqrt{\alpha} & 1 & 1 & \sqrt{k}\sqrt{\alpha} & k \\ \sqrt{\beta}k\sqrt{k} & \sqrt{\alpha\beta} & \sqrt{\beta}\sqrt{k} & \sqrt{\beta}\sqrt{k} & \sqrt{\alpha\beta}k & \sqrt{\beta}k\sqrt{k} \\ 1 & \sqrt{k}\sqrt{\alpha} & k & k & k\sqrt{k}\sqrt{\alpha} & 1 \end{bmatrix} \tag{14}$$

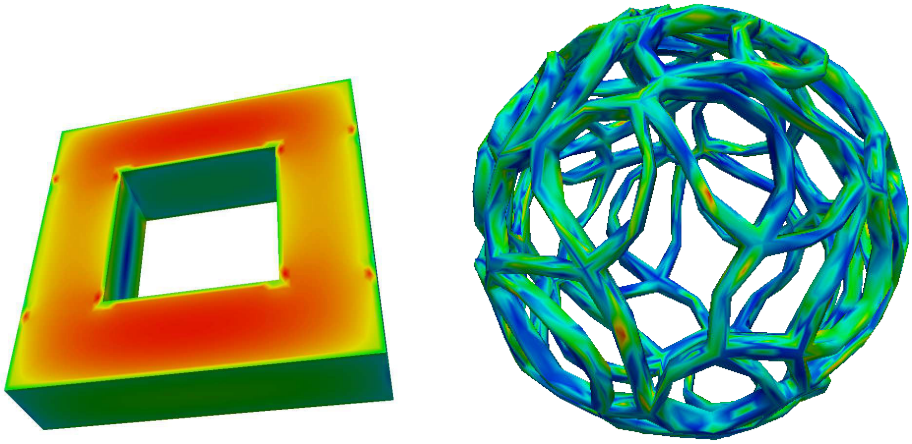

(a) Structure toroïdale: $g = 1$ (b) 136 boucles globales ($g = 68$)

Figure 7: Partie réelle du courant dans des géométries de test.

et le comportement fréquentiel du courant et de l'excitation est

$$\begin{aligned} \boldsymbol{R}^{-1}\left[\boldsymbol{j};\boldsymbol{m}\right]^{\mathrm{T}} &= \left[\sqrt{k} \quad k/\sqrt{\alpha} \quad \sqrt{k} \quad \sqrt{k} \quad k/\sqrt{\alpha} \quad \sqrt{k}\right]^{\mathrm{T}} \\ \boldsymbol{L}\left[\boldsymbol{h};\boldsymbol{e}\right]^{\mathrm{T}} &= \left[\sqrt{k} \quad k\sqrt{\beta} \quad \sqrt{k} \quad \sqrt{k} \quad k\sqrt{\beta} \quad \sqrt{k}\right]^{\mathrm{T}}. \end{aligned} \tag{15}$$

Plusieurs choix sont possibles pour les valeurs de α et β, cependant les contraintes suivantes sont imposées par les comportements fréquentiels: (i) $\alpha = 1/\beta$ pour éviter le mauvais conditionnement des blocs hors diagonale (éléments $(2,5)$ et $(5,2)$). (ii) α et β ne doivent pas croître plus rapidement que $O(1/k)$. Deux valeurs particulières de α et β sont mises en évidence par cette analyse: (a) $\alpha = 1/\beta = k$ qui permet un comportement fréquentiel homogène en $O(\sqrt{k})$, à la fois pour la solution et pour l'excitation, et (b) $\alpha = \beta = 1$ qui donne lieu à un comportement fréquentiel symétrique de la matrice préconditionnée. Par la suite nous choisirons (b) car, dans ce cas, $\mathbf{L}$ et $\mathbf{R}$ sont égales, ce qui permet de réduire la quantité de mémoire nécessaire au stockage du préconditionneur. L'autre choix est cependant tout aussi valable.

Dans un premier temps nous testons le nouveau préconditionneur hiérarchique dans le cas d'une structure avec deux boucles globales (illustrée en figure 7a) avec une permittivité $\varepsilon_{\mathrm{r}} = 3$ et un diamètre maximal de 2.8 m. Dans les figures 9 et 8 nous présentons une comparaison du conditionnement en fonction de la fréquence et de l'indice spectral

$1/h$ de la nouvelle formulation avec un préconditionneur *loop-star* et un préconditionneur hiérarchique naïf. Nous constatons que seule la nouvelle formulation est bien conditionnée dans les deux cas.

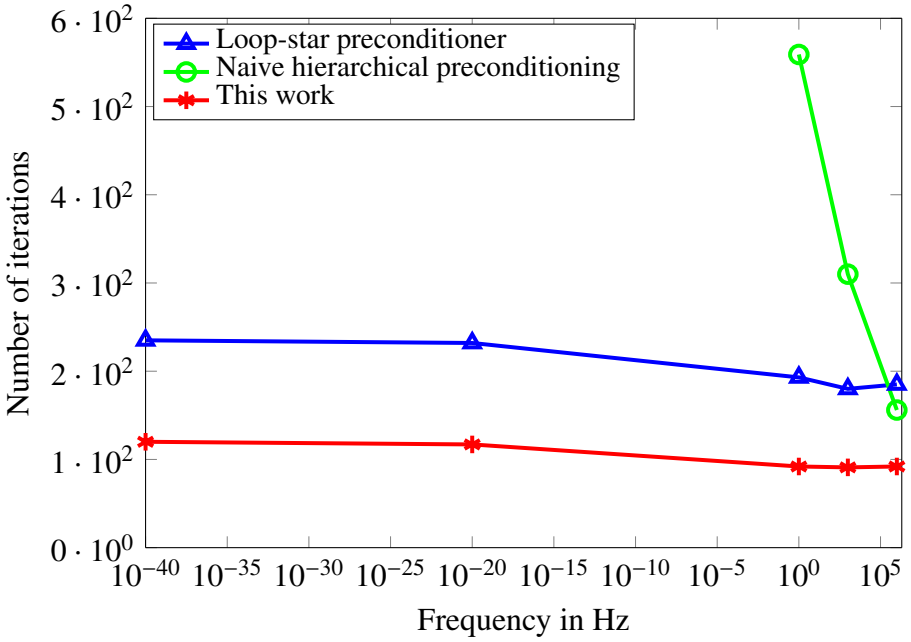

Figure 8: Structure toroïdale: nombre d'itérations en fonction de la fréquence.

Dans un second temps nous avons vérifié l'applicabilité de cette méthode à des modèles biologiques comme les scalp et le crâne illustrés en Figure 10a et Figure 10b. Dans les Figures 11 et 12 nous comparons, pour le scalp et le crâne, la vitesse de convergence de notre formulation à celle de formulations préconditonnées avec une méthode *loop-star* et avec préconditionneur hiérarchique naïf. Dans le cas du scalp la vitesse de convergence de notre formulation et des formulations traditionnelles sont les mêmes, à cause de l'absence de sous-espace harmonique. Cependant dans le cas du crâne, qui possède deux boucles globales, notre méthode converge le plus rapidement.

Pour vérifier l'efficacité de notre approche en présence d'un sous espace harmonique de grande dimension, nous avons testé notre nouvelle formulation sur la structure à connexions multiples illustrée en figure 7b, composée de 136 boucles globales et de 2.7 m de

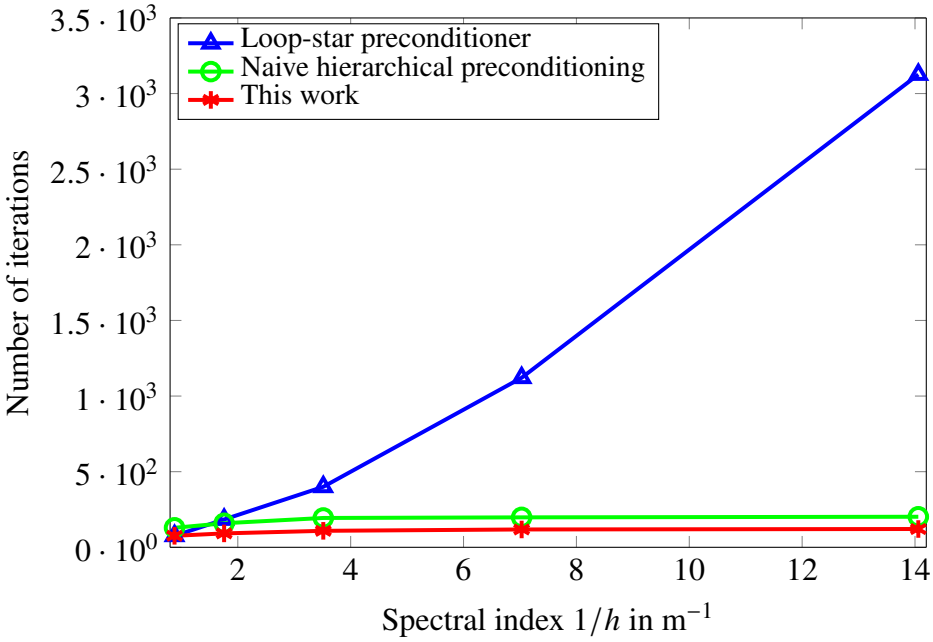

Figure 9: Structure toroïdale: nombre d'itérations en fonction de l'indice spectral $1/h$.

rayon. Une onde plane à 1 MHz a été utilisée comme excitation. Les résultats de cette simulation sont présentés dans la table 2. Notre technique a un avantage substantiel par rapport aux techniques *loop-star* standards même si nous n'avons utilisé qu'un seul niveau de raffinement dyadique. Cela confirme donc numériquement la stabilité de la formulation lorsqu'elle est appliquée à un sous espace harmonique.

Formulation	Itérations	Temps
Préconditionneur *loop-star*	5396	52h 1'22"
Préconditionneur hiérarchique naïf	18318	$\gg$ 100h
Notre formulation	2642	21h 6'5"

Table 2: Structure composée de 136 boucles globales: nombre d'itérations pour les différentes formulations avec une tolérance du solveur de 1×10^{-6}

Dans le dernier chapitre nous présentons une librairie permettant l'étude de problèmes électromagnétiques en deux dimensions. En utilisant cette librairie nous avons produit des résultats préliminaires pour le préconditionnement de l'EFIE en deux dimensions (2D) basé sur les identités de Calderón. Les opérateurs de l'EFIE en 2D pour les polarisations TE et

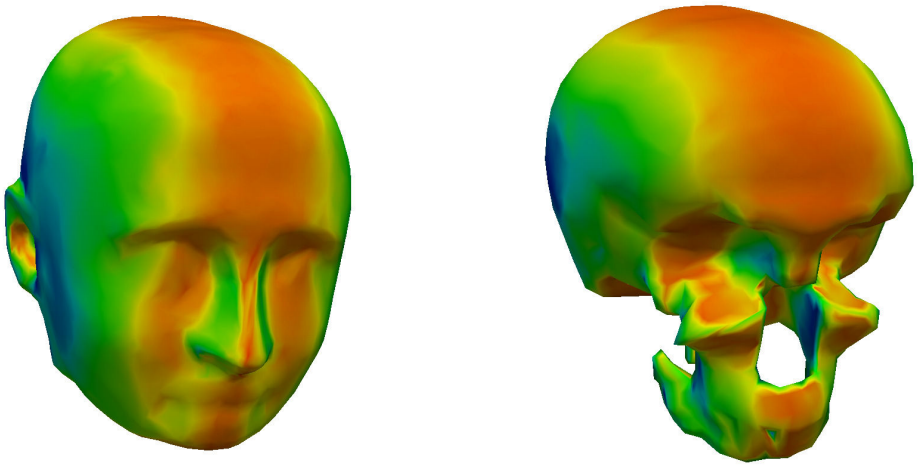

(a) Head model: $g = 0$ (b) Skull model : $g = 1$

Figure 10: Modèles biologiques avec une partie réelle de la densité du courant électrique.

TM sont définis comme suit

$$\begin{aligned}(T^{TM} J_z)(\boldsymbol{\rho}) &= \frac{k_0 \eta}{4} \int_\Gamma H_0^{(2)}(k_0|\boldsymbol{\rho} - \boldsymbol{\rho}'|) J_z(\boldsymbol{\rho}') d\boldsymbol{\rho}' \\ (T^{TE} J_t)(\boldsymbol{\rho}) &= \frac{k_0 \eta}{4} \hat{t} \cdot \int_C H_0^{(2)}(k_0|\boldsymbol{\rho} - \boldsymbol{\rho}'|) \hat{t}' J_t(\boldsymbol{\rho}') d\boldsymbol{\rho}' \\ &\quad + \frac{\eta}{4k_0} \hat{t} \cdot \nabla \int_C \nabla' \cdot [\hat{t}' J_t(\boldsymbol{\rho}')] H_0^{(2)}(k_0|\boldsymbol{\rho} - \boldsymbol{\rho}'|) d\boldsymbol{\rho}'.\end{aligned} \tag{16}$$

En utilisant les fonctions continues par partie P^0, les fonctions triangle P^1 et les fonctions $\tilde{P}^0$ et $\tilde{P}^1$ respectivement duales de P^0 et P^1, nous discrétisons les opérateurs ci-dessus de la façon suivante:

$$\mathbf{T}_0^{TM} = \langle P^0, T^{TM}(P^0) \rangle \tag{17a}$$

$$\mathbf{T}_1^{TM} = \langle P^1, T^{TM}(P^1) \rangle \tag{17b}$$

$$\tilde{\mathbf{T}}_0^{TM} = \langle \tilde{P}^0, T^{TM}(\tilde{P}^0) \rangle \tag{17c}$$

$$\tilde{\mathbf{T}}_1^{TM} = \langle \tilde{P}^1, T^{TM}(\tilde{P}^1) \rangle \tag{17d}$$

$$\mathbf{T}_1^{TE} = \langle P^1, T^{TE}(P^1) \rangle \tag{17e}$$

$$\tilde{\mathbf{T}}_1^{TE} = \langle \tilde{P}^1, T^{TE}(\tilde{P}^1) \rangle. \tag{17f}$$

Enfin nous utilisons la deuxième identité de Calderón pour construire quatre opérateurs

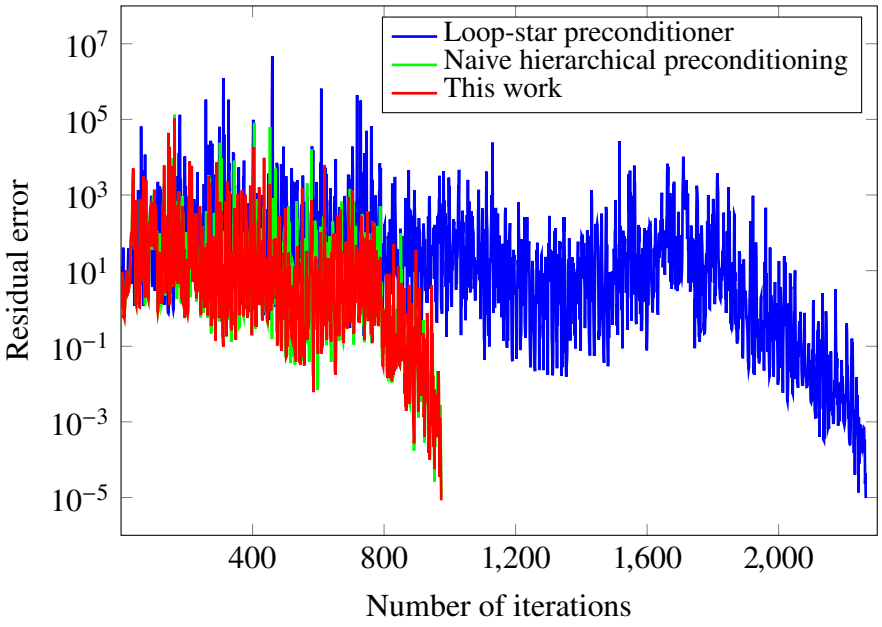

Figure 11: Head model: Residual error of the iterative solver.

bien conditionnés

$$\mathbf{T}_C^{TM} = \mathbf{T}_1^{TE}\mathbf{G}_{11}^{-1}\mathbf{T}_1^{TM} \tag{18a}$$

$$\tilde{\mathbf{T}}_C^{TM} = \tilde{\mathbf{T}}_1^{TE}\mathbf{G}_{0\tilde{1}}^{-1}\mathbf{T}_0^{TM} \tag{18b}$$

$$\mathbf{T}_C^{TE} = \mathbf{T}_1^{TM}\mathbf{G}_{11}^{-1}\mathbf{T}_1^{TE} \tag{18c}$$

$$\tilde{\mathbf{T}}_C^{TE} = \tilde{\mathbf{T}}_0^{TM}\mathbf{G}_{1\tilde{0}}^{-1}\mathbf{T}_1^{TE}, \tag{18d}$$

où les matrices de Gram $\mathbf{G}$ faisant le lien entre les discrétisations standards et duales sont calculées comme suit

$$\mathbf{G}_{11} = \langle P^1, P^1 \rangle \tag{19a}$$

$$\mathbf{G}_{0\tilde{1}} = \langle P^0, \tilde{P}^1 \rangle \tag{19b}$$

$$\mathbf{G}_{1\tilde{0}} = \langle P^1, \tilde{P}^0 \rangle \tag{19c}$$

Nous testons les opérateurs préconditionnés sur un cylindre infini dans la direction z et de rayon 1 m. La longueur d'onde est fixée à $\lambda = 2\pi/3$. Le contour de la coupe transversale est discrétisé avec différents niveaux de raffinement h. Le conditionnement de l'opérateur

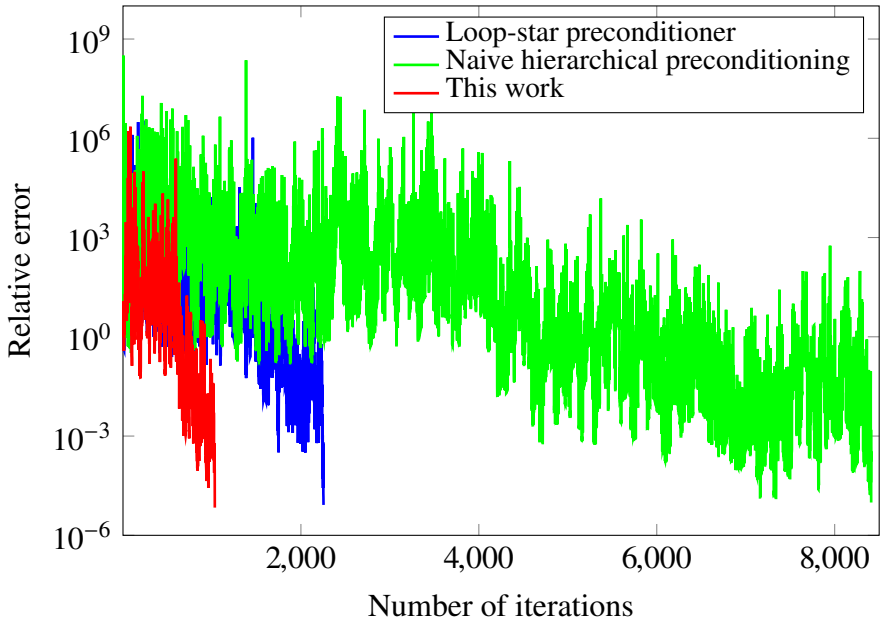

Figure 12: Skull model: Residual error of the iterative solver

non préconditionné croît avec $O(1/h)$ alors qu'il est constant pour les opérateurs préconditionnés avec Calderón. Les conditionnements des opérateurs TM et TE sont respectivement illustrés dans les figures 13 et 14, pour différents niveaux de raffinement.

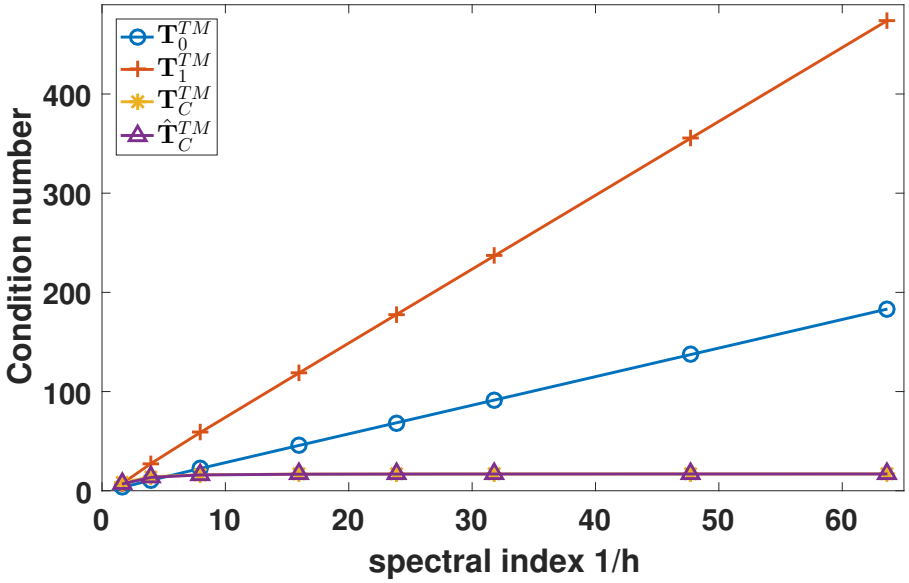

Figure 13: Conditionnement des opérateurs TM quand le maillage est rafiné.

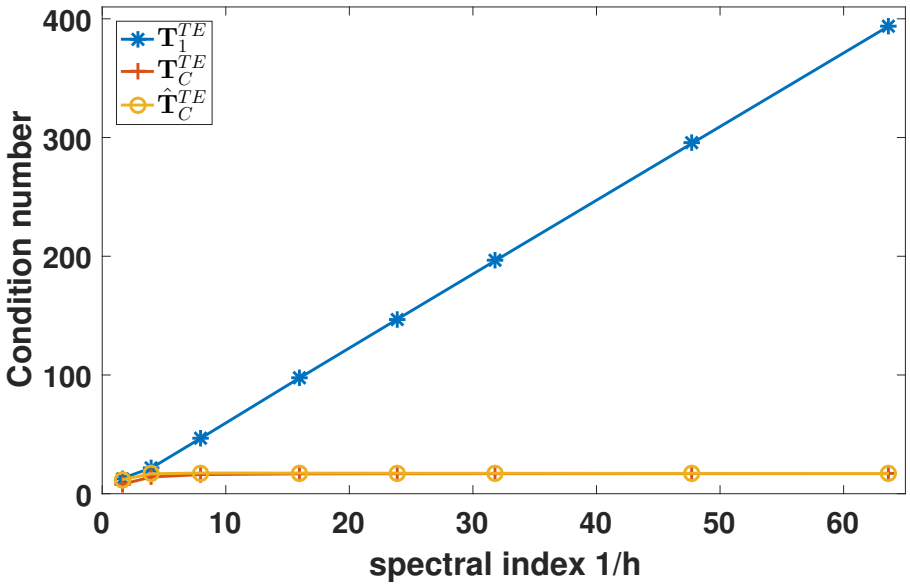

Figure 14: Conditionnement des opérateurs TE quand le maillage est rafiné.

Contents

List of Figures

Chapter 1

Introduction

This chapter introduces the background in solving electromagnetic problems with numerical methods, which is necessary to understand the work presented in this manuscript. A review of the boundary element method (BEM) is presented. Some basic concepts are introduced in order to set up the notation that will be used later on. The investigation treats static and high frequencies problems, especially formulations that are relevant for electromagnetic solutions in biological tissues both at low and high frequencies. Hence, a general review of both static and high frequency cases is presented. Moreover, two specific problems for each case are introduced in order to set the basic concepts for later chapters.

1.1 Boundary element method

Numerical solutions for integro-differential equations have had an important impact in the progress of engineering and science since the invention of the computers. The fast development of the technology has allowed to solve all kinds of physical problems, in particular, electromagnetic (EM) problems. The boundary element method is a numerical technique to solve linear equations using only the boundary of the structure. Therefore, the number of unknowns is reduced, in consequence the computational cost is decreased. We present the basic idea of this method.

Let Ω be a domain in R^d, with a smooth boundary $\Gamma = \partial\Omega$. We seek to solve the

equation

$$Lf = b \tag{1.1}$$

where b is a known function, f is the unknown function and L is a linear operator defined as

$$(Lf)(r) = \int_{\Gamma} f(r')k(r, r')dr' \tag{1.2}$$

where $k(r, r')$ is the kernel of the operator. In general, this problem does not have an analytical solution. Instead of solving (1.1), we solve the variational problem

$$\langle Lf, u\rangle = \langle b, u\rangle \tag{1.3}$$

where the function u is called the testing function and the inner product $\langle \cdot\,, \cdot \rangle$ is defined as

$$\langle v, u\rangle = \int_{\Gamma} v(r)u(r)dr \tag{1.4}$$

In order to solve equation (1.3) numerically, we divide the boundary into N elements, which can be line segments or triangles, depending on the dimension of the problem. Hence, the boundary is expressed as $\Gamma = \bigcup_{i=1}^{N} \Gamma_i$. In each Γ_i we define the local basis and testing functions ϕ_i and ψ_i respectively. Then, f and u are expanded as

$$f = \sum_{n=1}^{N} a_n \phi_n \tag{1.5}$$

$$u = \sum_{m=1}^{N} \psi_m \tag{1.6}$$

The basis and testing functions are chosen according to the properties of the operator. Replacing (1.5) and (1.6) in equation 1.3 we get the matrix equation

$$\mathbf{La} = \mathbf{b} \tag{1.7}$$

where the vector $\mathbf{a}$ contains the coefficients a_n of equation (1.5) and

$$\mathbf{L}_{nm} = \langle L(\phi_n), \psi_m\rangle \tag{1.8a}$$

$$\mathbf{b}_m = \langle b, \psi_m\rangle \tag{1.8b}$$

With this approach the problem is solved numerically by finding the coefficient **a** and therefore the function f.

1.2 Maxwell equations

In computational electromagnetic, the starting point is the Maxwell equations. These equations are the compendium of the previous work of many physicists, principally André-Marie Ampere, Michael Faraday and Carl Friedrich Gauss. In this section we present Maxwell equations and some derived forms that are used further on in this thesis.

Maxwell equations in differential form for homogeneous bodies read [41]

$$\nabla \times \mathcal{E} = -\mu \frac{\partial \mathcal{H}}{\partial t} \tag{1.9a}$$

$$\nabla \times \mathcal{H} = \epsilon \frac{\partial \mathcal{E}}{\partial t} + \mathcal{J} \tag{1.9b}$$

$$\nabla \cdot \mathcal{E} = \frac{\rho}{\epsilon} \tag{1.9c}$$

$$\nabla \cdot \mathcal{H} = 0 \tag{1.9d}$$

where $\mathcal{E}$ is the electric field, $\mathcal{H}$ is the magnetic field, $\mathcal{J}$ is the electric current density and ϵ and μ are the permittivity and permeability of the medium respectively. Applying the divergence operator to (1.9b) we get the charge conservation equation law

$$\nabla \cdot \mathcal{J} = -\frac{\partial \rho}{\partial t}. \tag{1.10}$$

Moreover, the electric current density $\mathcal{J}$ in presence of an electric field can be written as

$$\mathcal{J} = \sigma \mathcal{E} + \mathcal{J}_i \tag{1.11}$$

where σ is the conductivity of the medium and where $\mathcal{J}_i$ is the impressed current density. This equation is known as Ohm's law.

1.2.1 Static Case

In the static case, the first two Maxwell equations read

$$\nabla \times \mathcal{E} = 0 \tag{1.12a}$$

$$\nabla \times \mathcal{H} = \mathcal{J} \tag{1.12b}$$

which indicates that the electric and magnetic fields are decoupled. By taking the divergence of (1.12b) and using the Ohm's law we get

$$-\nabla \cdot (\sigma \mathcal{E}) = \nabla \cdot \mathcal{J}_i. \tag{1.13}$$

The Helmholtz decomposition [41] shows that a vector field with a rotational zero can be expressed as the gradient of a scalar potential. Therefore, the electrostatic field can be formulated in terms of the electric potential V as $\mathcal{E} = -\nabla V$. By replacing this in (1.13) we get the Poisson equation

$$\nabla \cdot (\sigma \nabla V) = \nabla \cdot \mathcal{J}_i \tag{1.14}$$

1.2.2 Frequency domain

By applying Fourier transform to Maxwell equations, they are expressed in the frequency domain as

$$\nabla \times \mathbf{E} = -j\omega\mu\mathbf{H} \tag{1.15a}$$

$$\nabla \times \mathbf{H} = j\omega\epsilon\mathbf{E} + \mathbf{J} \tag{1.15b}$$

$$\nabla \cdot \mathbf{E} = \frac{\rho}{\epsilon} \tag{1.15c}$$

$$\nabla \cdot \mathbf{H} = 0 \tag{1.15d}$$

where $j = \sqrt{-1}$ is the imaginary number and ω is the angular frequency. Moreover, the charge conservation law is expressed by

$$\nabla \cdot \mathbf{J} = -j\omega\rho. \tag{1.16}$$

By taking the curl of (1.15a) and (1.15b), we get the vector wave equations

$$\nabla \times \nabla \times \mathbf{E} - k^2 \mathbf{E} = -jk\eta \mathbf{J} \tag{1.17a}$$

$$\nabla \times \nabla \times \mathbf{H} - k^2 \mathbf{H} = \nabla \times \mathbf{J} \tag{1.17b}$$

where $k = \omega\sqrt{\mu\epsilon}$ is the wave number and $\eta = \sqrt{\mu/\epsilon}$ is the impedance of the medium. From the vector wave equations, integral equations to solve electromagnetic problems of bodies in free space can be derived.

1.3 Static formulations

In this section is presented the electroencephalography (EEG) forward problem, which can be solved using a static approximation thanks to the low frequency signals present in the brain. We review the general strategy to solve the problem with integral equations and three specific approaches as well.

1.3.1 Electroencephalography forward problem

The aim of the EEG forward problem is to find, on the scalp of the head, the potentials generated by a brain source representing a group of neurons. The solution of this problem is used in the EEG inverse problem. It has been shown that the forward problem has a considerable influence on the precision of the inverse problem [1, 28, 56].

Finite element methods (FEM) and boundary element methods (BEM) have been used to solve the EEG forward problem [34]. The FEM methods are based on partial derivative equations where a discretization of the entire domain is necessary. The advantage of these approaches is the capability to model complex structures and anisotropic scenarios. However, this is achieved at the cost of larger matrices. On the other hand, the BEM methods based on integral equations only require the discretization of the boundary. This reduces the system complexity at the cost of simplified models. Since in this thesis only integral

equations are used, we deal only with the BEM methods. First, we present the general strategy to solve the EEG forward problem with BEM formulations.

1.3.2 General formulation

Let $\Omega = \bigcup_{i=1}^{N} \Omega_i$ be a nested domain in R^3 with sufficiently smooth boundaries $\partial\Omega$. The exterior domain $\Omega_{N+1} = R^3 \backslash \overline{\Omega}$ extends to infinity as is shown in figure 1.1. We define the surface $\Gamma_i = \partial\Omega_i \cap \partial\Omega_{i+1}$, denote with $\mathbf{n}_i$ its outward going surface normal.

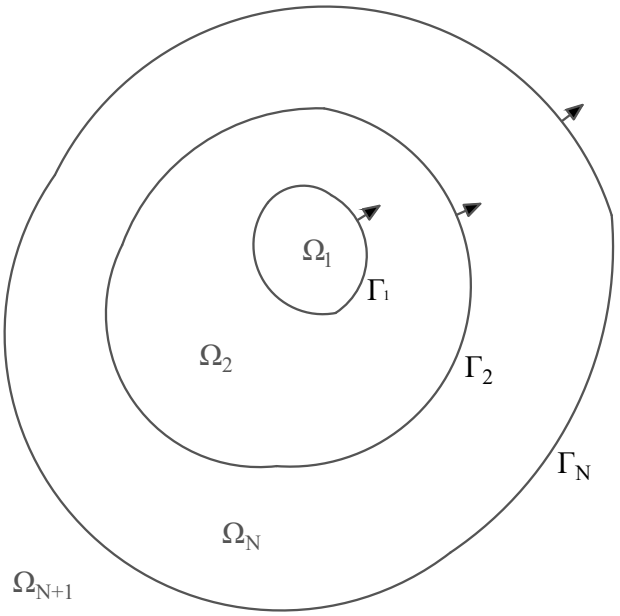

Figure 1.1: Nested domain.

In the EEG forward problem we seek to find the potentials on the scalp generated by a known source located in the brain. Due to the low frequency of the brain waves it is possible to use a quasi-static approximation yielding the Poisson equation

$$\nabla \cdot (\sigma \nabla V) = \nabla \cdot J = f \tag{1.18}$$

where V is the unknown potential, σ is the conductivity and J is the current source density. In the case of a nested domain, we assume piecewise isotropic and homogeneous conductivity. As a consequence, equation (1.18) can be rewritten in each subdomain Ω_i as

$$\sigma_i \Delta V = f \tag{1.19}$$

In the exterior domain Ω_{N+1} we have $\sigma_{N+1} = 0$. The jump of a function $g(r)$ at the surface Γ_i is defined by $[g]_i = g_i^- - g_i^+$ where the interior and exterior limits are

$$g_i^{\pm} = \lim_{\alpha \to 0^{\pm}} g(\mathbf{r} + \alpha \mathbf{n}), \quad \text{for } \mathbf{r} \in \Gamma_i.$$

With this approach we have the boundary conditions

$$[V]_i = 0, \quad \forall i \leq N \tag{1.20a}$$

$$[\sigma \partial_n V]_i = 0, \quad \forall i \leq N, \tag{1.20b}$$

where $\partial_n V = \mathbf{n} \cdot \nabla V$ is the normal derivative. These boundary conditions impose the continuity of the potential and density current at the interfaces between two regions.

In an unbounded medium, (1.19) can be solved using a homogeneous solution v. However, this solution does not take into account the boundary conditions. We then add a harmonic solution u in order to fulfill these conditions in the final solution V.

In order to build the homogeneous solution, the source is decomposed as

$$f = \sum_{i=1}^{N} f_i \tag{1.21}$$

where f_i is zero outside of Γ_i. We also define the static Green function as

$$G(\mathbf{r}, \mathbf{r}') = \frac{1}{4\pi ||\mathbf{r} - \mathbf{r}'||}, \tag{1.22}$$

where G is a fundamental solution of the Poisson equation $-\Delta G = \delta_0$, where δ is the Dirac delta distribution. Using (1.21) and (1.22) we build the homogeneous solution in each subdomain Ω_i as

$$v_i(\mathbf{r}) = -f_i * G(\mathbf{r}). \tag{1.23}$$

By using the properties of convolution and Green function we have that $\Delta v_i = -f_i * \Delta G = f_i$. Using a current dipole source $\mathbf{J}_{dip}(\mathbf{r}) = \mathbf{q}\delta_{\mathbf{r}_0}(\mathbf{r})$, where $\mathbf{q}$ is the dipolar moment, the homogeneous potential reads

$$v_i(\mathbf{r}) = \frac{\mathbf{q} \cdot (\mathbf{r} - \mathbf{r}_0)}{4\pi ||\mathbf{r} - \mathbf{r}_0||^3}, \tag{1.24}$$

where $\mathbf{r}_0$ is the position of the dipole source.

Now, let u be a harmonic solution, i.e.

$$\Delta u = 0\,, \quad \text{in } R^3 \backslash \partial\Omega$$

such that u is also a potential vanishing at infinity, satisfying the conditions

$$\begin{aligned} \lim_{r\to\infty} r|u(r)| &< \infty \\ \lim_{r\to\infty} r\frac{\partial u(r)}{\partial r} &= 0. \end{aligned} \tag{1.25}$$

For this harmonic potential u, the representation theorem reads [45]

$$-\partial_n u = \mathcal{N}[u] - \mathcal{D}^*[\partial_n u]\,, \qquad \mathbf{r} \notin \partial\Omega \tag{1.26a}$$

$$u = -\mathcal{D}[u] + \mathcal{S}[\partial_n u]\,, \qquad \mathbf{r} \notin \partial\Omega \tag{1.26b}$$

$$-(\partial_n u)^{\pm} = \mathcal{N}[u] + \left(\pm\frac{\mathcal{I}}{2} - \mathcal{D}^*\right)[\partial_n u]\,, \qquad \mathbf{r} \in \partial\Omega \tag{1.26c}$$

$$u^{\pm} = \left(\mp\frac{\mathcal{I}}{2} - \mathcal{D}\right)[u] + \mathcal{S}[\partial_n u]\,, \qquad \mathbf{r} \in \partial\Omega \tag{1.26d}$$

where $\mathcal{I}$ is the identity operator and where the operators $\mathcal{S}$, $\mathcal{D}$, $\mathcal{D}^*$ and $\mathcal{N}$ are defined as

$$\begin{aligned} (\mathcal{S}f)(\mathbf{r}) &= \int_{\partial\Omega} f(\mathbf{r}')\, G(\mathbf{r} - \mathbf{r}')\, \mathrm{d}s(\mathbf{r}') \\ (\mathcal{D}f)(\mathbf{r}) &= \int_{\partial\Omega} f(\mathbf{r}')\, \partial_{n'} G(\mathbf{r} - \mathbf{r}')\, \mathrm{d}s(\mathbf{r}') \\ (\mathcal{D}^*f)(\mathbf{r}) &= \int_{\partial\Omega} f(\mathbf{r}')\, \partial_{n} G(\mathbf{r} - \mathbf{r}')\, \mathrm{d}s(\mathbf{r}') \\ (\mathcal{N}f)(\mathbf{r}) &= \int_{\partial\Omega} f(\mathbf{r}')\, \partial_{n}\partial_{n'} G(\mathbf{r} - \mathbf{r}')\, \mathrm{d}s(\mathbf{r}') \end{aligned} \tag{1.27}$$

This representation theorem holds in case of nested domains as the one presented in figure 1.1. With the homogeneous and harmonic solution we can build the potential V.

There are different approaches to solve equation (1.19), depending on the choice of the global homogeneous solution, which is built using the local functions (1.23), and on the properties of the harmonic potential.

1.3.3 Single layer approach

For a nested domain Ω as the one shown in figure 1.1, the first boundary condition is set by construction as $[V]_j = 0$ and we then use a harmonic solution to fulfill the second boundary condition $[\sigma \partial_n V] = 0$. Hence, we construct the solution

$$V = v_s + u_s, \tag{1.28}$$

where v_s is a global homogeneous solution and u_s is a global harmonic solution.

We build v_s with the local homogeneous solutions v_i as

$$v_s = \sum_{i=1}^{N} \frac{v_i}{\sigma_i}. \tag{1.29}$$

This global solution has the boundary conditions $[v_s]_i = 0$, $[\partial_n v_s]_i = 0$ and it is a solution of the Poisson equation $\sigma \Delta v_s = f$.

In the case of the harmonic solution, let u be a local harmonic function with $[u] = 0$ and $p = [\partial_n u]$. Therefore, from the representation theorem, $u = \mathcal{S}p$ and $[\partial_n u] = [\partial_n \mathcal{S}p] = p$. Using this function we build the global harmonic solution as

$$u_s = \sum_{i=1}^{N} \mathcal{S}p_i \tag{1.30}$$

that holds the properties of the local function, $[u_s]_i = 0$ and $[\partial_n u_s]_i = p_i$. We then express the harmonic solution in (1.28) as $u_s = V - v_s$. Therefore, we have that $\sigma_i \Delta u_s = \sigma_i \Delta V - \sigma_i \Delta v_s = 0$. Now, taking the jump $[\sigma \partial_n u_s]_i = \sigma \partial_n u_s^- - \sigma \partial_n u_s^+$ and using the properties of u_s, together with (1.26a) and (1.26c), yields the function

$$[\sigma \partial_n u_s]_i = \frac{\sigma_i + \sigma_{i+1}}{2} p_i + (\sigma_i - \sigma_{i+1}) \sum_{j=1}^{N} \mathcal{D}_{ij}^* p_j. \tag{1.31}$$

Imposing the second boundary condition $[\sigma\partial_n V]_i = [\sigma\partial_n v_s]_i + [\sigma\partial_n u_s]_i = 0$ we can write

$$[\sigma\partial_n u_s]_i = -[\sigma\partial_n v_s]_i = -(\sigma_i - \sigma_{i+1})\partial_n v_s \tag{1.32}$$

Finally, combining (1.31) and (1.32) we have the equation

$$\partial_n v_s = \frac{\sigma_i + \sigma_{i+1}}{2(\sigma_{i+1} - \sigma_i)} p_i - \sum_{j=1}^{N} \mathcal{D}^*_{ij} p_j, \quad \mathbf{r} \in \Gamma_i, \tag{1.33}$$

where the notation $\mathcal{L}_{ij}$ indicates an operator acting on function defined on Γ_j and that yields on function defined on Γ_i. We create a linear system taking all the interfaces, yielding in N linear equations where the unknown function is p. The harmonic solution is found using (1.30) in order to compute the total solution (1.28).

1.3.4 Double layer approach

Let Ω be a nested domain as the one shown in figure 1.1. In this case we set by construction the second boundary condition $[\sigma\partial_n V] = 0$. We then use a harmonic function to accomplish the first boundary condition. Hence, we have

$$\sigma V = v_d + u_d, \tag{1.34}$$

where v_d is the global homogeneous solution and u_d is the global harmonic solution. We build the homogeneous solution using the local solutions as

$$v_d = \sum_{i=1}^{N} v_i \tag{1.35}$$

with boundary conditions $[v_d]_i = 0$, $[\partial_n v_d]_j = 0$ and it is solution of the Poisson equation $\Delta v_d = f$.

In order to build the global harmonic solution u_d, first we choose a local harmonic solution u with a normal derivative that does not jump in the boundary, i.e. $[\partial_n u] = 0$. We define $q = -[u]$. We can then write, using the representation theorem, $u = \mathcal{D}q$ and

$[u] = [\mathcal{D}q] = -q$. The global function is constructed by adding the contributions of all the interfaces

$$u_d = \sum_{i=1}^{N} \mathcal{D}q_i, \tag{1.36}$$

where the boundary conditions of the local function are kept. We next set the boundary condition $[V]_i = 0$, that yields in the equation

$$(\sigma_{i+1} - \sigma_i)v_d = \sigma_{i+1}u_d^+ - \sigma_i u_d^- = \frac{\sigma_i + \sigma_{i+1}}{2}q - \sum_{j=1}^{N}(\sigma_{j+1} - \sigma_j)\mathcal{D}_{ij}q. \tag{1.37}$$

We can express $q = -[u_d]_i = -[\sigma V]_i = (\sigma_{i+1} - \sigma_i)V_i$. Hence, the final equation reads

$$v_d = \frac{\sigma_i + \sigma_{i+1}}{2}V_i - \sum_{j=1}^{N}(\sigma_{j+1} - \sigma_j)\mathcal{D}_{ij}V_j, \quad \mathbf{r} \in \Gamma_i \tag{1.38}$$

The advantage of this approach is that the linear system is solved for V directly. Therefore, no extra steps are needed.

1.3.5 Symmetric formulation

Let Ω be a nested domain as the one shown in figure 1.1. We define in each subdomain Ω_i a harmonic function as

$$u_{\Omega_i} = \begin{cases} V - \frac{v_i}{\sigma_i}, & \text{in } \Omega_i \\ -\frac{v_i}{\sigma_i} & \text{in } R^3 \backslash \overline{\Omega}_i \end{cases} \tag{1.39}$$

where v_i is defined in (1.23). Recalling that the boundary of our domain is $\partial\Omega_i = \Gamma_{i-1} \cup \Gamma_i$, the boundary conditions for u_{Ω_i} and $\partial_n u_{\Omega_i}$ read

$$[u_{\Omega_i}]_i = V_i\,, \qquad [u_{\Omega_i}]_{i-1} = -V_{i-1} \tag{1.40a}$$

$$[\partial_n u_{\Omega_i}]_i = (\partial_n V)_i^-\,, \qquad [\partial_n u_{\Omega_i}]_{i-1} = -(\partial_n V)_{i-1}^+ \tag{1.40b}$$

By setting the boundary (1.20b) in Γ_i, we have $[\sigma\partial_n V]_i = \sigma_i(\partial_n V)_i^- - \sigma_{i+1}(\partial_n V)_i^+ = 0$. Hence, we can define $x_i = \sigma_i(\partial_n V)_i^- = \sigma_{i+1}(\partial_n V)_i^+$. With the representation theorem, we then express the internal limit $(u_{\Omega_i})_i^- = \left(V - \sigma_i^{-1}v_i\right)_i^-$ in Γ_i as

$$\left(V-\sigma_i^{-1}v_i\right)_i^- = \frac{[u_{\Omega_i}]_i}{2} - \mathcal{D}_{i,i}[u_{\Omega_i}]_i - \mathcal{D}_{i,i-1}[u_{\Omega_i}]_{i-1} + \mathcal{S}_{i,i}[\partial_n u_{\Omega_i}]_i + \mathcal{S}_{i,i-i}[\partial_n u_{\Omega_i}]_{i-1}$$
$$= \frac{V_i}{2} - \mathcal{D}_{i,i}V_i + \mathcal{D}_{i,i-1}V_{i-1} + \sigma_i^{-1}\mathcal{S}_{i,i}x_i - \sigma_i^{-1}\mathcal{S}_{i,i-i}x_{i-1}$$

and the external limit $(u_{\Omega_{i+1}})_i^+ = \left(V-\sigma_{i+1}^{-1}v_{i+1}\right)_i^+$ in Γ_i as

$$\left(V-\sigma_{i+1}^{-1}v_{i+1}\right)_i^+ = -\frac{[u_{\Omega_{i+1}}]_i}{2} - \mathcal{D}_{i,i}[u_{\Omega_{i+1}}]_i - \mathcal{D}_{i,i+1}[u_{\Omega_{i+1}}]_{i+1} + \mathcal{S}_{i,i}[\partial_n u_{\Omega_{i+1}}]_i + \mathcal{S}_{i,i+i}[\partial_n u_{\Omega_{i+1}}]_{i+1}$$
$$= \frac{V_i}{2} + \mathcal{D}_{i,i}V_i - \mathcal{D}_{i,i+1}V_{i+1} - \sigma_{i+1}^{-1}\mathcal{S}_{i,i}x_i + \sigma_{i+1}^{-1}\mathcal{S}_{i,i+1}x_{i+1}$$

Subtracting both limits yields the equation

$$\sigma_{i+1}^{-1}(v_{i+1})_i - \sigma_i^{-1}(v_i)_i = \mathcal{D}_{i,i-1}V_{i-1} - 2\mathcal{D}_{i,i}V_i + \mathcal{D}_{i,i+1}V_{i+1}$$
$$- \sigma_i^{-1}\mathcal{S}_{i,i-1}x_{i-1} + (\sigma_i^{-1}+\sigma_{i+1}^{-1})\mathcal{S}_{i,i}x_i - \sigma_{i+1}^{-1}\mathcal{S}_{i,i+1}x_{i+1} \quad (1.41)$$

In the same manner, by using (1.26c), the internal limit $(\sigma_i\partial_n u_{\Omega_i})_i^- = (x-\partial_n v_i)_i^-$ in Γ_i can be expressed as

$$(x-\partial_n v_i)_i^- = \sigma_i\left(-\mathcal{N}_{i,i}[u_{\Omega_i}]_i - \mathcal{N}_{i,i-1}[u_{\Omega_i}]_{i-1} + \frac{[\partial_n u_{\Omega_i}]_i}{2} + \mathcal{D}^*_{i,i}[\partial_n u_{\Omega_i}]_i + \mathcal{D}^*_{i,i-1}[\partial_n u_{\Omega_i}]_{i-1}\right)$$
$$= -\sigma_i\mathcal{N}_{i,i}V_i + \sigma_i\mathcal{N}_{i,i-1}V_{i-1} + \frac{x_i}{2} + \mathcal{D}^*_{i,i}x_i - \mathcal{D}^*_{i,i-1}x_{i-1}$$

and the external limit $(\sigma_{i+1}\partial_n u_{\Omega_{i+1}})_i^+ = (x-\partial_n v_{i+1})_i^+$ in Γ_i as

$$(x-\partial_n v_{i+1})_i^+ = \sigma_{i+1}\left(-\mathcal{N}_{i,i}[u_{\Omega_{i+1}}]_i - \mathcal{N}_{i,i+1}[u_{\Omega_{i+1}}]_{i+1} - \frac{[\partial_n u_{\Omega_{i+1}}]_i}{2} + \mathcal{D}^*_{i,i}[\partial_n u_{\Omega_{i+1}}]_i + \mathcal{D}^*_{i,i+1}[\partial_n u_{\Omega_{i+1}}]_{i+1}\right)$$
$$= \sigma_{i+1}\mathcal{N}_{i,i}V_i - \sigma_{i+1}\mathcal{N}_{i,i+1}V_{i+1} + \frac{x_i}{2} - \mathcal{D}^*_{i,i}x_i + \mathcal{D}^*_{i,i+1}x_{i+1}$$

As before, we subtract both limits to get the equation

$$(\partial_n v_i)_i - (\partial_n v_{i+1})_i = \mathcal{D}^*_{i,i-1}x_{i-1} - 2\mathcal{D}^*_{i,i}x_i + \mathcal{D}^*_{i,i+1}x_{i+1}$$
$$- \sigma_i\mathcal{N}_{i,i-1}V_{i-1} + (\sigma_i+\sigma_{i+1})\mathcal{N}_{i,i-1}V_{i-1} - \sigma_{i+1}\mathcal{N}_{i,i+1}V_{i+1} \quad (1.42)$$

Finally, we use (1.41) and (1.42) to build a system of linear equations. We set to zero x_N since $\sigma_{N+1} = 0$ and all the terms defined in the nonexistent interfaces Γ_0 and Γ_{N+1} as well. Therefore, the system to solve reads

$$\mathcal{Z}y = b, \quad (1.43)$$

where $\mathcal{Z}$, y and b are defined as

$$\mathcal{Z} = \begin{bmatrix} \alpha_1 N_{11} & -2D^*_{11} & -\sigma_2 N_{12} & D^*_{12} & & & & \\ -2D_{11} & \beta_1 S_{11} & D_{12} & -\sigma_2^{-1} S_{12} & & & & \\ -\sigma_2 N_{21} & D^*_{21} & \alpha_2 N_{22} & -2D^*_{22} & \cdots & & & \\ D_{21} & -\sigma_2^{-1} S_{21} & -2D_{22} & \beta_2 S_{22} & \cdots & & & \\ & & \vdots & \vdots & \ddots & & & \\ & & & & & \alpha_{N-1}\mathbf{N}_{N-1,N-1} & 2\mathbf{D}^*{}_{N-1,N-1} & -\sigma_N \mathbf{N}_{N-1,N} \\ & & & & & -2D_{N-1,N-1} & \beta_{N-1} S_{N-1,N-1} & D_{N-1,N} \\ & & & & & -\sigma_N N_{N,N-1} & D_{N,N-1} & \sigma_N N_{N,N} \end{bmatrix}$$

$$y = \begin{bmatrix} V_1 \\ x_1 \\ V_2 \\ x_2 \\ \vdots \\ x_{N-1} \\ V_N \end{bmatrix}, \quad b = \begin{bmatrix} (\partial_n v_1)_{\Gamma_1} - (\partial_n v_2)_{\Gamma_1} \\ \sigma_2^{-1} (v_2)_{\Gamma_1} - \sigma_1^{-1} (v_1)_{\Gamma_1} \\ (\partial_n v_2)_{\Gamma_2} - (\partial_n v_3)_{\Gamma_2} \\ \sigma_3^{-1} (v_3)_{\Gamma_2} - \sigma_2^{-1} (v_2)_{\Gamma_2} \\ \vdots \\ \sigma_N^{-1} (v_N)_{\Gamma_N - 1} - \sigma_{N-1}^{-1} (v_{N-1})_{\Gamma_N - 1} \\ (\partial_n v_N)_{\Gamma_N} \end{bmatrix}, \quad \begin{matrix} \alpha_i = \sigma_i + \sigma_{i+1} \\ \beta_i = \sigma_i^{-1} + \sigma_{i+1}^{-1} \end{matrix}$$

Contrary to the single and double layer formulations, the symmetric formulation has a first kind operator. This gives rise to an ill-conditioning of the matrix operator when the mesh refinement is increased. Moreover, the operator also presents an ill-conditioning due to high contrast conductivity. In Chapter 2 a preconditioner for the $\mathcal{Z}$ operator is presented that solved both ill-conditioning problems.

For more information about the single, double and symmetric formulations of the EEG forward problem, the reader is referred to [44, 34].

1.4 High frequency formulation

In high frequency electromagnetic problems, formulations for penetrable objects have been widely studied due to their applicability in several scenarios. In BEM methods, one of the most used formulations is the Poggio-Miller-Chang-Harrington-Wu-Tsai (PMCHWT) integral equation [41], which presents a high accuracy and stability [50]. This equation has

been used in dosimetry problems [52], where the dose of ionizing radiation absorbed for the human body is measured. A review of this equation is presented in this section.

1.4.1 The PMCHWT formulation

First, we introduce the Green equation

$$G^k(\mathbf{r},\mathbf{r}') = \frac{e^{-jk|\mathbf{r}-\mathbf{r}'|}}{4\pi|\mathbf{r}-\mathbf{r}'|} \tag{1.44}$$

that is the solution of the Helmholtz equation

$$\nabla^2 G^k(\mathbf{r},\mathbf{r}') + k^2 G^k(\mathbf{r},\mathbf{r}') = -\delta(\mathbf{r}-\mathbf{r}') \tag{1.45}$$

and which satisfies the radiation condition

$$r\left[\frac{\partial G^k(\mathbf{r},\mathbf{r}')}{\partial r} + jkG^k(\mathbf{r},\mathbf{r}')\right] = 0, \quad r \to \infty \tag{1.46}$$

We also need the following Green's theorem

$$\int_V [b(\nabla\times\nabla\times\mathbf{A}) + \mathbf{A}\nabla^2 b + (\nabla\cdot\mathbf{A})\nabla b]dV = \int_S [(\mathbf{n}\cdot\mathbf{A})\nabla b + (\mathbf{n}\times\mathbf{A})\times\nabla b + (\mathbf{n}\times\nabla\times\mathbf{A})b]dS \tag{1.47}$$

where $\mathbf{A}$ is a vector function, b is a scalar function and $\mathbf{n}$ is the outward going normal to the surface S.

Now, we consider a dielectric object Ω_i with a sufficiently smooth boundary Γ and impedance η_i. The exterior domain $\Omega_o = R^3\backslash\Omega_i$ has an intrinsic impedance η_o. An electromagnetic wave $(\mathbf{E}^{inc}, \mathbf{H}^{inc})$ is impinging in Ω_i. Since the body is dielectric, we can analyze the problem in Ω_i and Ω_o.

By taking $b = G^k$ and $\mathbf{A} = \mathbf{E}$ for the exterior and interior domain in (1.47) together with the wave equation for the electric field (1.17a), and after some manipulation, we get the surface integral equations

$$-\eta_o \mathcal{T}^{k_o}\mathbf{J}_s + \frac{1}{2}\mathbf{M}_s + \mathcal{K}^{k_o}\mathbf{M}_s = -\mathbf{n}\times\mathbf{E}_{inc} \tag{1.48a}$$

$$\eta_i \mathcal{T}^{k_i}\mathbf{J}_s + \frac{1}{2}\mathbf{M}_s - \mathcal{K}^{k_i}\mathbf{M}_s = 0 \tag{1.48b}$$

with k_o the wave number in the free space, $k_i = k_o\sqrt{\mu_r \epsilon_r}$ the wave number inside the object, $\mathbf{J}_s(\mathbf{r}') = \mathbf{n} \times \mathbf{H}(\mathbf{r}')$ the electric surface current density, $\mathbf{M}_s = \mathbf{n} \times E$ the magnetic surface current density and where the electric field integral operator (EFIO) reads

$$(\mathcal{T}^k f)(r) = jk\,\mathbf{n} \times \int_\Gamma G^k(\mathbf{r}, \mathbf{r}') f(\mathbf{r}') dS(\mathbf{r}') - \frac{1}{jk}\mathbf{n} \times \nabla \int_\Gamma G^k(\mathbf{r}, \mathbf{r}') \nabla' \cdot f(\mathbf{r}') dS(\mathbf{r}') \quad (1.49)$$

and where the magnetic field integral operator (MFIO) reads

$$(\mathcal{K}^k f)(\mathbf{r}) = \mathbf{n} \times \int_\Gamma \nabla G^k(\mathbf{r}, \mathbf{r}') \times f(\mathbf{r}') dS(\mathbf{r}'). \quad (1.50)$$

In the same way, if we take $\mathbf{A} = \mathbf{H}$, we get the equations

$$\frac{1}{2}\mathbf{J}_s + \mathcal{K}^{k_o}\mathbf{J}_s + \frac{1}{\eta_o}\mathcal{T}^{k_o}\mathbf{M}_s = \mathbf{n} \times \mathbf{H}_{inc} \quad (1.51a)$$

$$\frac{1}{2}\mathbf{J}_s - \mathcal{K}^{k_i}\mathbf{J}_s - \frac{1}{\eta_i}\mathcal{T}^{k_i}\mathbf{M}_s = 0 \quad (1.51b)$$

Finally, subtracting equations (1.48a), (1.48b) and equations (1.51a), (1.51b), we get the system

$$\begin{aligned} (\eta_o \mathcal{T}^{k_o} + \eta_i \mathcal{T}^{k_i})\,\mathbf{J}_s - (\mathcal{K}^{k_o} + \mathcal{K}^{k_i})\,\mathbf{M}_s &= \mathbf{n} \times \mathbf{E}^{inc} \\ (\mathcal{K}^{k_o} + \mathcal{K}^{k_i})\,\mathbf{J}_s + \left(\frac{1}{\eta_o}\mathcal{T}^{k_o} + \frac{1}{\eta_i}\mathcal{T}^{k_i}\right)\mathbf{M}_s &= \mathbf{n} \times \mathbf{H}^{inc} \end{aligned} \quad (1.52)$$

This system is known as PMCHWT integral equation, which is used to solve scattering problem of dielectric bodies. We can rewrite the system in operator equation form as

$$\mathcal{Z}\mathbf{a} = \mathbf{b} \quad (1.53)$$

with

$$\mathcal{Z} = \begin{bmatrix} (\eta_o \mathcal{T}^{k_o} + \eta_i \mathcal{T}^{k_i}) & -(\mathcal{K}^{k_o} + \mathcal{K}^{k_i}) \\ (\mathcal{K}^{k_o} + \mathcal{K}^{k_i}) & \left(\frac{1}{\eta_o}\mathcal{T}^{k_o} + \frac{1}{\eta_i}\mathcal{T}^{k_i}\right) \end{bmatrix}$$

$$\mathbf{a} = \begin{bmatrix} \mathbf{J}_s \\ \mathbf{M}_s \end{bmatrix}, \quad \mathbf{b} = \begin{bmatrix} \mathbf{n} \times \mathbf{E}^{inc} \\ \mathbf{n} \times \mathbf{H}^{inc} \end{bmatrix} \quad (1.54)$$

In general, the block operator $\mathcal{Z}$ has the same drawbacks as the EFIO and MFIO, which are the ill-conditioning for low frequency and the ill-conditioning when the mesh is refined. A solution for these issues is treated in Chapter 4.

Chapter 2

A Calderon preconditioner for the symmetric formulation for the EEG forward problem

The symmetric formulation of the electroencephalography (EEG) forward problem is a well-known and widespread equation thanks to the high level of accuracy that it delivers. However, this equation is first kind in nature and gives rise to ill-conditioned problems when the discretization density or the brain conductivity contrast increases, resulting in numerical instabilities and increasingly slow solutions. This work addresses and solves this problem by proposing a new regularized symmetric formulation. The new scheme is obtained by leveraging on Calderon identities which allow to introduce a dual symmetric equation that, combined with the standard one, results in a second kind operator which is both stable and well-conditioned under all the above mentioned conditions. The new formulation presented here can be easily integrated into existing EEG imaging packages since it can be obtained with the same computational technology required by the standard symmetric formulation. The performance of the new scheme are substantiated by both theoretical developments and numerical results which corroborate the theory and show the practical impact of the new technique.

2.1 Introduction

Functional brain imaging based on high-resolution scalp Electroencephalographies (EEGs) is characterized by very high levels of temporal resolution and, as such, it provides an unmatched overview on the underlying brain activity [29, 51, 66, 58]. This technique relies on the key task, referred to as the EEG inverse problem, of recovering the brain electric current sources responsible for a measured potential at the EEG scalp electrodes [61, 67]. The EEG inverse problem requires multiple solutions of the EEG forward problem, i.e. the computation of the scalp potential starting from the source currents [32, 36]. It has been widely studied and reported that the accuracy of EEG forward problem solvers has a direct impact on EEG inverse solution procedures [28, 56, 1, 15]. For this reason, any advancement of the state of the art in EEG forward solution technologies will have a direct impact on the overall high-resolution EEG imaging process.

When realistic head models are used [80, 19, 72, 1, 63, 10], the solution of the EEG forward problem can only be obtained numerically. Classical strategies to obtain this numerical solution are the Finite Element Method (FEM), the Finite Difference Method (FDM) or the Boundary Element Method (BEM) [34]. Both FDM and FEM leverage on a volume discretization of the considered head model. This implies them to take into account the different head conductivities' inhomogeneities or the anisotropies at the cost, however, of a higher computational demand. Previous works have shown that by using transfer matrices the computation time of the FEM formulations can be reduced [23, 30]. The use of these transfer matrices in FEM formulations yield similar computational times as BEM formulations for comparable accuracies. [75].

When the conductivity of the head is modelled as piecewise homogeneous, BEM can be easily used to compute the solution of the EEG forward problem. In order words, the main limitation of the BEM formulation resides in its inability to model anisotropies. However,

this method has the advantage that it requires only the discretization of the interface between regions with different conductivities [34]. Several studies (for example, [15, 38, 62]) focused on the impact of the head model simplifications in recovering the electric brain sources from the measurement of scalp potential. In particular, when computing the EEG forward problem, [74, 78, 49] have shown the importance of modelling correctly the skull anisotropy. However, when the anisotropic conductivity values are not known, it can be preferable to model this region as isotropic, as explained in [74]. Moreover, the anisotropic conductivity of the skull is due to its layered structure, a cancellous bone comprised between two compact bones. This means that when those three layers are available, the skull can accurately be modelled with three isotropic layers instead of one anisotropic layer as [21] shows.

The relevant computational savings which the use of BEM strategies can lead to, explain the attention the technique has received by the community, resulting in a continuous series of advances [34, 35, 27, 26, 3, 16]. Among them a method, the method published in [45], and referred to as the "symmetric formulation", became quite popular and impacted several EEG based imaging tools [55, 31, 71, 20]. The peculiarity of the BEM method proposed in [45] is the quite higher level of accuracy that it can achieve when compared to previously existing schemes. However these beneficial properties are obtained at the cost of using a first kind formulation (while the majority of standard strategies relies on second kind formulations). The computational consequence of this fact is that, when the "symmetric formulation" is discretized to be solved numerically, the condition number of the resulting BEM matrix (the ratio of the largest over the smallest singular value of the matrix) will grow as a function of the discretization density (the number of boundary elements used to discretize the structure) [69]. Similarly, a condition number growth is observed in the symmetric formulation also when the conductivity contrast between two regions of the head is increased (a case of practical interest given that the conductivity of the skull

is often modeled with a much smaller value with respect to the conductivity of the brain [1, 47, 81, 48]). In several cases, especially when handling models issued of high resolution Magnetic Resonance Imaging (MRI) [43], the solution of the EEG forward problem is obtained iteratively [34, 46]. A low and stable condition number is desirable since, on the one hand, the number of iterations of an iterative solver is growing with the condition numbers [9] and, on the other hand, the condition number controls the amplification in the solution of any initial error in the sources [9]. In other words, the higher the condition number, the longer the time needed to compute the solution, and the less correct the solution will be.

The purpose of this work is to address the ill-conditioning problems of the symmetric formulation. Given the favor that the formulation has found in the community and the fact that it is already implemented in several neuroimaging packages, a particular attention will be devoted to develop a solution strategy that will be conservative, in the sense that will not require the change of previous implementations of the symmetric formulation but will just require the addition of some extra steps to it. This will be achieved by developing a purely multiplicative preconditioner based on Calderon formulas, i.e. we will design a preconditioning matrix that is spectrally equivalent to the inverse of the symmetric formulation. After left multiplication of this matrix with the symmetric formulation matrix, the resulting linear system will, on the one hand, keep the accuracy the symmetric formulation is well known for and, on the other hand, will provide a stable condition number both when the mesh is refined and when the conductivity contrast between two adjacent domains increases. Partial results from this contribution has been presented in the conference contribution [57].

This chapter is organized as follows: Section 2.2 provides the reader with some necessary background material and notation used in the following developments. Section 2.3 presents the new Calderon preconditioner proposed in this work, while Section 2.4 focuses on its discretization and on the solution of the preconditioned symmetric formulation sys-

tem. Section 2.5 complements the paper's theoretical developments with numerical results which will show the efficiency and effectiveness of the new approach.

2.2 Background on the EEG Forward Problem

This section will briefly review the relevant formulations, currently available in literature, used to solve the EEG forward problem. The treatment will be synthetic and for the sole purpose of setting up the notation. The reader interested in a more profuse treatment should refer, for example to [45, 53] and to references therein.

2.2.1 The EEG Problem

Let $\Omega = \bigcup_{i=1}^{N_\Omega} \Omega_i$ be a nested domain with Lipchitz boundaries $\partial\Omega_i = \left(\bar{\Omega}_{i-1} \bigcap \bar{\Omega}_i\right) \bigcup \left(\bar{\Omega}_i \bigcap \bar{\Omega}_{i+1}\right)$ as in Fig. 2.1. We denote with $\boldsymbol{n}_i$ the outward going normal to the surface Γ_i, where $\Gamma_i = \bar{\Omega}_i \bigcap \bar{\Omega}_{i+1}$.

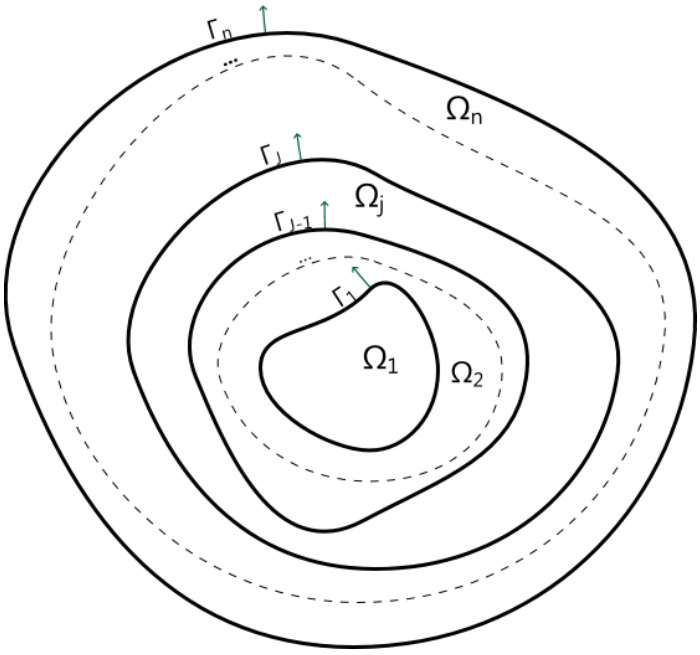

Figure 2.1: Geometry under consideration.

Solving the EEG forward problem amounts to compute the potential V at given electrodes' positions when the active brain current sources are known. Under quasi-static as-

sumptions and isotropic conductivity, the EEG forward problem reads [64]:

$$\sigma \Delta V = \nabla \cdot \boldsymbol{j} \tag{2.1}$$

where σ is the conductivity and $\boldsymbol{j}$ the current sources. The conductivity is assumed to be piecewise isotropic and homogeneous: in Ω_i, $\sigma = \sigma_i$. In the exterior domain, the conductivity is assumed to be 0. The current sources, as it is customary in literature [54], are assumed to be dipolar in nature. Hence, denoting with $f_i = \nabla \cdot \boldsymbol{j}$ the electric source in Ω_i, we have $f_i = q_i \cdot \nabla \delta_{r_i}$ with q_i the electric dipole moment and $\boldsymbol{r}_i$ its position. Furthermore, the symbol $[g]_i = g^- - g^+$, will refer to the jump of the function g at the interface Γ_i, with $g^{\mp}$ the inner and outer trace of g at Γ_i respectively. Then, the solvability of (2.1) is assured under the following boundary conditions [64]:

$$[V]_i = 0 \ \forall i \leq N \tag{2.2a}$$

$$[\sigma \boldsymbol{n} \cdot \nabla V]_i = 0 \ \forall i \leq N \tag{2.2b}$$

that enforce the continuity of the potential and the current between the different layers of the domain Ω.

The Green's function associated to (2.1) reads [69]

$$G(\boldsymbol{r}, \boldsymbol{r}') = \frac{1}{4\pi |\boldsymbol{r} - \boldsymbol{r}'|} \tag{2.3}$$

for which we can derive Green's representation theorem using the integral operators [69]

$$(D\Phi)(r) = \int_{\partial_\Omega} \partial_{n'} G(r, r') \Phi(r') dr' \ , \ D : H^{1/2} \to H^{1/2} \tag{2.4a}$$

$$(S\Psi)(r) = \int_{\partial_\Omega} G(r, r') \Psi(r') dr' \ , \ S : H^{-1/2} \to H^{1/2} \tag{2.4b}$$

$$(N\Phi)(r) = \int_{\partial_\Omega} \partial_n \partial_{n'} G(r, r') \Phi(r') dr' \ , \ N : H^{1/2} \to H^{-1/2} \tag{2.4c}$$

$$(D^*\Psi)(r) = \int_{\partial_\Omega} \partial_n G(r, r') \Phi(r') dr' \ , \ D^* : H^{-1/2} \to H^{-1/2}. \tag{2.4d}$$

In the above equation, H^s corresponds to the Sobolev space of order s. In the following, we will denote with L_{ij} the operator L when $r \in \Gamma_i$ and $r' \in \Gamma_j$ with $L = D, S, N$ or D^*. Note in particular that $L_{ij} : H^s(\Gamma_j) \rightarrow H^{s'}(\Gamma_i)$.

2.2.2 The Symmetric Formulation for the EEG Forward Problem

Several BEM formulations have been proposed to solve the EEG forward problem [34, 45]. Among them, the symmetric formulation [45] is quite popular and known for providing high levels of accuracy [31].

In solving the EEG forward problem, an efficient strategy is to build the unknown potential V starting from two functions, a function u harmonic in R^3 and a function v that takes into account the source term. The starting point of the symmetric formulation is to build u_i in each domain such that $u_i = V - v_i/\sigma_i$ in Ω_i and $u = -v_i/\sigma_i$ in $R^3 \setminus \Omega_i$, with v_i the solution of (2.1) in an unbounded medium: $v_i(r) = \int_{\Omega_i} f(r')G(r, r')dr'$. In this fashion, u_i is harmonic in $R^3 \setminus \partial\bar{\Omega}_i = \Gamma_{i-1} \cup \Gamma_i$. Using the boundary conditions (2.2a) and (2.2b) as well as the representation theorem [69], two integral equations for the potential and its derivative can be obtained [45]. They read:

$$\begin{aligned}\sigma_{i+1}^{-1}\left(v_{i+1}\right)_{\Gamma_i} - \sigma_i^{-1}\left(v_i\right)_{\Gamma_i} = {} & D_{i,i-1}V_{i-1} - 2D_{ii}V_i + D_{i,i+1}V_{i+1} \\ & - \sigma_i^{-1}S_{i,i-1}p_{i-1} + \left(\sigma_i^{-1} + \sigma_{i+1}^{-1}\right)S_{ii}p_i - \sigma_{i+1}^{-1}S_{i,i+1}p_{i+1} \quad (2.5)\end{aligned}$$

$$\begin{aligned}\left(\partial_n v_{i+1}\right)_{\Gamma_i} - \left(\partial_n v_i\right)_{\Gamma_i} = {} & \sigma_i N_{i,i-1}V_{i-1} - \left(\sigma_i + \sigma_{i+1}\right)N_{ii}V_i + \sigma_{i+1}N_{i,i+1}V_{i+1} \\ & - D^*_{i,i-1}p_{i-1} + 2D^*_{ii}p_i - D^*_{i,i+1}p_{i+1} \quad (2.6)\end{aligned}$$

with V_i the potential on the surface Γ_i and $p_i = \sigma_i\left[\boldsymbol{n} \cdot \nabla V\right]_i$. Equations (2.5) and (2.6) are obtained by applying the boundary conditions on the surface Γ_i. In a nested domain, it only involves the computation of the operators with functions defined in the surrounding

surfaces Γ_{i-1}, Γ_i and Γ_{i+1}. To clarify the ideas, equations (2.5) and (2.6) have been rewritten in matrix form in equation (2.7).

$$\begin{bmatrix} \alpha_1 N_{11} & -2D^*_{11} & -\sigma_2 N_{12} & D^*_{12} & & & & \\ -2D_{11} & \beta_1 S_{11} & D_{12} & -\sigma_2^{-1} S_{12} & & & & \\ -\sigma_2 N_{21} & D^*_{21} & \alpha_2 N_{22} & -2D^*_{22} & \cdots & & & \\ D_{21} & -\sigma_2^{-1} S_{21} & -2D_{22} & \beta_2 S_{22} & \cdots & & & \\ & & \vdots & \vdots & \ddots & & & \\ & & & & & \alpha_{N-1} N_{N-1,N-1} & 2D^*_{N-1,N-1} & -\sigma_N N_{N-1,N} \\ & & & & & -2D_{N-1,N-1} & \beta_{N-1} S_{N-1,N-1} & D_{N-1,N} \\ & & & & & -\sigma_N N_{N,N-1} & D_{N,N-1} & \sigma_N N_{N,N} \end{bmatrix}$$

$$\begin{bmatrix} V_1 \\ p_1 \\ V_2 \\ p_2 \\ \vdots \\ p_{N-1} \\ V_N \end{bmatrix} = \begin{bmatrix} (\partial_n v_1)_{\Gamma_1} - (\partial_n v_2)_{\Gamma_1} \\ \sigma_2^{-1} (v_2)_{\Gamma_1} - \sigma_1^{-1} (v_1)_{\Gamma_1} \\ (\partial_n v_2)_{\Gamma_2} - (\partial_n v_3)_{\Gamma_2} \\ \sigma_3^{-1} (v_3)_{\Gamma_2} - \sigma_2^{-1} (v_2)_{\Gamma_2} \\ \vdots \\ \sigma_N^{-1} (v_N)_{\Gamma_{N-1}} - \sigma_{N-1}^{-1} (v_{N-1})_{\Gamma_{N-1}} \\ (\partial_n v_N)_{\Gamma_N} \end{bmatrix} \tag{2.7}$$

with

$$\alpha_i = \sigma_i + \sigma_{i+1}, \quad \beta_i = \sigma_i^{-1} + \sigma_{i+1}^{-1}$$

For a more detailed explanation on the symmetric formulation, the reader is referred to Chapter 1.

2.2.3 Discretization of the Operators

The numerical solution of an integral equation is often obtained by using a Boundary Element Method (BEM). Following a well-established strategy, the domain Ω is tessellated into N_t triangular cells t_k of area A_k and average length h. The set of vertices of the tessellation will be denoted by $\{v_k\}_{k=1}^{N_v}$. Cells and vertices will form a mesh denoted by M_Ω. The number of triangles (respectively, vertices) of the surface Γ_i will be denoted N_{t_i} (respectively, N_{v_i}). To discretize the unknown and to test the equations the following standard basis functions will be used. The piecewise constant functions in P_0 are defined such that, $P_{0k} = 1/A_k$ in t_k and 0 elsewhere. The piecewise linear functions are the set

$P_1 = span\{P_{1k}\}_{k=1}^{N_v}$. The support of P_{1k}, denoted by $\mu_{P_{1k}}$, is the set of triangles around v_k such that $P_{1k} = 1$ in v_k and 0 on all other vertices. P_0 and P_1 functions are shown Fig. 2.3a and 2.3b respectively.

Following [2], on the surface Γ_i we discretize the two unknowns V_i and p_i with P_1 and P_0 basis functions respectively such that $V_i = \sum_l^{N_v} a_k P_{1l}$ and $p_i = \sum_l^{N_t} b_l P_{0l}$. To obtain the system matrix, the integral equations (2.5) and (2.6) are tested with P_0 and P_1 basis functions respectively. The operator matrices arising are then given by

$$[\mathbf{D}_{ij}]_{kl} = \int_{t_k} D_{ij}(P_{1l})\, P_{0k}(r) dr \tag{2.8a}$$

$$[\mathbf{S}_{ij}]_{kl} = \int_{t_k} S_{ij}(P_{0l})\, P_{0k}(r) dr \tag{2.8b}$$

$$[\mathbf{N}_{ij}]_{kl} = \int_{\mu_{P_{1i}}} N_{ij}(P_{1l})\, P_{1k}(r) dr \tag{2.8c}$$

$$[\mathbf{D^*}_{ij}]_{kl} = \int_{\mu_{P_{1i}}} D^*_{ij}(P_{0l})\, P_{1k}(r) dr. \tag{2.8d}$$

Consequently, the system to be solved reads $\mathbf{Zx} = \mathbf{b}$ with

$$\mathbf{Z} = \begin{bmatrix} \alpha_1\mathbf{N}_{11} & -2\mathbf{D^*}_{11} & -\sigma_2\mathbf{N}_{12} & \mathbf{D^*}_{12} & & & & \\ -2\mathbf{D}_{11} & \beta_1\mathbf{S}_{11} & \mathbf{D}_{12} & -\sigma_2^{-1}\mathbf{S}_{12} & & & & \\ -\sigma_2\mathbf{N}_{21} & \mathbf{D^*}_{21} & \alpha_2\mathbf{N}_{22} & -2\mathbf{D^*}_{22} & \cdots & & & \\ \mathbf{D_{21}} & -\sigma_2^{-1}\mathbf{S}_{21} & -2\mathbf{D}_{22} & \beta_2\mathbf{S}_{22} & \cdots & & & \\ & & \vdots & \vdots & \ddots & & & \\ & & & & & \alpha_{N-1}\mathbf{N}_{N-1,N-1} & 2\mathbf{D^*}_{N-1,N-1} & -\sigma_N\mathbf{N}_{N-1,N} \\ & & & & & -2\mathbf{D}_{N-1,N-1} & \beta_{N-1}\mathbf{S}_{N-1,N-1} & \mathbf{D}_{N-1,N} \\ & & & & & -\sigma_N\mathbf{N}_{N,N-1} & \mathbf{D}_{N,N-1} & \sigma_N\mathbf{N}_{N,N} \end{bmatrix} \tag{2.9}$$

and where

$$[\mathbf{x}]_{2l-1} = a_l \tag{2.10a}$$

$$[\mathbf{x}]_{2l} = b_l \tag{2.10b}$$

$$[\mathbf{b}]_{2k-1} = \int_{\mu_k} \left(\sigma_{k+1}^{-1} v_{k+1} - \sigma_k^{-1} v_k \right) P_{1k} \, dr \tag{2.11a}$$

$$[\mathbf{b}]_{2k} = \int_{t_k} \left(\partial_n v_{k+1} - \partial_n v_k \right) P_{0k} \, dr. \tag{2.11b}$$

In the following, the continuous operator associated to the matrix $\mathbf{Z}$ (obtained by replacing in (2.9) $\mathbf{D}$, $\mathbf{S}$, $\mathbf{N}$, and $\mathbf{D}^*$ with D, S, N, and D^*) will be denoted by Z.

2.3 A Calderon Preconditioner for the Symmetric Formulation

The high accuracy of the symmetric BEM formulation [2] has made of it a very popular tool for solving the EEG forward problem. However its system matrix suffers from ill-conditioning that can lead to the non-convergence of the employed iterative solver used to compute the solution [9]. Indeed, the operator S is compact [69]. This means that its spectrum will accumulate at zero when the mesh is refined and it will therefore have a condition number increasing inversely proportional to the average mesh length h. Moreover, the hypersingular operator N is an unbounded operator [69]. This implies that its condition number will also grow with $1/h$. Since these operators are the diagonal blocks of the matrix $\mathbf{Z}$ in (2.9) and the off-diagonal blocks of the matrix are smoothers, it follows that the overall conditioning of $\mathbf{Z}$ will increase when the mesh discretization will increase ($h \to 0$).

By leveraging on the Calderon identities, it is possible to build a preconditioner for the system matrix $\mathbf{Z}$. The rationale behind our strategy can be understood by considering the continuous operators first. The two Calderon identities that are relevant for our approach read [65]

$$S_{ii} N_{ii} = \frac{1}{4} I - D_{ii}^2 \tag{2.12a}$$

$$N_{ii} S_{ii} = \frac{1}{4} I - D_{ii}^{*2} \tag{2.12b}$$

where the symbol I stands for the identity operator. The spectral analysis of (2.12a) and (2.12b) shows that the operators $S_{ii}N_{ii}$ and $N_{ii}S_{ii}$ are well conditioned. Indeed, given that D and D^* are compact operators, then D_{ii}^2 and D_{ii}^{*2} are also compact operators as a product of two compact operators. Then the spectrum of D_{ii}^2 and D_{ii}^{*2} is bounded above and accumulates at zero. However, the presence of the identity operator in (2.12a) and (2.12b) guarantees that the spectrum of the operators $S_{ii}N_{ii}$ and $N_{ii}S_{ii}$ will be bounded from below by $1/4$. In other words, $S_{ii}N_{ii}$ and $N_{ii}S_{ii}$ are second kind operators whose spectrum accumulates at $1/4$. This property can be exploited to build a left preconditioner for the symmetric operator Z. We denote such a preconditioning operator by C and define it by

$$C = \begin{bmatrix} c_{11}S_{11} & c_{12}D_{11} & c_{13}S_{12} & c_{14}D_{12} & 0 & 0 & 0 \\ c_{21}D_{11}^* & c_{22}N_{11} & c_{23}D_{12}^* & c_{24}N_{12} & 0 & 0 & 0 \\ c_{31}S_{21} & c_{32}D_{21} & c_{33}S_{22} & c_{34}D_{22} & c_{35}S_{23} & c_{36}D_{23} & 0 \\ c_{41}D_{21}^* & c_{42}N_{21} & c_{43}D_{22}^* & c_{44}N_{22} & c_{45}D_{23}^* & c_{46}N_{23} & 0 \\ 0 & 0 & c_{53}S_{32} & c_{54}D_{32} & c_{55}S_{33} & c_{56}D_{33} & \cdots \\ 0 & 0 & c_{63}D_{32}^* & c_{64}N_{32} & c_{65}D_{33}^* & c_{66}N_{33} & \cdots \\ 0 & 0 & 0 & 0 & \vdots & \vdots & \ddots \end{bmatrix}. \tag{2.13}$$

where the constant coefficients c_{ij} accounting for the conductivity terms are the same as in (2.9). Then, as desired, CZ is a block operator exhibiting the Calderon identities (2.12a) and (2.12b) in its diagonal up to the multiplicative factor c_{ii}^2 as can be seen in (2.14).

$$CZ = \begin{bmatrix} c_{11}^2 S_{11}N_{11} + K_{11} & K_{12} & K_{13} & \cdots \\ K_{21} & c_{22}^2 N_{11}S_{11} + K_{22} & K_{23} & \cdots \\ K_{31} & K_{32} & c_{33}^2 S_{22}N_{22} + K_{33} & \cdots \\ \vdots & \vdots & \vdots & \ddots \end{bmatrix} \tag{2.14}$$

The terms denoted with K_{ij}, contain linear combinations of the compact operators $D_{ij}D_{jk}$, $S_{ij}N_{jk}$, $S_{ij}D_{jk}^*$, $D_{ij}S_{jk}$, $D_{ij}^*N_{jk}$, $N_{ij}D_{jk}$, $N_{ij}S_{jk}$ and $D_{ij}^*D_{jk}^*$. They read

$$K_{2n-1,2m-1} = \sum_{i=n-1}^{n+1} \chi_m(i)(c_{ni}c_{im}S_{ni}N_{im} + \chi_i c_{ni}c_{im}D_{ni}D_{im}) - c_{2n-1,2m-1}S_{nm}N_{nm}\delta_{nm} \tag{2.15a}$$

$$K_{2n,2m} = \sum_{i=n-1}^{n+1} \chi_m(i)(c_{ni}c_{im}D^*_{ni}D^*_{im} + \chi_i c_{ni}c_{im}N_{ni}S_{im}) - c_{2n,2m}N_{nm}S_{nm}\delta_{nm} \tag{2.15b}$$

$$K_{2n-1,2m} = \sum_{i=n-1}^{n+1} \chi_m(i)(c_{ni}c_{im}S_{ni}D^*_{im} + \chi_i c_{ni}c_{im}D_{ni}S_{im}) \tag{2.15c}$$

$$K_{2n,2m-1} = \sum_{i=n-1}^{n+1} \chi_m(i)(c_{ni}c_{im}D^*_{ni}N_{im} + \chi_i c_{ni}c_{im}N_{ni}D_{im}) \tag{2.15d}$$

where the symbols χ_i, $\chi_m(i)$ are given by

$$\chi_m(i) = \begin{cases} 1 & \text{if } |i-m| < 2 \\ 0 & otherwise \end{cases}, \tag{2.16}$$

$$\chi_i = \begin{cases} 1 & \text{if } i < N \\ 0 & otherwise \end{cases}, \tag{2.17}$$

and where δ_{nm} is the Kronecker's delta

$$\delta_{nm} = \begin{cases} 1 & \text{if } m = n \\ 0 & \text{otherwise} \end{cases}. \tag{2.18}$$

As shown previously, the terms $S_{ii}N_{ii}$ and $N_{ii}S_{ii}$ are second kind operator matrices well conditioned, as a consequence the terms $c_{ii}S_{ii}N_{ii}$ $c_{ii}N_{ii}S_{ii}$ will also be well conditioned with respect to the mesh parameter h since the c_{ii} are constant scalar terms. Then, writing

$$CZ = A + B$$

with

$$\begin{cases} [A]_{2l-1,2l-1} & = c^2_{2l-1,2l-1}S_{ll}N_{ll} \\ [A]_{2l,2l} & = c^2_{2l,2l}N_{ll}S_{ll} \\ [A]_{ij} & = 0 \text{ if } i \neq j \end{cases}$$

and B such that $[B]_{ij} = K_{ij}$, CZ can be seen as the sum of the well conditioned matrix A and a compact perturbation B (as the operators K_{ij} are compact operators). We can therefore expect the operator CZ to be well conditioned with respect to the mesh parameter. The proof of the compactness of the operators K_{ij} has been presented by Ms. A. Pillain in her doctoral thesis [60].

However, the condition number of CZ may still depend on the conductivities in the terms c_{ij}. Indeed, when substituting the terms $S_{ii}N_{ii}$ and $N_{ii}S_{ii}$ with the corresponding Calderon identities (2.12a) and (2.12b) respectively in A: $[A]_{2l-1,2l-1} = c^2_{2l-1,2l-1}\left(\frac{1}{4}I - D^2_{ii}\right)$, $[A]_{2l,2l} = c^2_{2l,2l}\left(\frac{1}{4}I - D^{*2}_{ii}\right)$, we obtain

$$CZ = c\frac{1}{4}I + cF + B \tag{2.19}$$

where c is given by $[c]_{ij} = c^2_{2l,2l}\delta_{ij}$ if $i = 2l$ and $c^2_{2l-1,2l-1}\delta_{ij}$ if $i = 2l - 1$ and where F contains the compact operators D^2_{ii} or D^{*2}_{ii} on its diagonal. Thus we can rewrite CZ as

$$CZ = c\frac{1}{4}I + M \tag{2.20}$$

with M compact. The operator CZ is then indeed a bounded second kind operator with a value of condition number which is independent of the mesh parameter, but that could still depend on the conductivity factors c_{ii}. These conductivity factors are given by $c_{2l-1,2l-1} = \sigma_l + \sigma_{l+1}$ and $c_{2l,2l} = \sigma_l^{-1} + \sigma_{l+1}^{-1}$. As a consequence, in the case of high conductivity contrast between two adjacent domains, i.e. asymptotically, when $\frac{\sigma_i}{\sigma_j} \to \infty$, that is $\left(\sigma_i + \sigma_j\right) \to \infty$ when $\sigma_i \to \infty$ or $\left(\sigma_i^{-1} + \sigma_j^{-1}\right) \to \infty$ when $\sigma_j \to 0$, the condition number of the system matrix will grow as a function of $\frac{\sigma_i}{\sigma_j}$. Because of high conductivity contrast between the brain and the skull [47, 81], this undesirable situation is likely to appear when solving the EEG forward problem. To solve also this problem, we will rescale with respect to the conductivity both the symmetric operator Z and the preconditioner C using a diagonal

operator Q whose diagonal elements Q_{ii} are given by

$$\begin{cases} Q_{ii} = \dfrac{1}{\sqrt{max(\sigma_i, \sigma_{i+1})}} & \text{if } i \text{ is odd} \\ Q_{ii} = \sqrt{min(\sigma_i, \sigma_{i+1})} & \text{if } i \text{ is even} \end{cases} \tag{2.21}$$

We then define a rescaled symmetric operator Z_q as

$$Z_q = QZQ \tag{2.22}$$

and a rescaled preconditioner C_q

$$C_q = QCQ. \tag{2.23}$$

An asymptotic analysis shows that the two rescaled operators above have a conditioning uniform with the conductivity ratio $\frac{\sigma_i}{\sigma_j}$ between two adjacent domains. For example, in the canonical case of a three layered domain where $\sigma_1 = \sigma_3 = 1$ and $\sigma_2 \ll \sigma_1$: when observing the asymptotic behavior, i.e. when $\sigma_2 \to 0$, Z_q reads

$$\begin{bmatrix} N_{11} & 0 & 0 & 0 & 0 \\ 0 & S_{11} & 0 & -S_{12} & 0 \\ 0 & 0 & N_{22} & 0 & -N_{23} \\ 0 & -S_{21} & 0 & S_{22} & 0 \\ 0 & 0 & -N_{32} & 0 & N_{33} \end{bmatrix} \tag{2.24}$$

which is clearly uniform with the values of conductivity.

Finally, for addressing both the mesh parameter and the conductivity related ill-conditioning, the Calderon preconditioning and the rescaling should be performed concurrently. In other words, the preconditioned symmetric operator we propose reads

$$Z_c = QCQQZQ. \tag{2.25}$$

which is a well conditioned operator with respect to both the mesh parameter h and the conductivity contrast.

2.4 Discretization of the Calderon Preconditioner and Solution of the Preconditioned Symmetric Formulation

In order to solve the preconditioned symmetric integral equation, the proposed multiplicative preconditioner C has to be discretized. This discretization should be carried out with care. In fact, the preconditioned operator in (2.25) will contain operator products which will not directly translate into matrix products in the general case. A suitable choice of basis functions should be made to guarantee that this could instead be the case here.

To fix the ideas, we could consider the discretization of the operator product $N_{11}S_{11}$ appearing in the top-left block of Z_c. The matrix $\mathbf{S_{11}}$ is obtained by using source and testing functions in P_0 while the matrix $\mathbf{N_{11}}$ is obtained by using source and testing functions in P_1. Yet the number of vertices N_t and the number of cells that defines the dimensions of the space P_1 and P_0 are different. As a consequence, the blocks $\mathbf{N_{11}}$ and $\mathbf{S_{11}}$ do not have compatible shapes and cannot be multiplied. Furthermore, the basis functions used for discretizing N_{11} and S_{11} must satisfy appropriate inf-sup conditions with respect to the duality pairing $\langle v, w\rangle : H^{1/2}(\Gamma_1)\times H^{-1/2}(\Gamma_1) \rightarrow \mathbb{R}$ (the reader should refer to [40] for further technical details on this topic). This condition enables to get a stable condition number for the Gram matrices, necessarily present in the discretized system as they orthonormalize the two chosen basis and testing functions sets.

To properly take care of this fact, we propose to discretize the preconditioner C on the dual mesh M_Ω^* of the standard mesh M_Ω and to leverage on the dual basis functions introduced in [12] on such a mesh. In the dual mesh, each vertex corresponds to a cell of the standard mesh and vice-versa. This means that in M_Ω^* we can build a discrete space in $H^{1/2}(\Gamma)$ which has the same dimension as the discrete space associated to $H^{-1/2}(\Gamma)$ in M_Ω and vice-versa. Moreover, the dual basis functions introduced by [12] abide by the inf-sup conditions required to obtain stable discrete products [40]. As a consequence, the discretization of the preconditioner operator C by using these basis functions enables to

perform the matrix multiplication associated to the operator multiplication $C_q Z_q$ in such a way that the spectral bounds holding for the continuous operator products will translate in well-conditioned matrix products.

The dual mesh M_Ω^* can be obtained by barycentric refinement of the standard mesh M_Ω by dividing the triangles t_k into six smaller triangles t_{bk} whose edges are built by tracing the medians of the standard triangles t_k [12]. The cells c_k of M_Ω^* are defined as the set of triangle t_{bk} sharing a common vertex v_k of M_Ω. The vertices of M_Ω^* are the barycenters b_k of the triangles t_k in M_Ω. The reader should refer to Fig. 2.2 for an example of such a refinement.

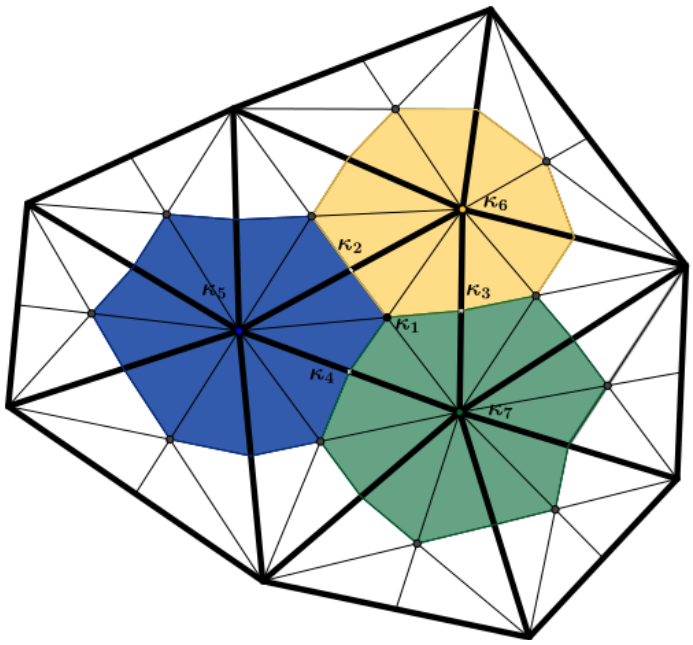

Figure 2.2: Standard Mesh in bold lines, its barycentric refinement in thin lines. Three cells of the dual mesh are evidenced. The coefficients κ are the coefficients used in the linear combination of primal P_1 functions to build the dual $\tilde{P}_1$ functions: $\kappa_1 = 1$, $\kappa_i = 1/2$ if $i \in 2, 3, 4$ and $\kappa_i = 1/t$ if $i \in 5, 6, 7$, with t the number of triangles in M_Ω sharing the corresponding node.

In M_Ω^*, we define the dual piecewise linear functions $\tilde{P}_1 = span\{\tilde{P}_{1_k}\}_{k=1}^{N_t}$ obtained with a linear combination of P_1 functions built on the barycentric refined mesh [12]. A dual piecewise linear function is shown Fig. 2.3d. The coefficients of the linear combination are

shown Fig. 2.2. The support of $\tilde{P}_{1_i}$ is denoted $\mu_{\tilde{P}_{1_i}}$. The dual piecewise constant functions in $\tilde{P}_0$, denoted $\tilde{P}_{0k}$, are the constant functions equal to $1/A_{c_k}$ on the cell c_k, whose area is A_{c_k}, of M^*_Ω and equal to zero elsewhere. A dual piecewise constant function is shown Fig. 2.3c.

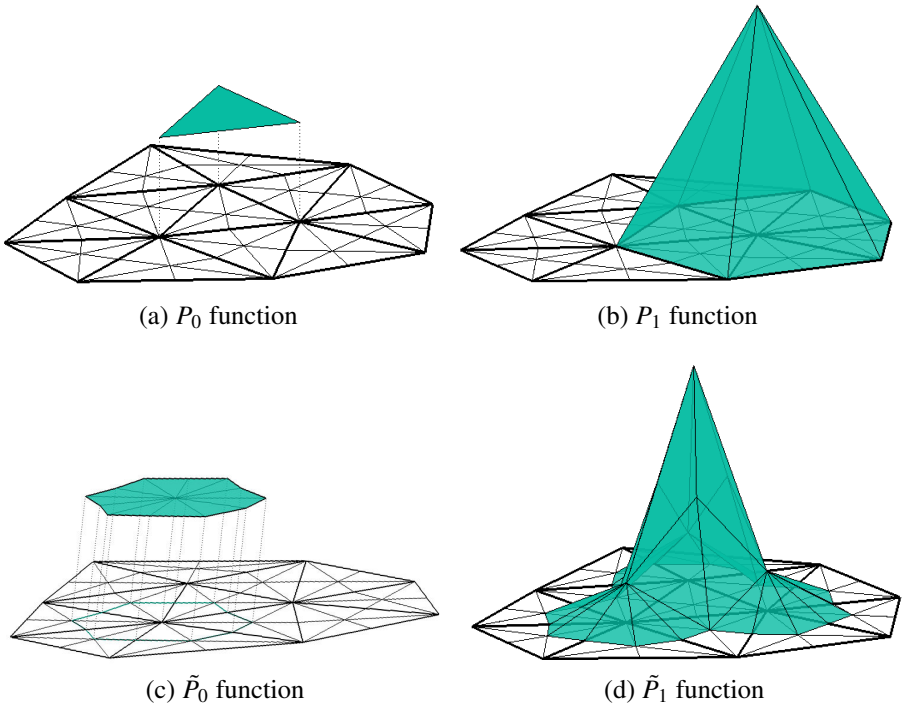

(a) P_0 function (b) P_1 function

(c) $\tilde{P}_0$ function (d) $\tilde{P}_1$ function

Figure 2.3: Basis and testing functions, in the standard mesh (2.3a, 2.3b) and in the dual mesh (2.3c, 2.3d)

Then the operators matrices used to build $\mathbf{C}$ are given by:

$$[\tilde{\mathbf{D}}_{ij}]_{kl} = \int_{c_k} D_{ij}(\tilde{P}_{1l})\, \tilde{P}_{0k}(r)dr \tag{2.26a}$$

$$[\tilde{\mathbf{S}}_{ij}]_{kl} = \int_{c_k} S_{ij}(\tilde{P}_{0l})\tilde{P}_{0k}(r)dr \tag{2.26b}$$

$$[\tilde{\mathbf{N}}_{ij}]_{kl} = \int_{\mu_{\tilde{P}_{1k}}} N_{ij}(\tilde{P}_{1l})\tilde{P}_{1k}(r)dr \tag{2.26c}$$

$$[\tilde{\mathbf{D}}^*_{ij}]_{kl} = \int_{\mu_{\tilde{P}_{1k}}} D^*_{ij}(\tilde{P}_{0l})\tilde{P}_{1k}(r)dr. \tag{2.26d}$$

and the discretized preconditioner $\tilde{\mathbf{C}}$ is made explicit in (2.27).

$$\tilde{\mathbf{C}} = \begin{bmatrix} c_{11}\tilde{\mathbf{S}}_{\mathbf{11}} & c_{12}\tilde{\mathbf{D}}_{\mathbf{11}} & c_{13}\tilde{\mathbf{S}}_{\mathbf{12}} & c_{14}\tilde{\mathbf{D}}_{\mathbf{12}} & 0 & 0 & 0 \\ c_{21}\tilde{\mathbf{D}}^{*}_{\mathbf{11}} & c_{22}\tilde{\mathbf{N}}_{\mathbf{11}} & c_{23}\tilde{\mathbf{D}}^{*}_{\mathbf{12}} & c_{24}\tilde{\mathbf{N}}_{\mathbf{12}} & 0 & 0 & 0 \\ c_{31}\tilde{\mathbf{S}}_{\mathbf{21}} & c_{32}\tilde{\mathbf{D}}_{\mathbf{21}} & c_{33}\tilde{\mathbf{S}}_{\mathbf{22}} & c_{34}\tilde{\mathbf{D}}_{\mathbf{22}} & c_{35}\tilde{\mathbf{S}}_{\mathbf{23}} & c_{36}\tilde{\mathbf{D}}_{\mathbf{23}} & 0 \\ c_{41}\tilde{\mathbf{D}}^{*}_{\mathbf{21}} & c_{42}\tilde{\mathbf{N}}_{\mathbf{21}} & c_{43}\tilde{\mathbf{D}}^{*}_{\mathbf{22}} & c_{44}\tilde{\mathbf{N}}_{\mathbf{22}} & c_{45}\tilde{\mathbf{D}}^{*}_{\mathbf{23}} & c_{46}\tilde{\mathbf{N}}_{\mathbf{23}} & 0 \\ 0 & 0 & c_{53}\tilde{\mathbf{S}}_{\mathbf{32}} & c_{54}\tilde{\mathbf{D}}_{\mathbf{32}} & c_{55}\tilde{\mathbf{S}}_{\mathbf{33}} & c_{56}\tilde{\mathbf{D}}_{\mathbf{33}} & \cdots \\ 0 & 0 & c_{63}\tilde{\mathbf{D}}^{*}_{\mathbf{32}} & c_{64}\tilde{\mathbf{N}}_{\mathbf{32}} & c_{65}\tilde{\mathbf{D}}^{*}_{\mathbf{33}} & c_{66}\tilde{\mathbf{N}}_{\mathbf{33}} & \cdots \\ 0 & 0 & 0 & 0 & \vdots & \vdots & \ddots \end{bmatrix} \tag{2.27}$$

The final preconditioner is then obtained by introducing the necessary rescaling to obtain a uniform conditioning with respect to the conductivity profiles (according to the analysis of the previous section). We then define $\tilde{\mathbf{C}}_{\mathbf{q}}$ such that $\tilde{\mathbf{C}}_{\mathbf{q}} = \mathbf{Q}\tilde{\mathbf{C}}\mathbf{Q}$ where $\mathbf{Q}$ is the diagonal matrix defined in accordance to (2.21).

In order to perform the multiplication of matrices with two different discretizations, a Gram matrix $\mathbf{G}$ to link them is necessary. This Gram matrix is computed by taking the scalar product between the trial functions of one operator and the test functions of the other operator. Hence, the computation of the Gram matrix does not require the evaluation of any operator. Additionally, it is almost diagonal, therefore the computational cost is very low. This matrix is obtained as

$$[\mathbf{G}_{2i-1}]_{kl} = \int_{\mu_{\tilde{P}_{1k}}} (\tilde{P_{0l}})\, P_{1k}(r) dr \tag{2.28a}$$

$$[\mathbf{G}_{2i}]_{kl} = \int_{t_k} (\tilde{P_{1l}})\, P_{0k}(r) dr. \tag{2.28b}$$

Finally, the preconditioned system matrix is given by

$$\mathbf{Z}_c = \mathbf{Q}\tilde{\mathbf{C}}\mathbf{Q}\mathbf{G}^{-1}\mathbf{Q}\mathbf{Z}\mathbf{Q} \tag{2.29}$$

or, more compactly

$$\mathbf{Z}_c = \tilde{\mathbf{C}}_{\mathbf{q}}\mathbf{G}^{-1}\mathbf{Z}_{\mathbf{q}} \tag{2.30}$$

The solution of the preconditioned symmetric formulation is then obtained by solving the following system $\mathbf{Z}_c\mathbf{y} = \mathbf{C}_q\mathbf{G}^{-1}\mathbf{Q}\mathbf{b}$ and $\mathbf{x}$ is obtained with $\mathbf{x} = \mathbf{Q}\mathbf{y}$.

Summarizing, the Calderon preconditioning strategy is multiplicative in nature. Its aim is to build a preconditioning operator spectrally equivalent to the inverse of the original operator. Thus, once this operator is built, multiplying the ill-conditioned operator with it yields an operator spectrally equivalent to an identity. The preconditioning operator is built on a dual mesh in order to allow matrix multiplication and stability. Moreover, regularization matrices are added in order to get a condition number independent from the conductivity ratio. In a nutshell, the steps are:

1. Compute the standard symmetric system matrix $\mathbf{Z}$;
2. Compute the Calderon preconditioning matrix $\tilde{\mathbf{C}}$ on the dual mesh;
3. Compute the Gram matrices linking the dual and standard discretization, known as Gram matrices $\mathbf{G}$;
4. Normalize the operator $\tilde{\mathbf{C}}$ and $\mathbf{Z}$ with the regularization matrices $\mathbf{Q}$;
5. Perform the multiplication $\mathbf{Z}_c = \mathbf{Q}\tilde{\mathbf{C}}\mathbf{Q}\mathbf{G}^{-1}\mathbf{Q}\mathbf{Z}\mathbf{Q}$;
6. The right hand side b must be modified accordingly : compute $\mathbf{b}_c = \mathbf{Q}\tilde{\mathbf{C}}\mathbf{Q}\mathbf{G}^{-1}\mathbf{Q}\mathbf{b}$;
7. Solve the system $\mathbf{Z}_c\mathbf{y} = \mathbf{b}_c$;
8. Get the solution using $\mathbf{x} = \mathbf{Q}\mathbf{y}$.

2.5 Numerical Results

The new Calderon regularized symmetric formulation proposed in this work has been first tested on the canonical scenario of three homogeneous and concentric spheres of radii 0.8, 0.9, and 1 respectively. Indeed, in the case of homogeneous nested spheres, an analytical solution is available as a reference [22, 82], this solution will be denoted with V_{ref}. In these simulations, a single dipole source is placed in (0, 0, 0.5) with a dipole moment of (0, 0, 1).

As a complement to these results, to validate the new formulation on a real case scenario, the new formulation has been tested also on a realistic head model obtained from MRI data.

2.5.1 Accuracy Assessments

A first set of simulations was performed to assess the accuracy of the proposed method. The assessment parameter is the relative error computed as $RE = \frac{||V_{num} - V_{ref}||}{||V_{ref}||}$ where V_{num} refers to the numerical solution obtained using either the proposed Calderon preconditioned symmetric formulation or the standard symmetric formulation.

The accuracy with respect to the refinement of the mesh was first evaluated. In this case, the conductivities of the three different domains are fixed to 1, 0.0125 and 1 respectively. The average length of the triangles (h) is decreased from 0.7 to 0.14. The results of this simulation are shown in Fig. 2.4. It is clear that the relative error of the symmetric and the Calderon-Symmetric approach are the same and that they provide a better accuracy than the adjoint double layer and double layer approach.

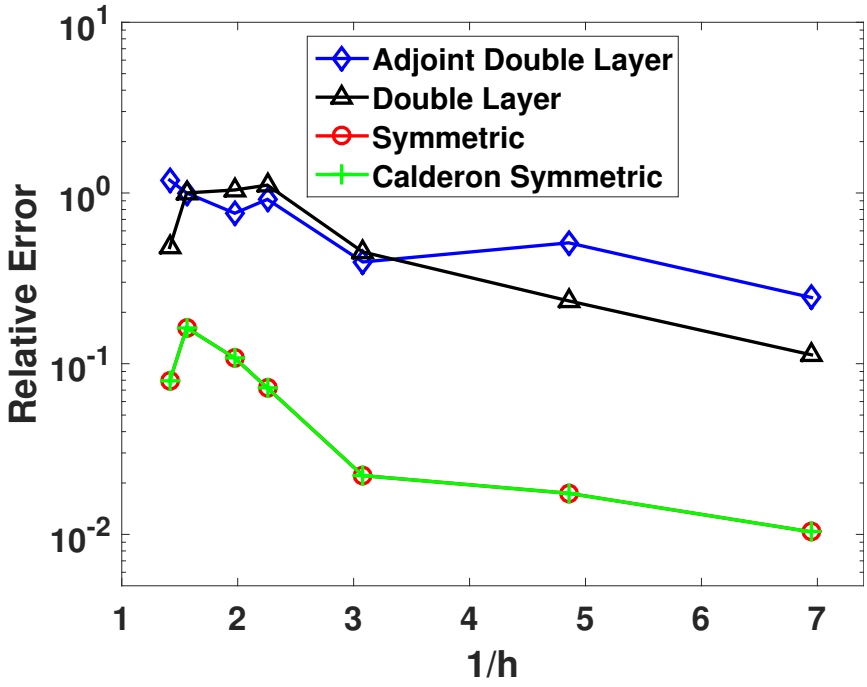

Figure 2.4: Relative error with respect to the mesh refinement. The average length of a cell is given by h

There is no consensus in literature about the value of the skull conductivity [47, 81, 61]. The value of the conductivity is given relatively to the conductivity of the brain and of the scalp. After fixing these latter to 1, we then study the accuracy of the solution with respect to the conductivity contrast $\sigma_{ratio} = \frac{\sigma_1}{\sigma_2}$. The results of this study are presented in Fig. 2.5. Here again, the relative error of the adjoint double layer and double layer formulations is higher than the relative error provided by the two symmetric formulations. We also note that the Calderon-symmetric approach provides the same relative error than the usual symmetric approach.

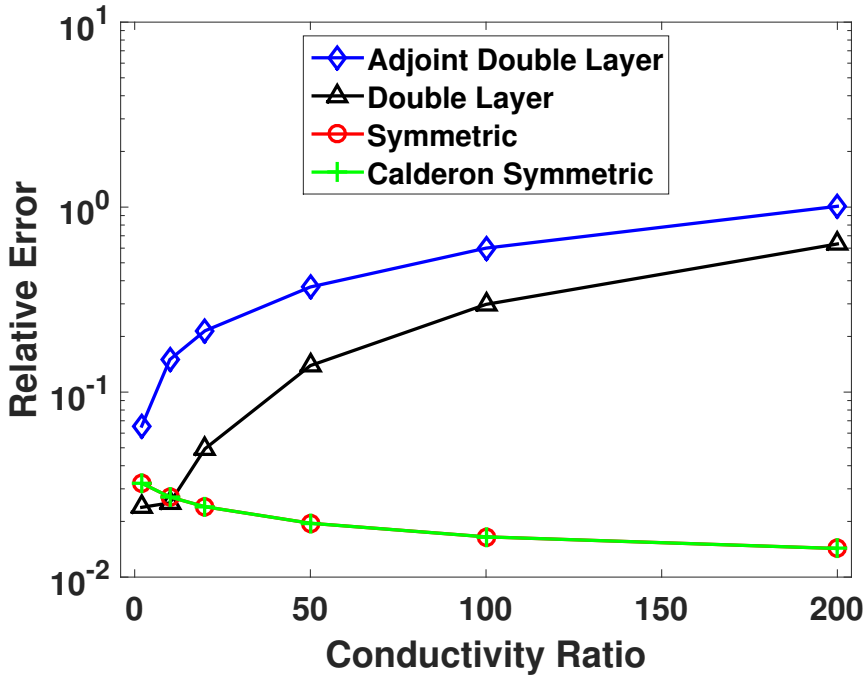

Figure 2.5: Relative Error with respect to the conductivity ratio σ_r

2.5.2 Condition Number Assessments

As verified in the previous section, the newly proposed formulation preserves the high levels of accuracy of the standard symmetric approach. As a key advantage with respect to the standard symmetric formulation, however, a regularized conditioning behavior is expected. For the same canonical scenario as in the previous section, Fig. 2.6 shows that when refin-

ing the mesh, the condition number of the usual symmetric approach increases, as expected, while the Calderon preconditioned approach provides a stable condition number.

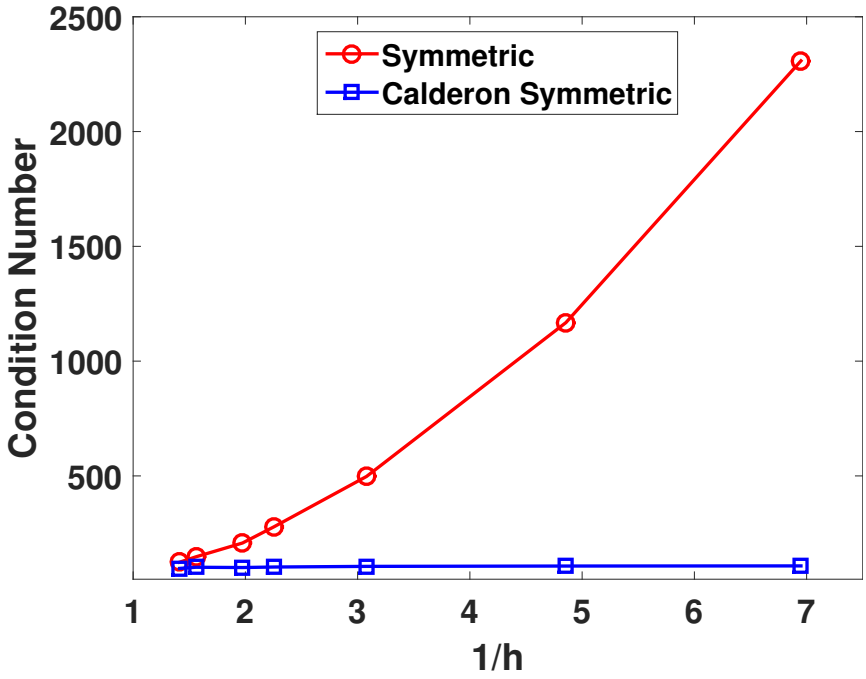

Figure 2.6: Condition Number with respect to the mesh refinement.

Complementarily, Fig. 2.7 shows the variation of the condition number as a function of the brain conductivity ratio. Again, the results match the expected behavior since the condition number of the standard symmetric approach staggers with σ_r while the newly proposed formulation method has a bounded condition number.

2.5.3 Assessments on a MRI-obtained head model

To show the advantages of the new formulation in a real case scenario, we have assessed the performance of the new technique on a head model obtained from MRI data [55]. The segmented model comprised of three layers corresponding to brain, skull, and scalp. The head model and the associated computed potential are shown in Fig. 2.8. To verify that the Calderon preconditioned symmetric formulation delivers the same solution of the standard symmetric formulation we have compared the potential values for both formulations at the

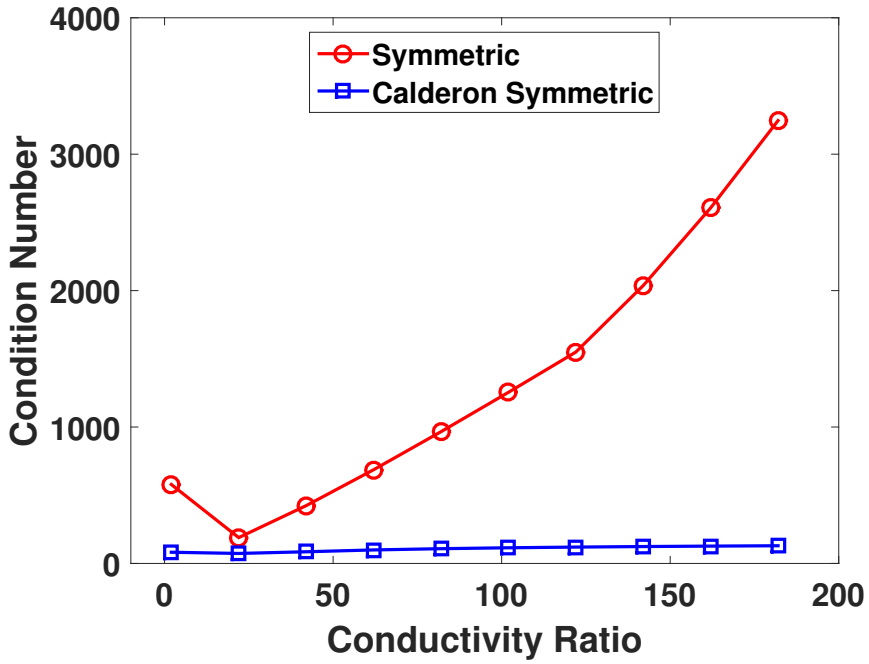

Figure 2.7: Condition Number with respect to the conductivity ratio σ_r

position of the EEG electrodes (EGI 256-sensors electrodes' positions have been used). The results of these comparisons are shown in Fig. 2.9. It is clear that the two formulations deliver perfectly matching solutions. The advantage of using the Calderon preconditioned symmetric formulation however, is evident from Fig. 2.10 that shows the convergence of the residual error of the iterative solver (conjugate gradient square) with respect to the number of iterations. It can be seen that the Calderon symmetric approach converges 40 times faster than the non-preconditionned symmetric approach.

2.5.4 Discussion

The numerical results show that the accuracy of the symmetric formulation is preserved in its Calderon preconditioned version presented in this work both when the mesh is refined (Fig. 2.4) and when conductivity contrast between two layers increases (Fig. 2.5). The new preconditioned equation, however, shows a low and stable condition number when the mesh is refined unlike the unpreconditioned standard symmetric formulation for which

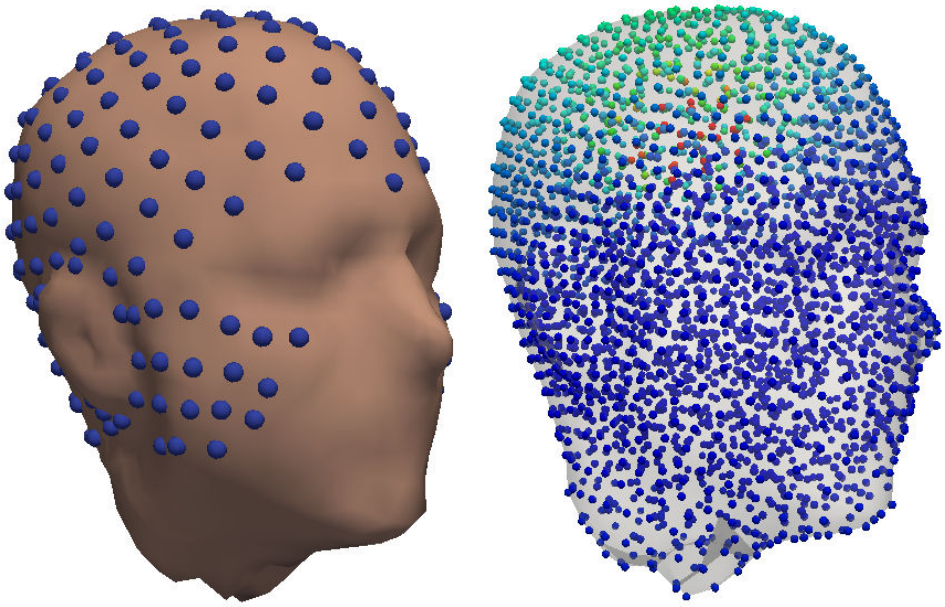

(a) Head model and EEG electrodes. (b) Calculated electric potential.

Figure 2.8: MRI-obtained head model

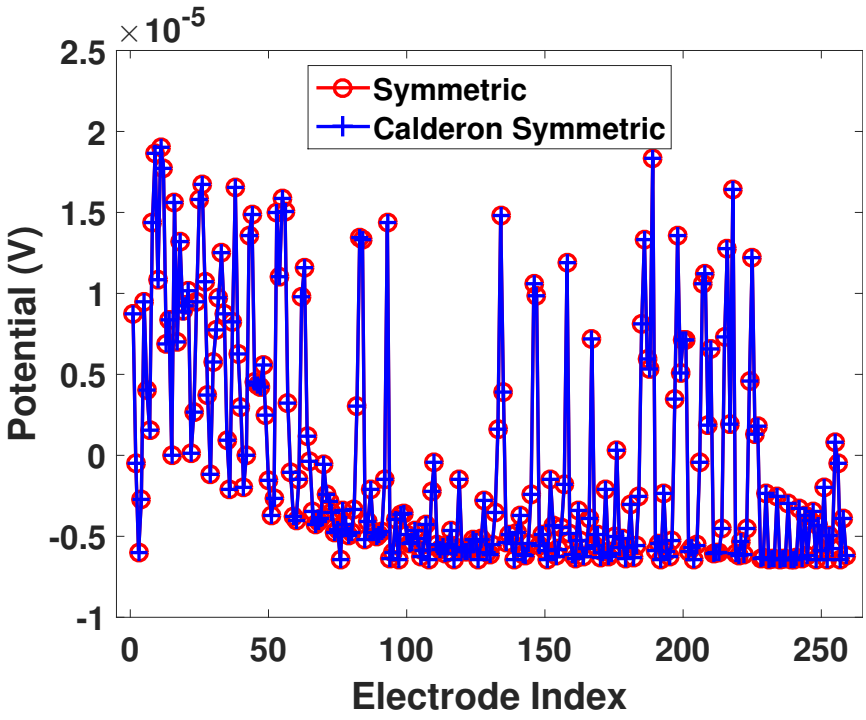

Figure 2.9: Validation of the new formulation via a potential comparison at the EEG electrodes' position (dipolar source).

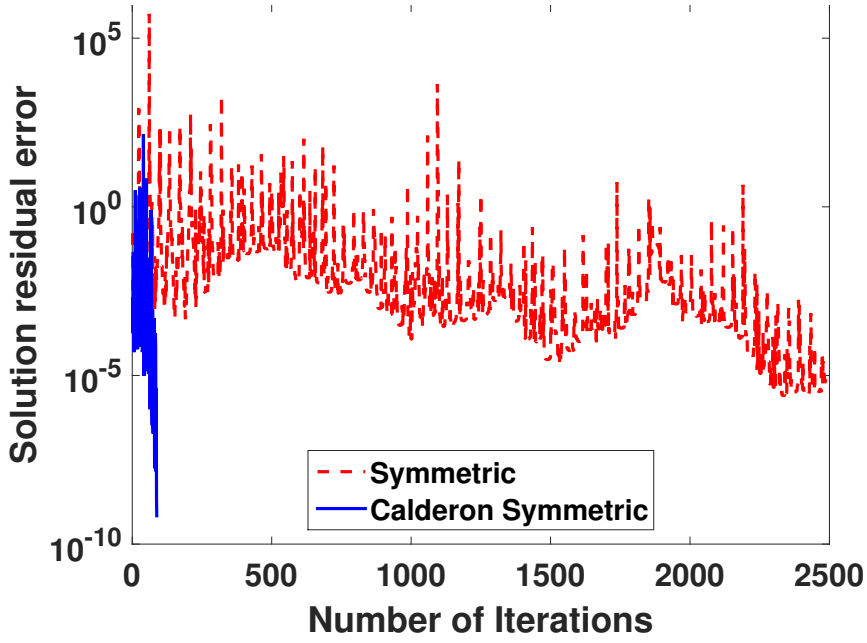

Figure 2.10: Convergence of the iterative solver for the preconditioned and not preconditioned symmetric approach

the condition number grows rapidly with $1/h$ (Fig. 2.6). Moreover, the conditioning is maintained stable also as a function of the conductivity ratio as the numerical results in Fig. 2.7 show.

2.6 Conclusion

Leveraging on Calderon identities, in this work we have proposed a Calderon preconditioned symmetric formulation for the EEG forward problem. When compared to the standard symmetric equation, the proposed formulation has the advantage of showing constant condition numbers both as a function of mesh refinement and of conductivity contrast, this while providing the same accuracy for which the standard symmetric formulation is widely used. This means that, for a given relative accuracy of the solution, the formulation proposed here will converge substantially faster than the standard one as the numerical results have shown. Moreover, the proposed approach can be easily integrated into existing symmetric formulation implementations as it requires only to multiply the standard symmetric

system matrix with a dual matrix that can be obtained with the same numerical technology used for the standard symmetric formulation. Numerical results have substantiated all theoretical claims and have shown the practical impact of the newly proposed scheme.

Chapter 3

Accelerating the Calderon-Symmetric Formulation with the Adaptive Cross Approximation method

This chapter presents the implementation of the adaptive cross approximation (ACA) fast solver for block operator matrices. The fast solver is based on a hierarchical multilevel partitioning of the domain and a kernel free low-rank compression. This yields a storage and computational complexity of $O(N\log(N))$ *(where N is the number of unknowns). We describe in detail the method, starting from the data structure necessary for ACA. We then explain the principle of the low-rank compression. Finally, we use this algorithm to speed up the Calderon-Symmetric formulation. The numerical results show the effectiveness of the algorithm for this case.*

3.1 Introduction

The fast solvers for integral equations are algorithms that speed up the time necessary to get the solution of a matrix system. In general, the fast solvers compute a compressed version of the matrix allowing to implement a fast matrix-vector product (MVP). When the solution is computed using an iterative solver, the improvement of the required time to perform MVP impacts directly the overall time of the solution system. Moreover, using a fast solver reduces the time to compute the system matrix entries as well as the storage

memory since it does not require the computation of all the entries of the matrix.

Without fast solving technique, the MVP for dense matrix has $O(N^2)$ complexity, where N is the number of unknowns. Several techniques have been used to reduce this complexity, for example: the precorrected fast Fourier transform (pFFT) method [59], the adaptive integral method (AIM) [76] and the multilevel fast multipole method (ML-FMM)[68], among others. In this chapter, we will focus on the adaptive cross approximation (ACA) algorithm [11]. Indeed, this fast solver has a $O(N\log(N))$ complexity when the system matrix entries are obtained using an integral operator with an asymptotically smooth kernel [83], which is the case of the EEG symmetric formulation system matrix. The ACA is based on a hierarchical division of the domain. Separating into far interacting and near interacting sources yields a fast computation of the matrix in a compressed fashion based on a kernel free low-rank decomposition. This fashion allows a fast matrix-vector multiplication.

This chapter is divided as follows. First, we present the hierarchical partitioning used to create the data structure. In section 3.3 is described the low-rank compression. We then use the data structure and the low-rank compression to explain the multilevel method in section 3.4. Finally, in section 3.5 we present the implementation of the ACA method for the Calderon-symmetric formulation, as well as numerical results that prove the practical impact of the fast solver.

3.2 Hierarchical partitioning

The first step in order to use a fast multipole method is the construction of a hierarchical data structure of the mesh. For this purpose an octree partitioning is used.

We start by creating a box surrounding the mesh that contains all the elements of the domain. This stage is the level 0 of the octree as shows figure 3.1a. In figure 3.1b is presented the level 1 of the partinioning. Here, the original box has been divided into 8 boxes, each box containing a certain number of elements. We call $K_i(b)$ the number of elements

contained in the box b of the level i. We define $K_i^M = max(K_i(b))$ the maximum number of elements within a box of the level i. The level 2 shown in figure 3.1c is constructed in the same manner, subdividing each box of the level 1 that contains elements into 8 boxes. The other levels of the octree are constructed following this pattern. The recursion stops when the number of elements in a box of the constructed level reaches the desired number K_{max}. Calling L the finest level, this means that the process stops when $K_L^M \leq K_{max}$.

For uniform meshes, at each level i we have

$$K_i^M \approx \frac{N}{8^i} \tag{3.1}$$

where N is the total number of elements of the mesh. Therefore, the finest level L for a desire K_{max} can be approximated as

$$L \approx \log_8 N - \log_8 K_{max} \tag{3.2}$$

which yields an $O(\log N)$ complexity.

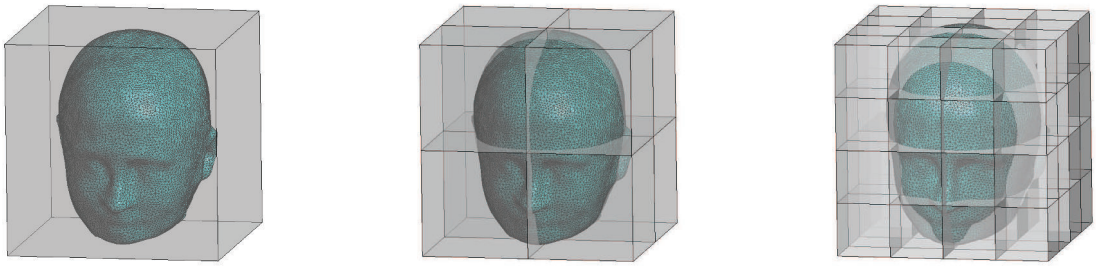

(a) Level 0 (b) Level 1 (c) Level 2

Figure 3.1: Octree partitioning

A node of the octree is a box containing elements at any level. Figure 3.2 presents a hierarchical representation of the octree. We call a relation between the nodes and their subdivisions a Father-Son relation. The boxes in level l created by subdividing the box b_j^{l-1} are called the sons of b_j^{l-1}, while b_j^{l-1} is called the father of $\{b_j^l\}_{i=1,2,...,8}$. The nodes

$\{b_j^l\}_{j=1,2,\ldots,8}$ are called siblings. The node of level 0 does not have a Father and it is called *Root*. Moreover, a node without sons is called *Leaf*.

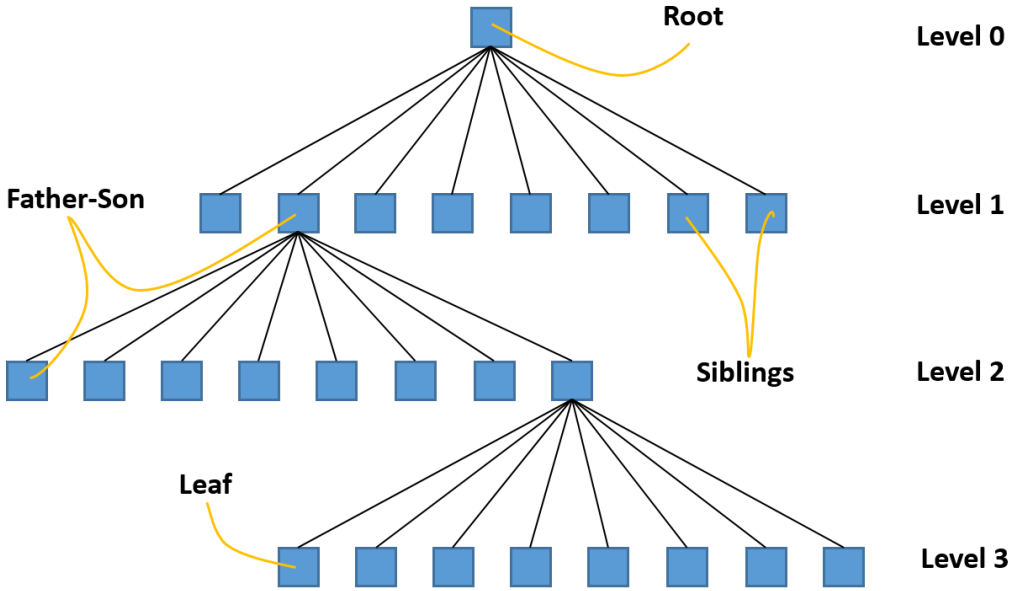

Figure 3.2: Hierarchical relations of the Octree.

3.3 Compression of low-rank matrices

Let $\mathbf{A}$ be an $n \times m$ low-rank matrix. Let's call r the effective rank of $\mathbf{A}$ so that the matrix is approximated as

$$\hat{\mathbf{A}} = \mathbf{U}\mathbf{V}^T \tag{3.3}$$

where $\mathbf{U}$ and $\mathbf{V}$ are matrices with dimensions $n \times r$ and $m \times r$ with ε a chosen tolerance such that

$$\| \mathbf{A} - \hat{\mathbf{A}} \| \leq \varepsilon \| \mathbf{A} \| \tag{3.4}$$

This shows that the matrix $\mathbf{A}$ can be stored using $(n+m) \times r$ elements instead of $n \times m$. This affects directly the matrix vector product (MVP) as well. Indeed, if $\mathbf{b}$ is a vector of dimension m, the multiplication $\mathbf{y} = \mathbf{A}\mathbf{b}$ has an order $O(nm)$, whereas the multiplication $\hat{\mathbf{y}} = \hat{\mathbf{A}}\mathbf{b} = \mathbf{U}\mathbf{V}^T\mathbf{b}$ can be done in two parts. First perform $\hat{\mathbf{y}}' = \mathbf{V}^T\mathbf{b}$ with $O(mr)$ complexity.

Then , perform $\hat{\mathbf{y}} = \mathbf{U}\hat{\mathbf{y}}'$ with $O(nr)$ complexity. Overall, this multiplication yields a cost of $O((n+m)r)$.

The matrices $\mathbf{U}$ and $\mathbf{V}$, that provide the best approximation with an optimal rank r for an accuracy ε, are computed using the singular value decomposition (SVD). Unfortunately, this method has the high computational cost of $O(nm^2)$. Hence, we cannot apply the method directly to the matrix $\mathbf{A}$. Instead, we can use a less expensive method to compute $\mathbf{U}_0$ and $\mathbf{V}_0$ with rank r_0. We then use these matrices to compute the SVD in a reduced complexity to get $\mathbf{U}$ and $\mathbf{V}$.

The matrices $\mathbf{U}_0$ and $\mathbf{V}_0^T$ are obtained with the following general procedure. We select r_0 independent columns of the matrix $\mathbf{A}$ that form the matrix $\mathbf{U}_0$. We then create the matrix $\mathbf{T}$ with r_0 independent rows of $\mathbf{A}$. The intersections of these selected rows and columns are stored in the matrix $\mathbf{P}$, and we get $\mathbf{V}_0 = \mathbf{P}^{-1}\mathbf{T}$. The specific ACA algorithm works as the general procedure described before and, additionally, adds a pivoting strategy in order to improve the numerical stability. This method computes only the necessary rows and columns of the matrix. In each iteration, the algorithm verifies the approximation matrix until the accuracy ε is reached getting a rank r_0. The algorithm is fully described in [84].

Now, the SVD is applied as follows. We start by computing a QR decomposition of the matrices $\mathbf{U}_0$ and $\mathbf{V}_0^T$

$$\begin{aligned} \mathbf{U}_0 &= \mathbf{Q}_U\mathbf{R}_U \\ \mathbf{V}_0 &= \mathbf{Q}_V\mathbf{R}_V. \end{aligned} \tag{3.5}$$

The cost of this procedure is $O((n+m)r_0^2)$. Moreover, the rank of the matrices $\mathbf{Q}_U$, $\mathbf{R}_U$, $\mathbf{Q}_V$ and $\mathbf{R}_V$ is the optimal rank r. Hence, the SVD of the product $\mathbf{R}_U\mathbf{R}_V$ is computed in a reduced complexity of $O(r^3)$ as

$$\mathbf{R}_U\mathbf{R}_V^T = \mathbf{U}_S\mathbf{S}\mathbf{V}_S^T \tag{3.6}$$

Finally, we approximate the low-rank matrix $\mathbf{A}$ as

$$\hat{\mathbf{A}} = \mathbf{U}\mathbf{V}^T. \tag{3.7}$$

where

$$\mathbf{U} = \mathbf{Q}_U \mathbf{U}_S$$
$$\mathbf{V} = \mathbf{S}\mathbf{Q}_V \mathbf{V}_S \tag{3.8}$$

These new matrices have an optimal rank r.

3.4 Computation of the compressed matrix

The ACA method computes an operator matrix in a compressed form, reducing the storage memory and computation time of the MVP. This method can be applied to operators with asymptotically smooth integral kernels.

We start by making some definitions in order to explain the multilevel computation. Let b_i be a box at level i of an octree. The *near neighbor* group are the boxes of level i that share a vertex or an edge with b_i. Otherwise, they are called *well separated* group of the box b_i. The boxes of level i that are well separated but whose fathers are near neighbors of the father of b_i are called *far interacting* group. Figure 3.3 illustrates these definitions using a quadtree, which is the 2D version of an octree.

Let Z be an operator with asymptotically smooth kernel [33] defined in the boundary $\partial\Omega = \Gamma$ of the domain Ω. We divide the boundary $\Gamma = \bigcup_{i=1}^{N} \Gamma_i$ creating a mesh with N elements. By using the local functions $f_i(\mathbf{r})$ and $g_i(\mathbf{r})$ defined in each subdomain Γ_i, the operator Z is discretized as a dense matrix $\mathbf{Z}$, whose elements are

$$\mathbf{Z}_{ij} = \langle g_i, Z f_j \rangle \tag{3.9}$$

with $\langle \cdot, \cdot \rangle$ the $\boldsymbol{L}^2(\Gamma)$ scalar product. The computational cost to obtain this matrix is $O(N^2)$ as well as his MVP. Therefore, the computation of the dense matrix is unsuitable for large N. Instead, the operator Z can be computed in a compressed fashion using the ACA method, which uses a hierarchical multilevel partitioning and a low-rank compression. Hence, the matrix can be computed as

$$\tilde{\mathbf{Z}} = \mathbf{Z}_n + \mathbf{Z}_f \tag{3.10}$$

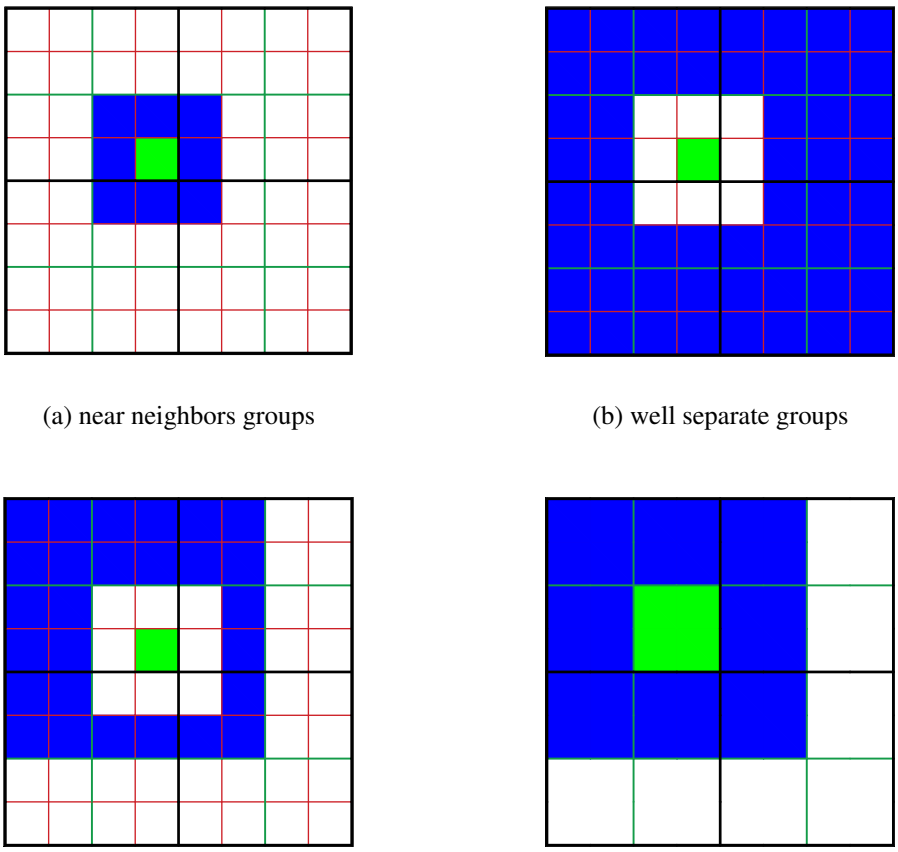

(a) near neighbors groups

(b) well separate groups

(c) far interacting groups

(d) near neigbors of the father

Figure 3.3: Groups of the octree

where the matrix $\mathbf{Z}_n$ corresponds to the near interactions and the matrix $\mathbf{Z}_f$ are the far interactions.

In order to use the ACA, we first create a hierarchical data structure of the mesh using an octree as described in section 3.2. We then find at every level for each box containing elements their near neighbors and their far interacting groups. With the near neighbors at the finest level L we compute $\mathbf{Z}_n$ by direct evaluation with equation (3.9). In an octree, the maximum number of near neighbors of a box is constant. Hence, the total number of near interactions is $O(N)$. The matrix $\mathbf{Z}_f$ is computed with the far interacting couples of each box at every level. These interactions yield low-rank matrices that compound the far

interaction matrix as

$$\mathbf{Z}^f(a_i, b_i) = \mathbf{U}(a_i, b_i)\mathbf{V}^T(a_i, b_i) \tag{3.11}$$

where a_i and b_i are the far interacting boxes at level i. These low-rank matrices are computed using the method described in 3.3. There is a constant number of far interacting groups for each box, meaning that the number of far interactions at each level is $O(N)$. Therefore, the overall complexity is $O(NL) = O(N\log(N))$.

The compressed matrix $\tilde{\mathbf{Z}}$ yields fast MVP. Taking a vector $\mathbf{x}$ of dimension N we have the multiplication

$$\begin{aligned} \tilde{\mathbf{y}} &= \tilde{\mathbf{Z}}\mathbf{x} \\ \tilde{\mathbf{y}} &= \mathbf{Z}_n\mathbf{x} + \mathbf{Z}_f\mathbf{x} \\ \tilde{\mathbf{y}} &= \tilde{\mathbf{y}}^n + \tilde{\mathbf{y}}^f \end{aligned} \tag{3.12}$$

where $\tilde{\mathbf{y}}^n$ is obtained with a classical MVP whose cost is proportional to the number of elements, i.e. $O(N)$. The other part of the equation (3.12) is performed by multiplying the low-rank submatrices at every level by the correct subvector $\mathbf{x}$ and adding this to the correct positions in $\tilde{\mathbf{y}}^f$ as

$$\tilde{\mathbf{y}}^f(a_i) = \tilde{\mathbf{y}}^f(a_i) + \mathbf{Z}^f(a_i, b_i)\mathbf{x}(b_i) \tag{3.13}$$

The multiplication of $\mathbf{x}$ with all the interacting couples of $\mathbf{Z}^f$ has a cost of $O(N\log(N))$. Overall, the MVP (3.12) has $O(N\log(N))$ complexity.

3.5 Acceleration of the Symmetric and Calderon-Symmetric formulations

In this section we describe the implementation of the ACA fast solver for the symmetric formulation of the EEG forward problem as well as the preconditioned symmetric version, the Calderon-Symmetric formulation presented in Chapter 2. The nature of the integral kernel of the operators used in these formulations allows us to use the ACA efficiently.

3.5.1 Symmetric formulation

The integral symmetric formulation of the EEG forward problem is made of 4 operators yielding a block operator. The matrix form of the operator for a 3-surface head model reads

$$Z = \begin{bmatrix} (\sigma_1+\sigma_2)N_{11} & -\sigma_2 N_{12} & 0 & -2D^*_{11} & D^*_{12} \\ -\sigma_2 N_{21} & (\sigma_2+\sigma_3)N_{22} & -\sigma_3 N_{23} & D^*_{21} & -2D^*_{22} \\ 0 & -\sigma_3 N_{32} & \sigma_3 N_{33} & 0 & D^*_{32} \\ -2D_{11} & D_{12} & 0 & (\sigma_1^{-1}+\sigma_2^{-1})S_{11} & -\sigma_2^{-1}S_{12} \\ D_{21} & -2D_{22} & D_{23} & -\sigma_2^{-1}S_{21} & (\sigma_2^{-1}+\sigma_3^{-1})S_{22} \end{bmatrix} \tag{3.14}$$

where the operators N, S, D and D^* are defined in the chapter 2. The kernel of these operators is the 3D-static Green function, which is a smooth kernel. It is therefore possible and efficient to use the ACA method to compute the matrix Z.

Since the structure is composed of three surfaces, we must identify within the octree the elements belonging to different surfaces. With this data structure, each block of the operator Z is computed separately with the method presented in section 3.4 getting the compressed matrix

$$\tilde{\mathbf{Z}} = \begin{bmatrix} (\sigma_1+\sigma_2)\tilde{\mathbf{N}}_{11} & -\sigma_2\tilde{\mathbf{N}}_{12} & 0 & -2\tilde{\mathbf{D}}^*_{11} & \tilde{\mathbf{D}}^*_{12} \\ -\sigma_2\tilde{\mathbf{N}}_{21} & (\sigma_2+\sigma_3)\tilde{\mathbf{N}}_{22} & -\sigma_3\tilde{\mathbf{N}}_{23} & \tilde{\mathbf{D}}^*_{21} & -2\tilde{\mathbf{D}}^*_{22} \\ 0 & -\sigma_3\tilde{\mathbf{N}}_{32} & \sigma_3\tilde{\mathbf{N}}_{33} & 0 & \tilde{\mathbf{D}}^*_{32} \\ -2\tilde{\mathbf{D}}_{11} & \tilde{\mathbf{D}}_{12} & 0 & (\sigma_1^{-1}+\sigma_2^{-1})\tilde{\mathbf{S}}_{11} & -\sigma_2^{-1}\tilde{\mathbf{S}}_{12} \\ \tilde{\mathbf{D}}_{21} & -2\tilde{\mathbf{D}}_{22} & \tilde{\mathbf{D}}_{23} & -\sigma_2^{-1}\tilde{\mathbf{S}}_{21} & (\sigma_2^{-1}+\sigma_3^{-1})\tilde{\mathbf{S}}_{22} \end{bmatrix} \tag{3.15}$$

We then solve the system

$$\tilde{\mathbf{Z}}\mathbf{x} = \mathbf{b} \tag{3.16}$$

where $\mathbf{x}$ corresponds to the potentials and normal derivative of the potentials in the surfaces and $\mathbf{b}$ is the right hand side computed with a dipole source. The system is solved using an iterative solver, in our case we use the conjugate gradient square (CGS). Inside of the CGS we must perform the MVP $\tilde{\mathbf{Z}}\mathbf{x}_j$, where $\mathbf{x}_j$ is the approximate solution at the jth iteration of the iterative solver. This multiplication is performed by splitting the vector $\mathbf{x}_j$ and multiplying by the correct operator using the process described in the section 3.4. The parallelization of the overall process is straightforward with this approach.

3.5.2 Calderon-Symmetric formulation

The implementation of the Calderon preconditioner follows the same procedure as before with the difference that we use dual basis functions to discretize the operators. Luckily, these basis functions can be obtained using the same data structure and a local barycentric refinement when necessary. We compute each block of the operator C with the ACA getting the compressed matrix

$$\tilde{\mathbf{C}} = \begin{bmatrix} (\sigma_1+\sigma_2)\tilde{\mathbb{S}}_{11} & -\sigma_2\tilde{\mathbb{S}}_{12} & 0 & -2\tilde{\mathbb{D}}_{11} & \tilde{\mathbb{D}}_{12} \\ -\sigma_2\tilde{\mathbb{S}}_{21} & (\sigma_2+\sigma_3)\tilde{\mathbb{S}}_{22} & -\sigma_3\tilde{\mathbb{S}}_{23} & \tilde{\mathbb{D}}_{21} & -2\tilde{\mathbb{D}}_{22} \\ 0 & -\sigma_3\tilde{\mathbb{S}}_{32} & \sigma_3\tilde{\mathbb{S}}_{33} & 0 & \tilde{\mathbb{D}}_{32} \\ -2\tilde{\mathbb{D}}^*_{11} & \tilde{\mathbb{D}}^*_{12} & 0 & (\sigma_1^{-1}+\sigma_2^{-1})\tilde{\mathbb{N}}_{11} & -\sigma_2^{-1}\tilde{\mathbb{N}}_{12} \\ \tilde{\mathbb{D}}^*_{21} & -2\tilde{\mathbb{D}}^*_{22} & \tilde{\mathbb{D}}^*_{23} & -\sigma_2^{-1}\tilde{\mathbb{N}}_{21} & (\sigma_2^{-1}+\sigma_3^{-1})\tilde{\mathbb{N}}_{22} \end{bmatrix} \tag{3.17}$$

where the double barred notation is used to indicate that the operators have been discretized with dual basis and testing functions. The regularization matrix $\mathbf{Q}$ presented in Chapter 2 can be included with the constants multiplying each block operator in $\tilde{\mathbf{Z}}$ and $\tilde{\mathbf{C}}$

$$\begin{aligned} \tilde{\mathbf{Z}}_Q &= \mathbf{Q}\tilde{\mathbf{Z}}\mathbf{Q} \\ \tilde{\mathbf{C}}_Q &= \mathbf{Q}\tilde{\mathbf{C}}\mathbf{Q}. \end{aligned} \tag{3.18}$$

The Gram matrix necessary for the multiplication of $\tilde{\mathbf{Z}}_Q$ and $\tilde{\mathbf{C}}_Q$ is computed in the standard way. Applying the preconditioner to the symmetric matrix as described in Chapter 2, the new system to solve reads

$$\tilde{\mathbf{C}}_Q\mathbf{G}^{-1}\tilde{\mathbf{Z}}_Q\mathbf{x}' = \tilde{\mathbf{C}}_Q\mathbf{G}^{-1}\mathbf{Q}\mathbf{b}, \tag{3.19}$$

where $\tilde{\mathbf{C}}_Q\mathbf{G}^{-1}\tilde{\mathbf{Z}}_Q$ is the compressed Calderon-Symmetric matrix. The system is solved with an iterative solver, where a high acceleration is expected thanks to the fast MVP provided by the hierarchical multilevel compression and the fast convergence obtained when the preconditioner is applied. The multiplications within the iterative solver are performed

in three steps as follows

$$\mathbf{y}_1 = \tilde{\mathbf{Z}}_Q \mathbf{x}'_j \tag{3.20a}$$

$$\mathbf{y}_2 = \mathbf{G}^{-1}\mathbf{y}_1 \tag{3.20b}$$

$$\mathbf{y}_3 = \tilde{\mathbf{C}}_Q \mathbf{y}_2. \tag{3.20c}$$

The multiplications (3.20a) and (3.20c) are performed as explained in 3.5.1. In the case of (3.20b), even if the inversion of $\mathbf{G}^{-1}$ can be computed with low cost thanks to the sparsity of the Gram matrix, this results in a dense matrix. Hence, it is not efficient to get $\mathbf{y}_2$ directly. Instead, the equation (3.20b) can be rewritten as

$$\mathbf{G}\mathbf{y}_2 = \mathbf{y}_1, \tag{3.21}$$

and $\mathbf{y}_2$ is computed indirectly solving the equation (3.21) with an iterative solver. Since the Gram matrix is sparse, this can be done at very low cost.

3.5.3 Results

In the first set of tests we use a spherical head model with 3 concentric spheres of radii 0.8, 0.9, and 1.0 and with conductivities of 1.0, 0.0125 and 1.0. We started by checking the theoretical complexity of the ACA. In table 3.1 is shown a comparison in memory storage and MVP time of the dense and the compressed symmetric matrices. It can be seen that, for both memory and MVP, the compressed matrix operator scales with $O(N\log(N))$ while the dense matrix operator scales with $O(N^2)$ as expected from the theory.

	MVP time (s)		Memory (GB)	
n	Dense	ACA	Dense	ACA
7430	0.024	0.017	0.411	0.202
13608	0.073	0.033	1.380	0.397
24921	0.236	0.078	4.627	0.832
47790	0.787	0.100	17.016	2.081

Table 3.1: Memory and time results with a 3 surface spherical head model.

We then tested the impact of the Calderon preconditioner on the iterative solution time to solve the problem as well as on the time to compute the operator. In Figure 3.4 is presented the time to compute the compressed Calderon-Symmetric matrix and the symmetric matrix, in both dense and compressed cases. It can be verified that the compressed matrices scale with $O(N\log(N))$. The cost of computing the Calderon preconditioner is worth for high density meshes, where the iterative solver of the non-preconditioned systems has a low convergence and where direct inversion becomes impractical. This is confirmed in figure 3.5 where the computation time for the solution of the system is presented. It is clear that the direct inversion time increases with a cubic order, while the time for indirect solutions depends on, for both the symmetric and the Calderon-Symmetric formulations, the number of iterations of the CGS. However, the Calderon preconditioned formulation has the advantage that its number of iterations is constant. As a consequence, the iterative solver solution scales with the scaling of the MVP that is $O(N\log(N))$.

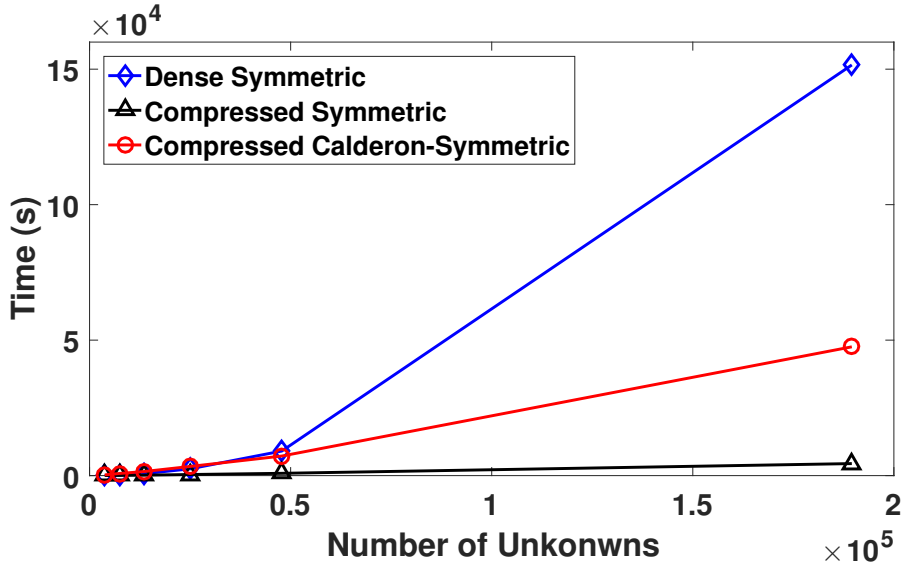

Figure 3.4: Computational time of the operators.

Finally, we seek to assess the performance of the Calderon preconditioner when used with the ACA in a realistic scenario. This case consists in computing a lead-field matrix using a head model obtained from MRI data. This matrix, which provides the propagation

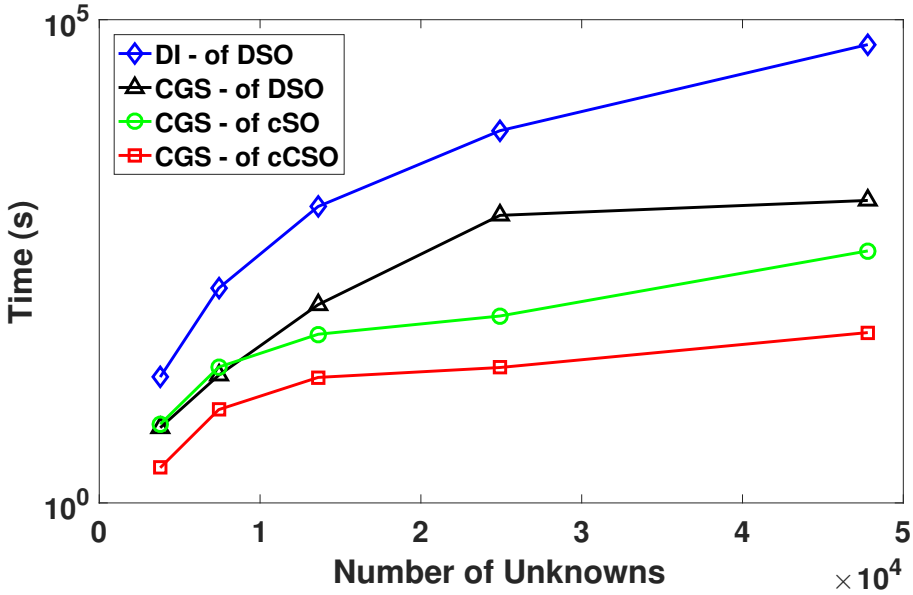

Figure 3.5: Solution time. Dense Symmetric(DS). Compressed Symmetric (CS). Compressed Calderon-Symmetric (CCS). Direct Inversion(DI).

model between known brain electric current sources and electrodes located at the surface of the head of a patient, is a key element in distributed inverse solutions [32]. For this purpose, we constructed a three layer mesh using [55]. These layers model the brain, the skull, and the scalp. They respectively contain 11850, 11616 and 22948 triangular cells. The potential generated on the scalp by a single dipole located in the brain is presented Figure 3.6a. This figure also shows the position of the 21 electrodes for which we computed the lead-field matrix. The error when the Calderon-Symmetric formulation is solved with the ACA compared with the original Symmetric formulation solved with direct inversion is displayed in Fig. 3.6b. It can be seen that the error is never greater than 0.05%. To fill-in the lead-field matrix, we placed 1500 unitary dipole sources in the brain layer, each having an orientation orthogonal to the brain surface. Using reciprocity as in [77], the forward model is then solved at each electrode position. We compared in Table 3.2, for four different cases, the time needed to compute the operator, the time needed to solve the forward system once, and the time needed to compute the full lead-field matrix. Hence, the total time needed

Method	Memory (GB)	Operator Time (s)	Solution Time (s)	Lead Field Time (h)
DI Dense Symmetric	16.234	10845.67	54609.99	18.19
CGS Dense Symmetric	16.234	10845.67	7294.61	45.56
CGS Compressed Symmetric	1.254	1436.63	2322.89	13.95
CGS Compressed Calderon-Symmetric	2.542	7888.86	62.40	2.56

Table 3.2: Memory and computation time information for computing a lead-field matrix using the reciprocity method

to get the lead-field matrix is given by the sum of the computation time for obtaining the operator and the time to get the solution for all the electrode positions. It can be seen that even if the time necessary to compute the compressed Calderon-Symmetric operator is greater than the time necessary to compute the compressed Symmetric operator, the fast convergence of the proposed method allows to compute the complete lead-field matrix in 2.56 hours, that is almost 10 times faster than without the proposed preconditioner. This compensates largely the computation overload brought by computing the preconditioning operator.

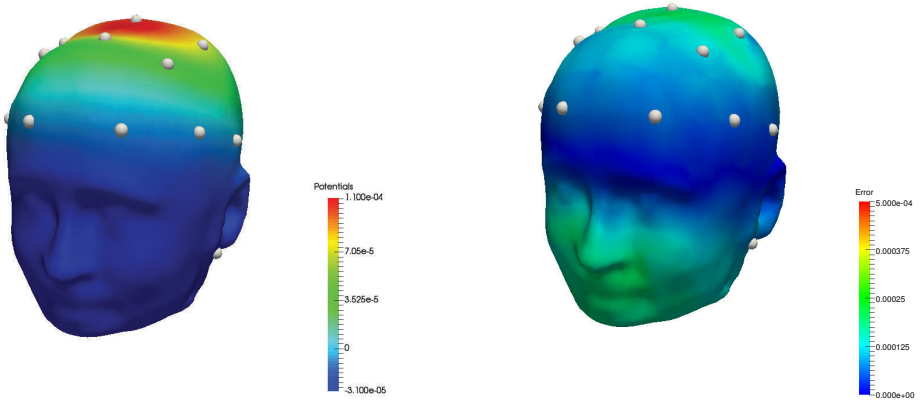

(a) Potential on the scalp produced for one dipole source for a 21 electrodes configuration

(b) Error of the compression compared with Dense matrix

Figure 3.6: MRI-obtained head model

3.6 Conclusion

In this chapter a fast solver for the Calderon-Symmetric formulation has been presented. This fast solver reduces the computational and MVP time as well as the storage memory, that decreases to $O(N\log(N))$ complexity. Numerical results proved the efficiency of the method in both spherical and real head models scenarios. Even if the implementation of the algorithm has been intended for the symmetric operator and the Calderon-Symmetric operator, it can be used for any block operator with an asymptotically smooth integral kernel.

Chapter 4

A hierarchical preconditioner for the PMCHWT integral equation

We present a hierarchical basis preconditioning strategy for the Poggio-Miller-Chang-Harrington-Wu-Tsai (PMCHWT) integral equation considering both simply and multiply connected geometries. To this end, we first consider the direct application of hierarchical basis preconditioners, developed for the Electric Field Integral Equation (EFIE), to the PMCHWT. It is notably found that, whereas for the EFIE a diagonal preconditioner can be used for obtaining the hierarchical basis scaling factors, this strategy is catastrophic in the case of the PMCHWT since it leads to a severely ill-conditioned PMCHWT system in the case of multiply connected geometries. We then proceed to a theoretical analysis of the effect of hierarchical bases on the PMCHWT operator for which we obtain the correct scaling factors and a provably effective preconditioner for both low frequencies and mesh refinements. Numerical results will corroborate the theory and show the effectiveness of our approach.

4.1 Introduction

In the frequency domain, the PMCHWT integral equation is used to solve scattering problems involving dielectric bodies. The PMCHWT operator comprises the EFIE operator and the MFIE operator and, thereby, it inherits some of the properties of these operators.

In particular, if the frequency f or the average edge length h of the mesh decreases, then the condition number of the system matrix of the discretized PMCHWT operator grows. These effects are often referred to as low-frequency and dense-discretization breakdown, respectively [6].

Classically, the low-frequency breakdown has been cured by using loop-tree or loop-star preconditioners [14]. More recently, a Calderón identity based preconditioner has been presented for curing also the dense-discretization breakdown [18, 79, 70]. This method, however, requires the use of dual elements defined on the barycentric refinement of the mesh. On the other hand, hierarchical basis preconditioners have been used in the past to cure the low-frequency and dense-discretization breakdown of the EFIE without using barycentric refinements [8, 13]. For this reason it would be useful to have a hierarchical basis strategy to precondition the PMCHWT, both in frequency and in discretization, without the need to go on the dual mesh. The extension of an EFIE hierarchical basis strategy to the PMCHWT, however, is not straightforward due to the fundamentally different way in which the two equations act on the global loops of the structure, the so called harmonic subspace.

The contribution of this section is twofold: (i) We present a theoretical analysis of the low-frequency properties of the PMCHWT operator at low frequencies for both simply and multiply connected geometries. The analysis will show why a direct extension of EFIE strategies would not work for the PMCHWT and will clarify both conditioning properties and solution scalings of the classical and preconditioned equation. (ii) We present a hierarchical basis preconditioning strategy that solves the low-frequency and the dense-discretization breakdown of the PMCHWT for both simply and multiply connected geometries.

For the sake of completeness the reader should notice that the conference contribution [24] reported numerical results of the application of a hierarchical basis to the PMCHWT.

Although the approach used by the authors of [24] remains undefined in their paper, their numerical experiments are limited to simply connected geometries (as for dielectrics) and thus they are not relevant for the theoretical findings presented here.

This chapter is organized as follows: Section 2 sets the notation and introduces background material, in Section 3 we derive our theory and propose a new preconditioner for the PMCHWT. Numerical results are presented and discussed in Section 4 that both corroborate the theory and show the practical applicability of the new scheme.

4.2 Notation and Background

We consider a polyhedral domain $\Omega_i \subset R^3$ with intrinsic impedance η_i and boundary $\Gamma = \partial\Omega_i$, which can be simply or multiply connected. The exterior domain $\Omega_o = \Omega_i^c \setminus \partial\Omega_i$ has the intrinsic impedance η_o. The EFIE operator reads

$$\mathcal{T}^\kappa = \mathrm{i}\kappa\mathcal{T}_\mathrm{A}^\kappa + 1/(\mathrm{i}\kappa)\mathcal{T}_\Phi^\kappa \tag{4.1}$$

with the vector potential $\mathcal{T}_\mathrm{A}^\kappa$ and the scalar potential $\mathcal{T}_\Phi^\kappa$ defined as

$$\begin{aligned}\mathcal{T}_\mathrm{A}^\kappa \boldsymbol{f} &= \hat{\boldsymbol{n}} \times \int_\Gamma G(\boldsymbol{r},\boldsymbol{r}')\boldsymbol{f}(\boldsymbol{r}')\mathrm{d}S(\boldsymbol{r}')\\ \mathcal{T}_\Phi^\kappa \boldsymbol{f} &= -\hat{\boldsymbol{n}} \times \nabla_\Gamma \int_\Gamma G(\boldsymbol{r},\boldsymbol{r}')\nabla'_\Gamma \cdot \boldsymbol{f}(\boldsymbol{r}')\mathrm{d}S(\boldsymbol{r}'),\end{aligned}$$

where $\hat{\boldsymbol{n}}$ is the outward going normal to the surface Γ, the wavenumber κ is k_i or k_o associated with the domain Ω_i or Ω_o, and where

$$G(\boldsymbol{r},\boldsymbol{r}') = \frac{\mathrm{e}^{\mathrm{i}\kappa|\boldsymbol{r}-\boldsymbol{r}'|}}{4\pi|\boldsymbol{r}-\boldsymbol{r}'|} \tag{4.2}$$

is the free-space Green's function. The MFIE operator reads

$$\mathcal{K}^\kappa \boldsymbol{f} = -\hat{\boldsymbol{n}} \times \int_\Gamma \nabla_\Gamma G(\boldsymbol{r},\boldsymbol{r}') \times \boldsymbol{f}(\boldsymbol{r}')\mathrm{d}S(\boldsymbol{r}'), \tag{4.3}$$

A time-harmonic electromagnetic wave $(\boldsymbol{E}^\mathrm{i}, \boldsymbol{H}^\mathrm{i})$ is impinging on Ω_i. Note that a time dependency $\mathrm{e}^{-\mathrm{i}\omega t}$ is suppressed throughout this section. The PMCHWT integral equation

reads

$$\begin{bmatrix} \mathcal{T}^{k_i}/\eta_i + \mathcal{T}^{k_o}/\eta_o & -(\mathcal{K}^{k_i} + \mathcal{K}^{k_o}) \\ (\mathcal{K}^{k_i} + \mathcal{K}^{k_o}) & \eta_i \mathcal{T}^{k_i} + \eta_o \mathcal{T}^{k_o} \end{bmatrix} \begin{bmatrix} \boldsymbol{M} \\ \boldsymbol{J} \end{bmatrix} = \begin{bmatrix} -\hat{\boldsymbol{n}} \times \boldsymbol{H}^{\mathrm{i}} \\ -\hat{\boldsymbol{n}} \times \boldsymbol{E}^{\mathrm{i}} \end{bmatrix},$$

for all $\boldsymbol{r} \in \Gamma$. It relates the magnetic and electric surface current densities $\boldsymbol{M}$ and $\boldsymbol{J}$, defined on Γ, to the incident fields.

To obtain $\boldsymbol{M}$ and $\boldsymbol{J}$, the surface Γ is triangulated and, via a Galerkin approach, the currents are approximated using the RWG functions $\boldsymbol{f}_n$ as source and the rotated RWGs $\hat{\boldsymbol{n}} \times \boldsymbol{f}_n$ are used as testing functions so that the currents are approximated as

$$\begin{aligned} \boldsymbol{M} &= \sum_{n=1}^{N} \left[\boldsymbol{m}\right]_n \boldsymbol{f}_n \\ \boldsymbol{J} &= \sum_{n=1}^{N} \left[\boldsymbol{j}\right]_n \boldsymbol{f}_n. \end{aligned} \tag{4.4}$$

The RWGs are normalized such that the flux through their defining edges equals 1. Thus, the linear system to solve reads

$$\boldsymbol{Z} \begin{bmatrix} \boldsymbol{m} \\ \boldsymbol{j} \end{bmatrix} := \begin{bmatrix} \boldsymbol{T}^{k_i}/\eta_i + \boldsymbol{T}^{k_o}/\eta_o & -(\boldsymbol{K}^{k_i} + \boldsymbol{K}^{k_o}) \\ \boldsymbol{K}^{k_i} + \boldsymbol{K}^{k_o} & \eta_i \boldsymbol{T}^{k_i} + \eta_o \boldsymbol{T}^{k_o} \end{bmatrix} \begin{bmatrix} \boldsymbol{m} \\ \boldsymbol{j} \end{bmatrix} = \begin{bmatrix} \boldsymbol{h} \\ \boldsymbol{e} \end{bmatrix}, \tag{4.5}$$

where the matrices are

$$\begin{aligned} \left[\boldsymbol{T}^{\kappa}\right]_{mn} &= (\hat{\boldsymbol{n}} \times \boldsymbol{f}_m, \mathcal{T}^{\kappa} \boldsymbol{f}_n)_{\boldsymbol{L}^2(\Gamma)} \\ \left[\boldsymbol{K}^{\kappa}\right]_{mn} &= (\hat{\boldsymbol{n}} \times \boldsymbol{f}_m, \mathcal{K}^{\kappa} \boldsymbol{f}_n)_{\boldsymbol{L}^2(\Gamma)} \end{aligned}$$

using the $\boldsymbol{L}^2(\Gamma)$-duality pairing. The right-hand side vectors are defined as

$$\begin{aligned} \left[\boldsymbol{h}\right]_m &= (\hat{\boldsymbol{n}} \times \boldsymbol{f}_m, -\hat{\boldsymbol{n}} \times \boldsymbol{H}^{\mathrm{i}})_{\boldsymbol{L}^2(\Gamma)} \\ \left[\boldsymbol{e}\right]_m &= (\hat{\boldsymbol{n}} \times \boldsymbol{f}_m, -\hat{\boldsymbol{n}} \times \boldsymbol{E}^{\mathrm{i}}(\boldsymbol{r}))_{\boldsymbol{L}^2(\Gamma)}. \end{aligned}$$

Any hierarchical basis $\boldsymbol{H}_n$ for the EFIE is a quasi-Helmholtz decomposition consisting of solenoidal $\boldsymbol{H}_n^{\Lambda}$, non-solenoidal $\boldsymbol{H}_n^{\Sigma}$, and quasi-harmonic functions $\boldsymbol{H}_n^{\mathrm{qH}}$. These functions are defined as linear combinations of RWG functions and we have

$$\boldsymbol{J} \approx \sum_{n=1}^{N} \left[\boldsymbol{j}\right]_n \boldsymbol{f}_n = \sum_{n=1}^{N_{\Lambda}} \left[\boldsymbol{j}_{\Lambda}\right]_n \boldsymbol{H}_n^{\Lambda} + \sum_{n=1}^{N_{\mathrm{qH}}} \left[\boldsymbol{j}_{\mathrm{qH}}\right]_n \boldsymbol{H}_n^{\mathrm{qH}} + \sum_{n=1}^{N_{\Sigma}} \left[\boldsymbol{j}_{\Sigma}\right]_n \boldsymbol{H}_n^{\Sigma}. \tag{4.6}$$

The reader should recall that the quasi-harmonic functions $\boldsymbol{H}_n^{\mathrm{qH}}$ are related to the global cycles of the structure, that is, they are present only when Γ is multiply connected to represent the quasi-harmonic Helmholtz subspace [73]. In fact, only when the global loops are added, we have $N = N_\Lambda + N_{\mathrm{qH}} + N_\Sigma$ with $N_{\mathrm{qH}} = 2g$, where g is the genus of the geometry. Since the functions $\boldsymbol{H}_n^{\Lambda}$, $\boldsymbol{H}_n^{\mathrm{qH}}$, and $\boldsymbol{H}_n^{\Sigma}$ are defined as linear combinations of RWG functions, we can define transformation matrices $\boldsymbol{H}_\Lambda$, $\boldsymbol{H}_{\mathrm{qH}}$, and $\boldsymbol{H}_\Sigma$ such that $\boldsymbol{j} = \boldsymbol{H}_\Lambda \boldsymbol{j}_\Lambda + \boldsymbol{H}_{\mathrm{qH}} \boldsymbol{j}_{\mathrm{qH}} + \boldsymbol{H}_\Sigma \boldsymbol{j}_\Sigma$. The analysis of this work applies to any hierarchical basis which can precondition the EFIE, that is, it yields a condition number that grows at most $O(\log(1/h)^2)$. In this work, we use the matrices $\boldsymbol{H}_\Lambda$, $\boldsymbol{H}_{\mathrm{qH}}$, and $\boldsymbol{H}_\Sigma$ obtained from the hierarchical basis defined in [8], for which after defining the diagonal matrices $\left[\boldsymbol{D}_{\hat{\boldsymbol{H}}^\Lambda}\right]_{nn} = 2^{l_{\hat{\boldsymbol{H}}^\Lambda}(n)/2}$, $\left[\boldsymbol{D}_{\hat{\boldsymbol{\Sigma}}}\right]_{nn} = 2^{-l_{\hat{\boldsymbol{\Sigma}}}(n)/2}$ (where the function $l_{\hat{\boldsymbol{H}}^\Lambda}(n)$, $n \in \{0 \ldots, N_\Lambda\}$, returns the level on which $\boldsymbol{H}_n^\Lambda$ is defined), and $\boldsymbol{M}_k = \left[\boldsymbol{H}_\Lambda \boldsymbol{D}_{\hat{\boldsymbol{H}}^\Lambda}/\sqrt{k} \quad \boldsymbol{H}_{\mathrm{qH}}/\sqrt{k} \quad \boldsymbol{H}_\Sigma \boldsymbol{D}_{\hat{\boldsymbol{\Sigma}}}\sqrt{k}\right]$, we have the conditioning property

$$\mathrm{cond}(\boldsymbol{M}_k^{\mathrm{T}} \boldsymbol{T}^k \boldsymbol{M}_k) \lesssim \log^2(1/h^2)\,. \tag{4.7}$$

In other words, for any hierarchical basis preconditioner for the EFIE satisfying condition (4.7), the theoretical developments obtained in this work will hold.

4.3 Hierarchical Preconditioners for the PMCHWT

The diagonal blocks of the PMCHWT operator contain the EFIE operator. The most intuitive idea for preconditioning the PMCHWT would then be to use the same EFIE strategy: perform the same change of basis for both electric and magnetic currents (as delineated in the previous section) and then proceed with a diagonal preconditioning. This idea would surely render well-conditioned diagonal blocks of the PMCHWT operator. Unfortunately, however, such a strategy would have catastrophic effects due to the off-diagonal blocks of the PMCHWT operator as will be shown next.

To see and solve this problem, we will perform a complete frequency analysis of the PMCHWT operator and associated solutions. To this purpose, we will use the hierarchical basis transformation without rescaling $\boldsymbol{M} = [\mathrm{diag}(\boldsymbol{M}_1, \boldsymbol{M}_1)]$ with $\boldsymbol{M}_1 = \begin{bmatrix} \boldsymbol{H}_\Lambda & \boldsymbol{H}_{\mathrm{qH}} & \boldsymbol{H}_\Sigma \end{bmatrix}$. This is possible since a hierarchical basis is in particular also a quasi-Helmholtz decomposition.

In order to proceed, we need to use the frequency analysis in [14] and extend it to the case of non-simply connected geometries. In [14], in fact, it is observed that the magnetostatic field produced by a loop is curl-free. This implies that the discretization of the $\mathcal{K}^k$ operator scales as $O(k^2)$ whenever the source is solenoidal (a local or a global loop) and the testing is a local loop, or the source is a local loop and the testing is solenoidal (a local or a global loop). For a further explanation the reader is referred to [14]. From this it follows that the hierarchical matrix blocks $\boldsymbol{H}_\Lambda^{\mathrm{T}} \boldsymbol{K}^k \boldsymbol{H}_\Lambda$, $\boldsymbol{H}_\Lambda^{\mathrm{T}} \boldsymbol{K}^k \boldsymbol{H}_{\mathrm{qH}}$, and $\boldsymbol{H}_{\mathrm{qH}}^{\mathrm{T}} \boldsymbol{K}^k \boldsymbol{H}_\Lambda$ will scale as $O(k^2)$. It remains to be studied the case in which both source and testing functions are global loops (i.e., they belongs to the quasi-harmonic subspace). We prove here the following result that will be used both here and in the h-conditioning analysis that will follow:

Proposition 4.1. *The matrix block $\boldsymbol{H}_{\mathrm{qH}}^{\mathrm{T}} \boldsymbol{K}^k \boldsymbol{H}_{\mathrm{qH}}$ scales as $O(1)$ with respect to k and has a conditioning which is both frequency and h independent.*

Proof. First it should be remembered that the harmonic Helmholtz subspace $H = \mathrm{span}\{\boldsymbol{h}_i\}$ is spanned by two g-dimensional, orthogonal subspaces, the poloidal and the toroidal loops [17]. Since these two subspaces are in the null-spaces of the operators $\pm\mathcal{I}/2 - \mathcal{K}^0$, respectively, [17], we have $\mathcal{K}^0 = \mathcal{I}/2$ for toroidal loops and $\mathcal{K}^0 = -\mathcal{I}/2$ for poloidal loops, where $\mathcal{I}$ is the identity operator. If the RWG functions could span H exactly, the above property would immediately prove the hypothesis. However, the RWG functions cannot span H exactly, instead they provide functions that are solenoidal, but not necessarily harmonic. This is equivalent to saying that linear combinations of RWGs result in global

loops $\boldsymbol{H}_i^{\mathrm{qH}} = \boldsymbol{h}_i + \boldsymbol{s}_i$, with $\boldsymbol{s}_i$ a solenoidal and non-irrotational function (i.e., a local loop). However it should be noted that

$$(\hat{\boldsymbol{n}} \times \boldsymbol{h}_j, \boldsymbol{\mathcal{K}}^0 \boldsymbol{s}_i)_{\boldsymbol{L}^2} = (\hat{\boldsymbol{n}} \times \boldsymbol{s}_j, \boldsymbol{\mathcal{K}}^0 \boldsymbol{h}_i)_{\boldsymbol{L}^2} = (\hat{\boldsymbol{n}} \times \boldsymbol{s}_j, \boldsymbol{\mathcal{K}}^0 \boldsymbol{s}_i)_{\boldsymbol{L}^2} = 0\,,$$

so that

$$(\hat{\boldsymbol{n}} \times (\boldsymbol{h}_j + \boldsymbol{s}_j), \boldsymbol{\mathcal{K}}^0 (\boldsymbol{h}_i + \boldsymbol{s}_i))_{\boldsymbol{L}^2} = (\hat{\boldsymbol{n}} \times \boldsymbol{h}_j, \boldsymbol{\mathcal{K}}^0 \boldsymbol{h}_i)_{\boldsymbol{L}^2}$$

from which the proposition is proved. □

The above proposition completes the analysis of the off-diagonal blocks of the PMCHWT. The analysis of the diagonal blocks and of the right-hand side (plane wave-excitation) directly follows from the EFIE [5]. Altogether, the following scalings for the entire PMCHWT equation, valid for both simply and multiply connected geometries are obtained (note that for the sake of brevity we write k instead of $O(k)$) : $\boldsymbol{M}^{\mathrm{T}} \boldsymbol{Z} \boldsymbol{M} \left[\boldsymbol{M}^{-1} \left[\boldsymbol{j}; \boldsymbol{m}\right]\right] = \boldsymbol{M}^{\mathrm{T}} [\boldsymbol{h}; \boldsymbol{e}] =$

$$\begin{matrix} \boldsymbol{H}_\Lambda^{\mathrm{T}} \\ \boldsymbol{H}_{\mathrm{qH}}^{\mathrm{T}} \\ \boldsymbol{H}_\Sigma^{\mathrm{T}} \\ \boldsymbol{H}_\Lambda^{\mathrm{T}} \\ \boldsymbol{H}_{\mathrm{qH}}^{\mathrm{T}} \\ \boldsymbol{H}_\Sigma^{\mathrm{T}} \end{matrix} \Bigg\{ \underbrace{\begin{bmatrix} k & k & k & k^2 & k^2 & 1 \\ k & k & k & k^2 & 1 & 1 \\ k & k & k^{-1} & 1 & 1 & 1 \\ k^2 & k^2 & 1 & k & k & k \\ k^2 & 1 & 1 & k & k & k \\ 1 & 1 & 1 & k & k & k^{-1} \end{bmatrix}}_{\boldsymbol{H}_\Lambda \quad \boldsymbol{H}_{\mathrm{qH}} \quad \boldsymbol{H}_\Sigma \quad \boldsymbol{H}_\Lambda \quad \boldsymbol{H}_{\mathrm{qH}} \quad \boldsymbol{H}_\Sigma} \begin{bmatrix} 1 \\ k \\ k \\ 1 \\ k \\ k \end{bmatrix} \Bigg\} \begin{matrix} \boldsymbol{M}_1^{-1} \boldsymbol{j} \\ \\ \\ \boldsymbol{M}_1^{-1} \boldsymbol{m} \\ \\ \\ \end{matrix} = \begin{bmatrix} k \\ k \\ 1 \\ k \\ k \\ 1 \end{bmatrix} \Bigg\} \begin{matrix} \boldsymbol{M}_1^{\mathrm{T}} \boldsymbol{h} \\ \\ \\ \boldsymbol{M}_1^{\mathrm{T}} \boldsymbol{e} \\ \\ \\ \end{matrix} \tag{4.8}$$

where the scaling of the solution has been obtained after performing a block analysis based on the Sherman-Morrison formulas [39]. The scalings in equation (4.8) clearly show why the idea of using the same preconditioning strategy adopted for the EFIE would be catastrophic for the PMCHWT. In fact, a diagonal preconditioner, by definition, would render $O(1)$ the frequency scaling of elements (2,2) and (5,5), but as a consequence the off-diagonal blocks associated to the harmonic subspace (elements (2,5) and (5,2)) would scale as $O(1/k)$ resulting in a catastrophic growth of the condition number.

Given the analysis above, we propose a hierarchical preconditioned PMCHWT in the form of

$$\boldsymbol{L}^{\mathrm{T}}\boldsymbol{Z}\boldsymbol{R}\boldsymbol{y} = \boldsymbol{L}^{\mathrm{T}}[\boldsymbol{h};\boldsymbol{e}], \quad \text{with } \boldsymbol{j} = \boldsymbol{R}\boldsymbol{y}\,. \tag{4.9}$$

The (potentially different) left and right preconditioning matrices we propose are defined as

$$\boldsymbol{L} = [\mathrm{diag}(\boldsymbol{L}_k, \boldsymbol{L}_k)], \quad \boldsymbol{R} = [\mathrm{diag}(\boldsymbol{R}_k \boldsymbol{R}_k)] \tag{4.10}$$

and with

$$\begin{aligned}\boldsymbol{L}_k &= \left[\boldsymbol{H}_\Lambda \boldsymbol{D}_{\hat{\boldsymbol{H}}^\Lambda}/\sqrt{k} \quad \boldsymbol{H}_{\mathrm{qH}}\sqrt{\beta} \quad i\boldsymbol{H}_\Sigma \boldsymbol{D}_{\hat{\boldsymbol{\Sigma}}}\sqrt{k}\right]\\ \boldsymbol{R}_k &= \left[\boldsymbol{H}_\Lambda \boldsymbol{D}_{\hat{\boldsymbol{H}}^\Lambda}/\sqrt{k} \quad \boldsymbol{H}_{\mathrm{qH}}\sqrt{\alpha} \quad i\boldsymbol{H}_\Sigma \boldsymbol{D}_{\hat{\boldsymbol{\Sigma}}}\sqrt{k}\right].\end{aligned}$$

The imaginary scaling of the non-solenoidal functions homogenizes the sign of the overall operator in the static limit [7]. Moreover, since a special problem has been identified by the previous analysis in the scaling of the harmonic subspace, we will study the effect of different scalings via the constants α and β. With these definitions we obtain the following frequency scaling for the preconditioned equation:

$$\boldsymbol{L}^{\mathrm{T}}\boldsymbol{Z}\boldsymbol{R} = \begin{bmatrix} 1 & \sqrt{\alpha}\sqrt{k} & k & k & k\sqrt{k}\sqrt{\alpha} & 1 \\ \sqrt{\beta}\sqrt{k} & \sqrt{\alpha\beta}k & \sqrt{\beta}k\sqrt{k} & \sqrt{\beta}k\sqrt{k} & \sqrt{\alpha\beta} & \sqrt{\beta}\sqrt{k} \\ k & k\sqrt{k}\sqrt{\alpha} & 1 & 1 & \sqrt{k}\sqrt{\alpha} & k \\ k & k\sqrt{k}\sqrt{\alpha} & 1 & 1 & \sqrt{k}\sqrt{\alpha} & k \\ \sqrt{\beta}k\sqrt{k} & \sqrt{\alpha\beta} & \sqrt{\beta}\sqrt{k} & \sqrt{\beta}\sqrt{k} & \sqrt{\alpha\beta}k & \sqrt{\beta}k\sqrt{k} \\ 1 & \sqrt{k}\sqrt{\alpha} & k & k & k\sqrt{k}\sqrt{\alpha} & 1 \end{bmatrix} \tag{4.11}$$

while for the current and the right-hand-side the scalings are

$$\begin{aligned}\boldsymbol{R}^{-1}[\boldsymbol{j};\boldsymbol{m}]^{\mathrm{T}} &= \left[\sqrt{k} \quad k/\sqrt{\alpha} \quad \sqrt{k} \quad \sqrt{k} \quad k/\sqrt{\alpha} \quad \sqrt{k}\right]^{\mathrm{T}}\\ \boldsymbol{L}[\boldsymbol{h};\boldsymbol{e}]^{\mathrm{T}} &= \left[\sqrt{k} \quad k\sqrt{\beta} \quad \sqrt{k} \quad \sqrt{k} \quad k\sqrt{\beta} \quad \sqrt{k}\right]^{\mathrm{T}}.\end{aligned} \tag{4.12}$$

Several choices of α and β are possible, but the following constraints arise by the scalings above: (i) $\alpha = 1/\beta$ in order to avoid a frequency breakdown in the off-diagonal block (elements (2,5) and (5,2). (ii) α and β can grow at most as $O(1/k)$ to avoid breakdowns. Two notable choices of α and β arise from this analysis:(a) $\alpha = 1/\beta = k$ which provides

an homogeneous frequency scaling of $O(\sqrt{k})$ for both solution and right-hand-side and (b) $\alpha = \beta = 1$ which provides a symmetric frequency scaling in the preconditioned matrix. We opt here for (b) since in this case $\boldsymbol{L} = \boldsymbol{R}$, which reduces the preconditioning storage. The other choice, however, could be equally exploited.

From (4.11) with $\alpha = \beta = 1$, it follows immediately that $\text{cond}(\boldsymbol{L}^{\mathrm{T}}\boldsymbol{Z}\boldsymbol{R}) = O(1), k \to 0$. Moreover, the h-dependent conditioning of the preconditioned equation is also uniformly bounded up to logarithmic terms. In fact, the diagonal blocks have a bounded conditioning as it follows from the initial hypothesis (4.7). The off-diagonal blocks are instead compact when either source or testing space is different from the harmonic subspace. In the case in which both source and testing functions are in the harmonic subspace, the h-uniform conditioning is ensured by the structure in (4.11) and by Proposition 4.1. Summarizing, the preconditioned PMCHWT we proposed will have a bounded condition number both in frequency and in discretization. Although the theoretical analysis is rigorous only for smooth surfaces, numerical practice in hierarchical schemes has shown that these methods are robust even for non-uniformly meshed and non-smooth geometries.

4.4 Numerical Results

To verify the frequency performance of our new scheme, we compared our new formulation with a standard loop-star preconditioner and with a hierarchical scheme followed by a naive diagonal preconditioner. For this test, we used a structure with two global loops shown in Figure 4.1a with permittivity $\varepsilon_{\mathrm{r}} = 3$ and with a maximum diameter of 2.8 m. We used a plane wave excitation and the CGS method (other Krylov methods show a similar behavior). Figure 4.2 shows that the number of iterations needed by the CGS solver to obtain a relative residual of 10^{-6} is independent from the frequency for both Loop-Star and the formulation presented in this work. However, the new formulation needs fewer iterations as expected by the fact that loop-star/tree schemes have a derivative behavior [4]. It should

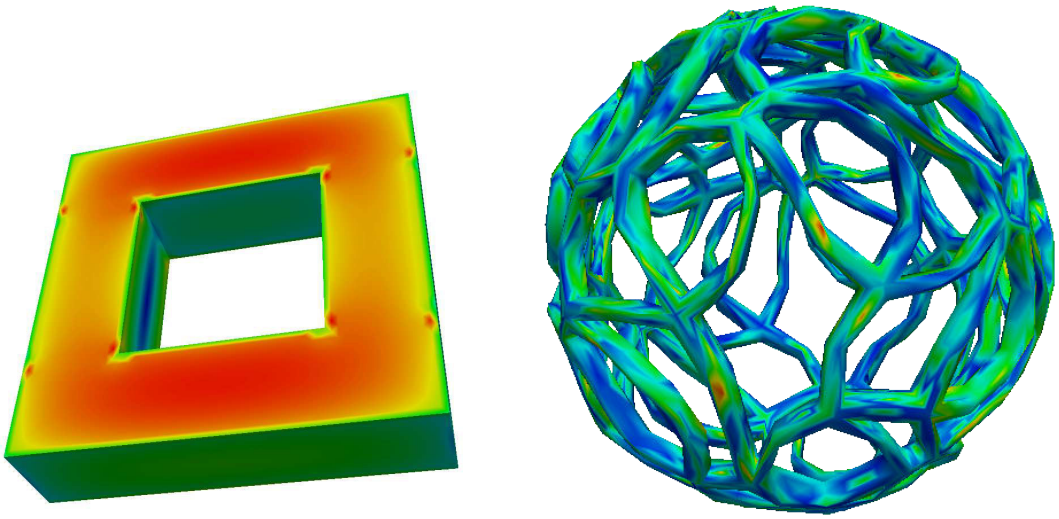

(a) Toroidal structure: $g = 1$ (b) 136 global loops ($g = 68$)

Figure 4.1: Test geometries with real part of the electric current density.

also be noted that a hierarchical scheme followed by a naive diagonal preconditioner does not deliver a frequency-independent number of iterations. This confirms the theory we have developed in the previous section. To verify the dense-discretization stability, we compared our new formulation again with a standard loop-star preconditioner and used a plane wave excitation with frequency 1 MHz. Figure 4.3 shows the number of iterations needed by the CGS solver to obtain a relative residual of 10^{-6}. We can see that the number of iterations needed by our new formulation is almost constant as predicted by theory while the derivative nature of the loop-star preconditioner results in a h-growing condition number. For h-refinement, naive diagonal preconditioning also yields a $O(\log(1/h)^2)$ conditioning which, however, deteriorates with respect to the new scheme by a constant depending on the frequency.

We also test the formulations in biological models, as the scalp and the skull shown in figures 4.4a and 4.4b respectively. We compare the convergence of the iterative solver of the new formulation with a standard loop-star preconditioner and with the naive hierarchical diagonal preconditioner using a tolerance of 1×10^{-5}, with frequency 1 MHz and 1 level of dyadic refinement. In the case of the head, due to the lack of harmonic subspace, the new

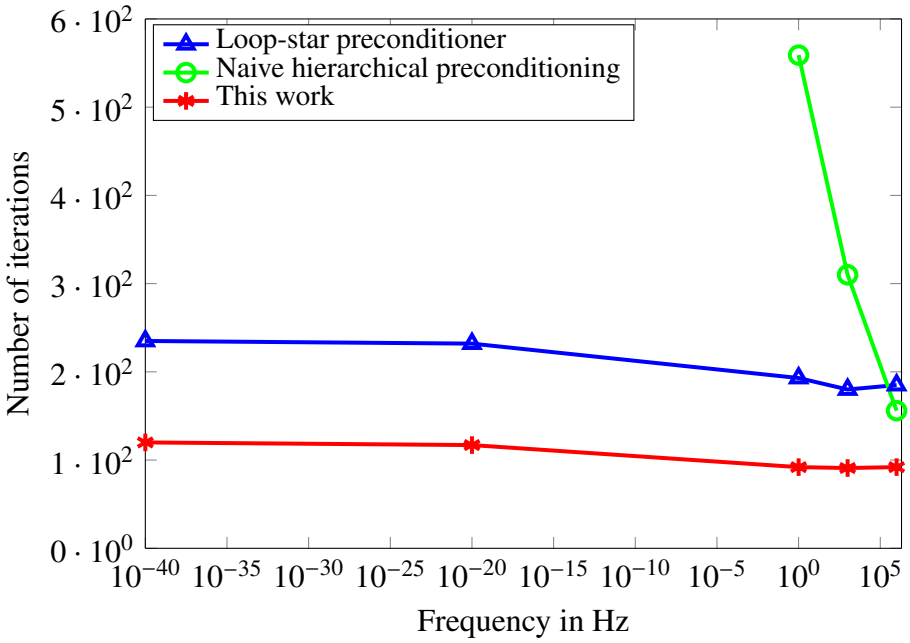

Figure 4.2: Toroidal structure: the number of iterations as a function of the frequency.

scheme and the naive diagonal preconditioner have the same convergence speed as is shown in figure 4.5. In figure 4.6 is presented the convergence for the skull model, which has 2 global loops. Here we can see the improvement in the convergence of the new formulations compared with both standard loop-star and naive hierarchical diagonal.

To verify the effectiveness of our approach in the presence of a larger harmonic subspace, we tested our new formulation on the multiply connected structure in Figure 4.1b containing 136 global loops and 2.7 m of diameter. A plane wave excitation is used with frequency 1 MHz. The results are shown in Table 4.1. Again there is a substantial advantage with respect to loop-star techniques even if only one dyadic refinement step was used as in this case. The stability on a harmonic subspace is thus also confirmed numerically.

Finally, to verify the accuracy, we compared the results obtained by our preconditioner with an analytic solution. Figure 4.7a and Figure 4.7b show a good agreement of the RCS for a sphere with radius 1 m and relative permittivity $\varepsilon_r = 3$ and plane wave excitation. In both cases the error is -22.6dB

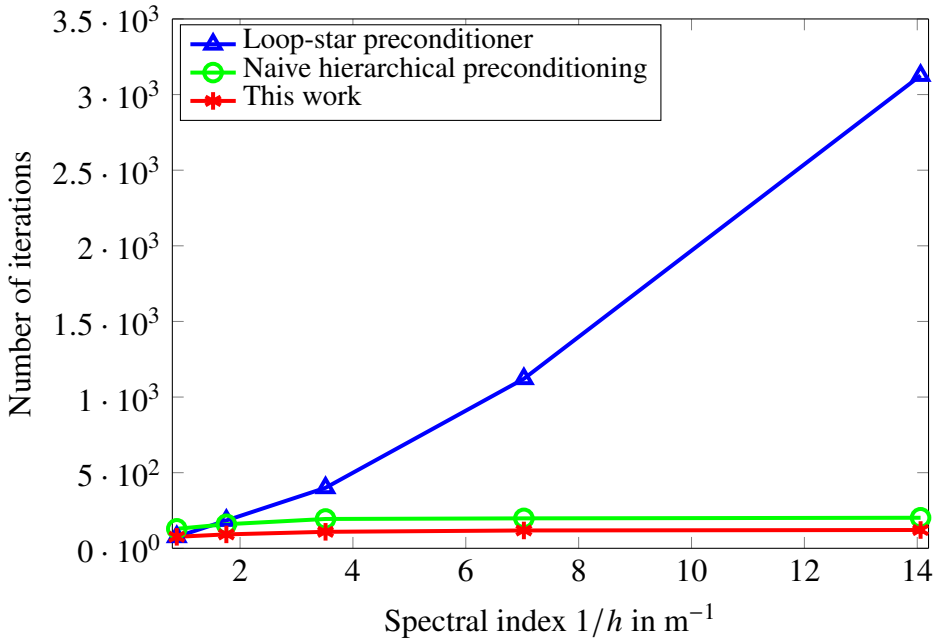

Figure 4.3: Toroidal structure: the number of iterations as a function of the spectral index $1/h$.

Formulation	Iterations	Time
Loop-star preconditioner	5396	52h 1'22"
Naive hierarchical preconditioning	18318	>>100h
This work	2642	21h 6'5"

Table 4.1: 136 global loops structure: the number of iterations for the different formulations with solver tolerance $10^{-}6$.

4.5 Conclusion

It has been presented a new hierarchical preconditioner for the PMCHWT that does not suffer of dense-discretization and low-frequency breakdown. The new formulation can handle simply and multiply connected geometries. The numerical results show improvement in the number of iterations for both a simple structure with just 2 global loops and with a complex structure with 136 global loops proving the effectiveness of the method.

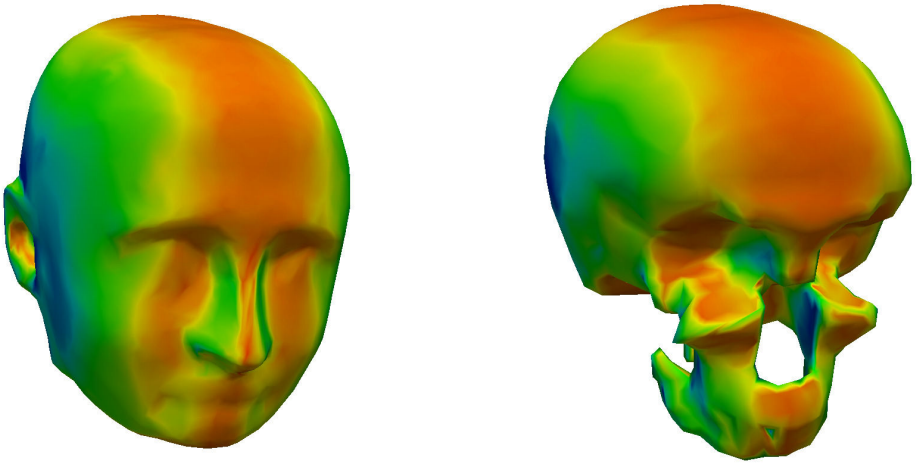

(a) Head model: $g = 0$ (b) Skull model : $g = 1$

Figure 4.4: Biological models with real part of the electric current density.

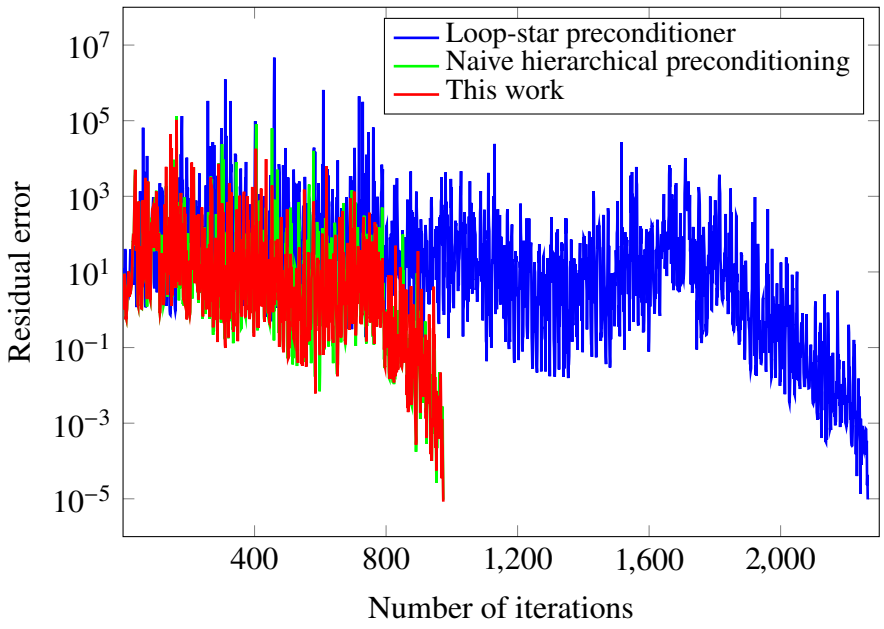

Figure 4.5: Head model: Residual error of the iterative solver.

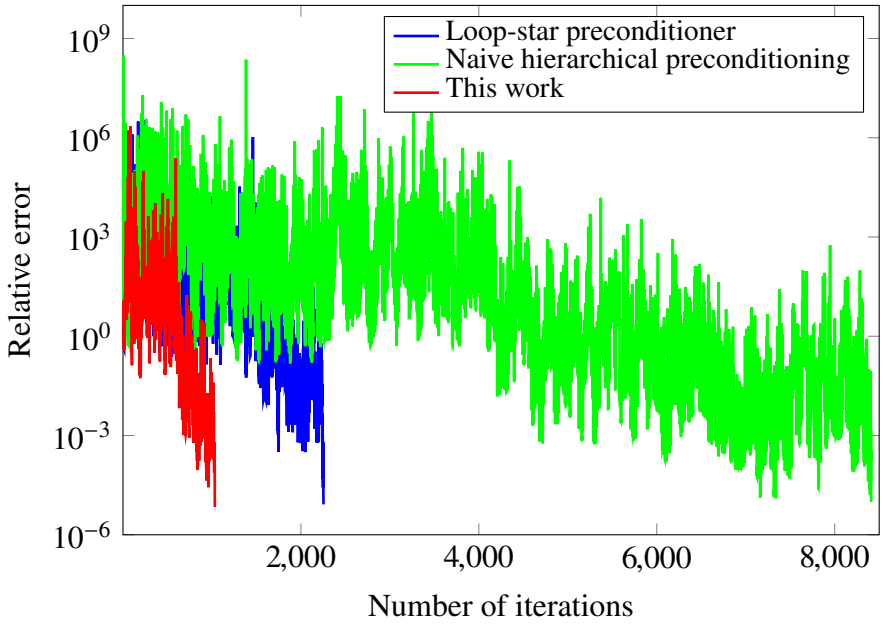

Figure 4.6: Skull model: Residual error of the iterative solver

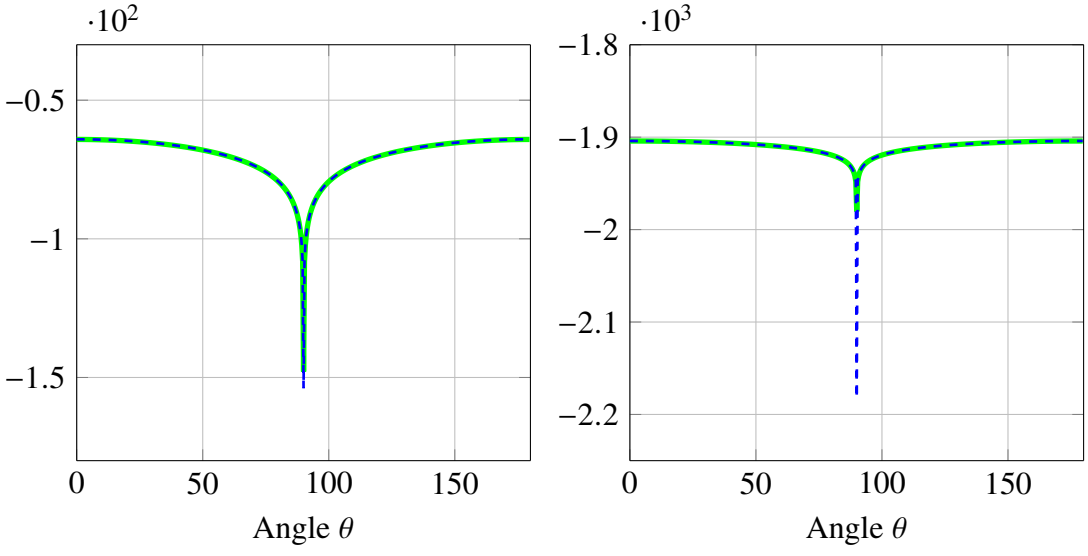

(a) Frequency: 1 MHz.

(b) Frequency: 1e-40 Hz.

Figure 4.7: Sphere: Radar cross section in dBsm.

Chapter 5

A new computational framework for 2D electromagnetic formulations

In this chapter is presented a propaedeutic discretization framework and associated computational library for 2D Calderon research which will enable future investigations in tomographic imaging. To this end, we first define the Electric Field Integral Equation (EFIE) in 2D for both polarizations, transverse magnetic (TM) and transverse electric (TE). We also present the different discretizations of the operators. We then provide a general description of the computational library. Finally, the second Calderon identity is used to build four preconditioners, which are validated with the library. Numerical results are presented to prove the theory.

5.1 Introduction

For infinite cylindrical or translationally invariant scatterers, the 3D-problem can be reduced to a 2D scalar problem. The 2D Electric Field Integral Equation (EFIE) is a well known formulation for scattering electromagnetic problems [41] and has been used in microwave imaging [25]. In two dimensions, the incident field can be split in transverse electric (TE) and transverse magnetic (TM), which results in two different formulations [37]. Both formulations have operators that are ill-conditioned with respect to dense discretization. In the case of 3D-EFIE, the Calderon identities have been used to cure the

mesh refinement ill-conditioning [6]. Indeed, by leveraging on the Calderon identities a multiplicative preconditioner can be built. This preconditioner strategy can be extended to the 2D-EFIE.

In this chapter we present a computational library for 2D electromagnetic problems, which provides all the necessary tools to compute the 2D-operators and is used to study the 2D-Calderon identities. In order to describe the library, we first review the EFIE with both TM and TE polarizations.

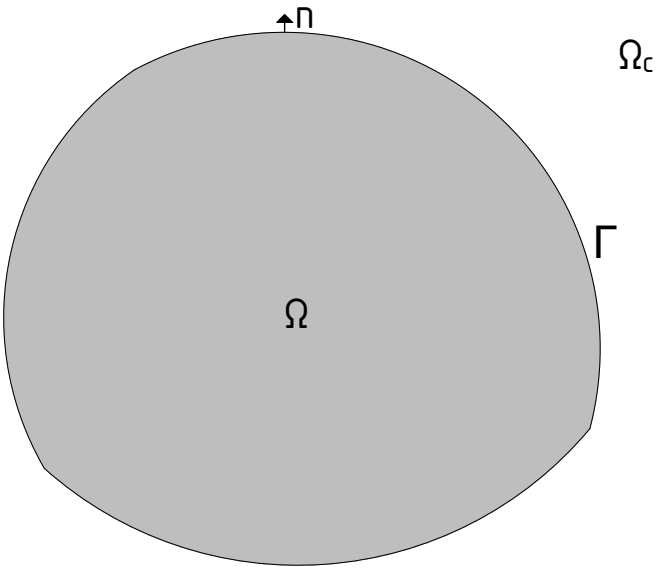

Figure 5.1: Cross section of a cylinder with the xy plane

5.1.1 TM polarization

We consider a conductive cylinder that extends to infinity along the z-axis. Therefore, we only have to analyze the cross section Ω, in the xy-plane. We define the boundary $\partial\Omega = \Gamma$ with an outward going normal $\mathbf{n}$ and an exterior domain $\Omega_c = R^3 \backslash \Omega$, as is shown in figure 5.1.

Let's consider an impinging electromagnetic wave with TM polarization, i.e, the electric field with only z direction component and the magnetic field with components only transverse to z. In this case, the surface current is in the z direction and the electric field integral equation (EFIE) reads

$$\frac{k_0\eta}{4}\int_\Gamma H_0^{(2)}(k_0|\boldsymbol{\rho}-\boldsymbol{\rho}'|)J_z(\boldsymbol{\rho}')d\boldsymbol{\rho}' = E_z^{inc}(\boldsymbol{\rho}) \tag{5.1}$$

where J_z is the surface current in z direction, η is the intrinsic impedance and $H_0^{(2)}$ is the zero order Hankel function. We define TM - electric field integral operator (TM-EFIO) as

$$(T^{TM}J_z)(\boldsymbol{\rho}) = \frac{k_0\eta}{4}\int_\Gamma H_0^{(2)}(k_0|\boldsymbol{\rho}-\boldsymbol{\rho}'|)J_z(\boldsymbol{\rho}')d\boldsymbol{\rho}' \tag{5.2}$$

This is a single layer operator in 2D, which is a compact operator. Therefore, it has a condition number that grows inversely proportional to the length refinement.

5.1.2 TE polarization

We consider the same PEC cylinder as before, with Ω, Γ as is shown in figure 5.1. In this case, an electromagnetic wave with TE polarization is impinging in the scatterer, i.e. the magnetic field only has a component in the z direction and the electric field is transverse to z. Therefore the surface current is tangential to the contour Γ. By using the Maxwell equations together with the boundary conditions we can find the TE-EFIE as

$$\begin{aligned}\frac{k_0\eta}{4}\hat{t}\cdot\int_C H_0^{(2)}(k_0|\boldsymbol{\rho}-\boldsymbol{\rho}'|)\hat{t}'J_t(\boldsymbol{\rho}')d\boldsymbol{\rho}' \\ + \frac{\eta}{4k_0}\hat{t}\cdot\nabla\int_C \nabla'\cdot[\hat{t}'J_t(\boldsymbol{\rho}')]H_0^{(2)}(k_0|\boldsymbol{\rho}-\boldsymbol{\rho}'|)d\boldsymbol{\rho}' = \hat{t}\cdot\mathbf{E}^{inc}(\boldsymbol{\rho})\end{aligned} \tag{5.3}$$

where J_t is the tangential component of the current, $\hat{t}$ is the tangential unit vector in $\boldsymbol{\rho}$ and $\mathbf{E}^{inc}(\boldsymbol{\rho})$ is the incident field. In this case, the incident field has only x and y components. We define the TE-EFIO as

$$(T^{TE} J_t)(\boldsymbol{\rho}) = \frac{k_0 \eta}{4} \hat{t} \cdot \int_C H_0^{(2)}(k_0 |\boldsymbol{\rho} - \boldsymbol{\rho}'|) \hat{t}' J_t(\boldsymbol{\rho}') d\boldsymbol{\rho}' + \frac{\eta}{4k_0} \hat{t} \cdot \nabla \int_C \nabla' \cdot [\hat{t}' J_t(\boldsymbol{\rho}')] H_0^{(2)}(k_0 |\boldsymbol{\rho} - \boldsymbol{\rho}'|) d\boldsymbol{\rho}' \quad (5.4)$$

This operator is compound with the sum of two operators, a single layer and a hypersingular, that is an unbounded operator. In other words, the T^{TE} operator is the sum of a compact operator and an unbounded operator, both with a condition number that grows inversely proportional to the length refinement. Hence, the T^{TE} operator has a condition number that grows with the same order as the T^{TM} operator.

5.2 Discretization

In order to solve (5.1) and (5.3) numerically, we divided the contour $\Gamma = \bigcup_{i=1} \Gamma_i$ into linear segments, which creates a standard mesh. Here, we can define the 2D piecewise constant functions $P^0(\rho)$ as is shown in figure 5.2. These pulse functions are defined in each segment s_n. We also define the 2D piecewise linear functions or triangle functions, which are defined in each vertex $\mathbf{v}_n$ as in figure 5.3.

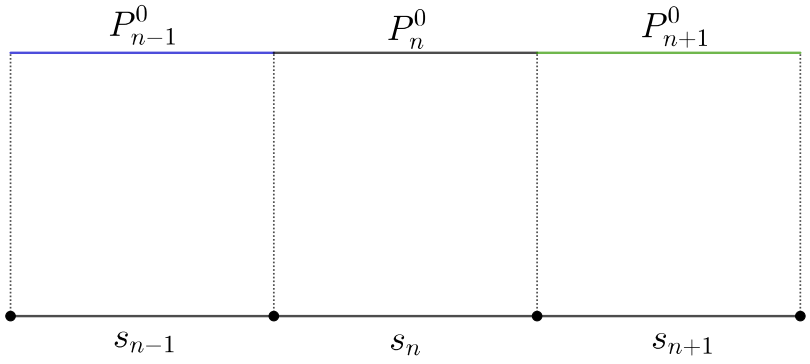

Figure 5.2: Piecewise constant functions

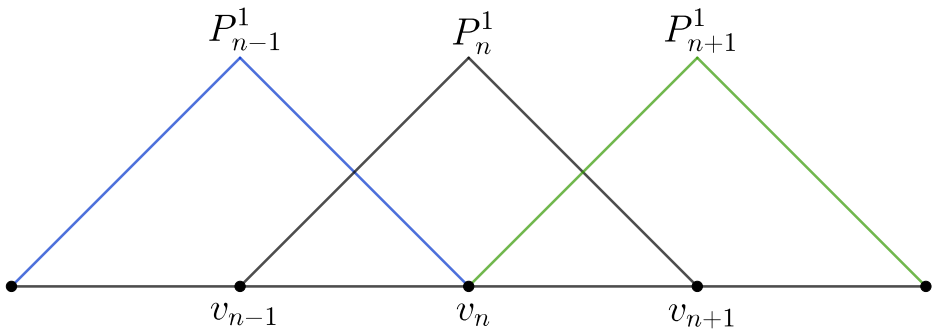

Figure 5.3: Piecewise linear functions

Moreover, we can construct dual functions which are built on the dual mesh. The dual mesh is created using the barycentric refinement, where the dual vertices are the barycenters of each standard segment. We then define the dual piecewise constant functions $\tilde{P}^0$, that are associated with a vertex of the standard mesh and they are a linear combination of the barycentric functions as is shown in figure 5.4. In a same manner, combining the barycentric triangle functions, we create the dual piecewise linear functions $\tilde{P}^1$, which are defined in each standard segment s_n. They are presented in figure 5.5.

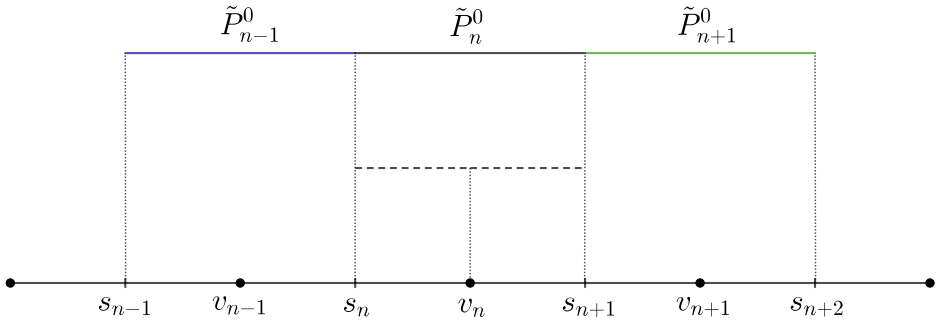

Figure 5.4: Dual piecewise constant functions

Now, by using the scalar product $\langle \cdot, \cdot \rangle$ defined as

$$\langle g, f \rangle = \int_\Gamma g(\boldsymbol{\rho}) f(\boldsymbol{\rho}) d\boldsymbol{\rho} \tag{5.5}$$

we can discretize the systems (5.1) and (5.3). For this, we expand the unknown surface

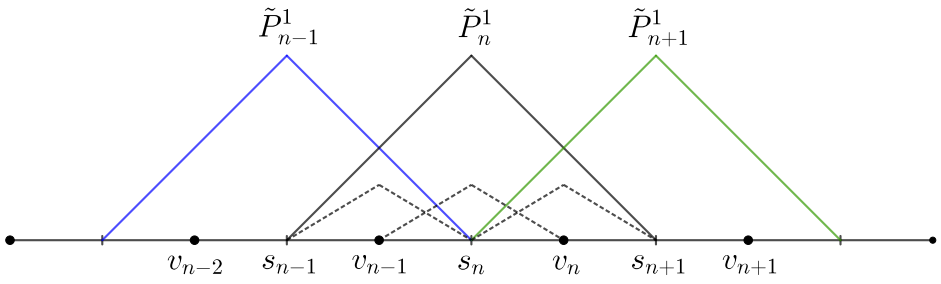

Figure 5.5: Dual piecewise linear functions

current as

$$J = \sum_{i}^{N} a_i f_i(\boldsymbol{\rho}) \tag{5.6}$$

where, a_i are the coefficients to find and f_i is a basis function that can be either P^0, $\tilde{P}^0$, P^1, $\tilde{P}^1$. We then use a testing function g_i, which can also be one of the four functions presented before. This results in the matrix equation

$$\mathbf{Ta} = \mathbf{b} \tag{5.7}$$

where $\mathbf{a}$ is the vector of unknown coefficients a_i, $\mathbf{b}$ is the right hand side vector, whose elements are $\mathbf{b}_i = \langle g_i, E^{inc} \rangle$, and $\mathbf{T}$ is the matrix operator with elements defined as $\mathbf{T}_{i,j} = \langle g_i, T f_j \rangle$. The operator T can be T^{TM} or T^{TE}.

The operator T^{TM} can be discretized using as basis and testing functions $P^0(\rho)$ or $P^1(\rho)$. Moreover, we discretize T^{TM} with the dual function $\tilde{P}^0$. This discretization is used in one of the preconditioner strategies later on. Hence, the discretized operators read

$$\mathbf{T}_0^{TM} = \langle P^0, T^{TM}(P^0) \rangle \tag{5.8a}$$

$$\mathbf{T}_1^{TM} = \langle P^1, T^{TM}(P^1) \rangle \tag{5.8b}$$

$$\tilde{\mathbf{T}}_0^{TM} = \langle \tilde{P}^0, T^{TM}(\tilde{P}^0) \rangle \tag{5.8c}$$

In the case of the T^{TE} operator, it is required basis functions of at least order one due to the presence of the hypersingular operator. Therefore, we discretize the operator with

triangle basis functions P^1. As before, we also discretize using the dual function $\tilde{P}^1$ to use it as preconditioner. Then, we get

$$\mathbf{T}_1^{TE} = \langle P^1, T^{TE}(P^1)\rangle \tag{5.9a}$$

$$\tilde{\mathbf{T}}_1^{TE} = \langle \tilde{P}^1, T^{TE}(\tilde{P}^1)\rangle \tag{5.9b}$$

In order to perform the matrix-matrix product, which will be used in the preconditioning, it is necessary to have a Gram matrix to link the discretization of the operators. Hence, we define the following Gram matrices

$$\mathbf{G}_{11} = \langle P^1, P^1\rangle \tag{5.10a}$$

$$\mathbf{G}_{0\tilde{1}} = \langle P^0, \tilde{P}^1\rangle \tag{5.10b}$$

$$\mathbf{G}_{1\tilde{0}} = \langle P^1, \tilde{P}^0\rangle \tag{5.10c}$$

5.3 Overview of the 2D-Library

A library for 2D electromagnetic problems has been implemented using Matlab ©. In table 5.1 are presented all the functions of the library. The first three functions of the table are used to create the data structure of the mesh, which is composed of points and segments, as well as the structure for the triangle functions both standard and dual. The following functions of the table create the matrices of the 2D-EFIE operators for both polarizations with different discretizations. These functions use Gaussian integration for the non-singular elements and singularity extraction for the singular ones. The library has functions to compute the matrix operators for the Magnetic Field Integral Equations (MFIE) [42] as well. We named the operator functions using the following format

`[Formulation]_[Polarization]_[Discretization Function].`

We then have the functions to compute the Gram matrices $\mathbf{G}_{11}$, $\mathbf{G}_{0\tilde{1}}$ and $\mathbf{G}_{1\tilde{0}}$. The next functions on the list compute the incident fields creating the right hand side (RHS) vector.

read_2D_mesh	MFIE_TM_dp1	PW_EFIE_TE_dp1
create_bar_mesh	MFIE_TE_p1	PW_EFIE_TE_p1
create_p1_functions	MFIE_TE_dp1	PW_MFIE_TM_p1
EFIE_TM_p0	Gmtrx_p1_p1	PW_MFIE_TM_dp1
EFIE_TM_p1	Gmtrx_p0_dp1	PW_MFIE_TE_p1
EFIE_TM_dp0	Gmtrx_p1_dp0	PW_MFIE_TE_dp1
EFIE_TM_dp1	PW_EFIE_TM_p0	p1_functions_value
EFIE_TE_p1	PW_EFIE_TM_dp0	quadrature_points
EFIE_TE_dp1	PW_EFIE_TM_p1	
MFIE_TM_p1	PW_EFIE_TM_dp1	

Table 5.1: List of functions

Here, we also implemented the RHS vector for the MFIE formulation. Up to now, we have implemented plane waves (PW) incident fields. The name of the functions for computing the incident field have the format

```
[Incident field]_[Formulation]_[Discretization Function].
```

The last two functions in the table 5.1 are used inside of the operator and RHS functions to compute the Gaussian integration.

This framework provides the tools necessary to construct and analyze 2D electromagnetic problems. In the following section we validate the application of the second Calderon identity for preconditioning the 2D-EFIE, where this library is used to compute the numerical results.

5.4 Calderon preconditioners

In this section we describe the second Calderon identity in 2D, which we use to build preconditioners for T^{TM} and T^{TE} operators. It is well known that using this identity the EFIE in 3D can be preconditioned [6]. We extend this to TM-EFIO and TE-EFIO.

The Calderon identities for the 3D EFIE read

$$TK = -KT \tag{5.11a}$$

$$T^2 = -\frac{1}{4}I + K^2 \tag{5.11b}$$

where I is the identity operator and K is a compact operator. The second identity shows that the EFIE preconditions itself. This is due to the presence of a single and hypersingular operator, which precondition each other. However, the absence of a hypersingular part in the TM-EFIO does not allow the self preconditioning. Instead, we can use the T^{TE} to precondition T^{TM} or vice versa. Hence, we have the next identities

$$T^{TE}T^{TM} = -\frac{1}{4}I + K^2 \tag{5.12a}$$

$$T^{TM}T^{TE} = -\frac{1}{4}I + K^2 \tag{5.12b}$$

In the case of T^{TM} operator, we have two possible discretizations, using pulse functions or triangle functions. When the P^0 are used, the T^{TE} operator acting as a left preconditioner has to be discretized with the dual triangle functions $\hat{P}^1$ in order to have functions based in the same elements. The Gram matrix (5.10a) is necessary to perform the matrix multiplication. With this, we get the preconditioned matrix operator

$$\tilde{\mathbf{T}}_C^{TM} = \tilde{\mathbf{T}}_1^{TE}\mathbf{G}_{0\tilde{1}}^{-1}\mathbf{T}_0^{TM} \tag{5.13}$$

On the other hand, when T^{TM} is discretized with P^1 functions, P^1 functions are used in the T^{TE} operator as well. In this case, we use the Gram matrix (5.10b) to link both discretizations. The preconditioned matrix operator reads

$$\mathbf{T}_C^{TM} = \mathbf{T}_1^{TE}\mathbf{G}_{11}^{-1}\mathbf{T}_1^{TM} \tag{5.14}$$

In the case of the T^{TE} operator, although there is only one possible discretization using P^1 functions, the T^{TM} operator used as left preconditioner can have two possible discretizations. This is due to the fact that the T^{TM} operator can use two functions based on the nodes,

the triangle and the dual pulse functions. Therefore, we have two preconditioners

$$\mathbf{T}_C^{TE} = \mathbf{T}_1^{TM}\mathbf{G}_{11}^{-1}\mathbf{T}_1^{TE} \tag{5.15a}$$

$$\tilde{\mathbf{T}}_C^{TE} = \tilde{\mathbf{T}}_0^{TM}\mathbf{G}_{1\tilde{0}}^{-1}\mathbf{T}_1^{TE} \tag{5.15b}$$

5.5 Numerical results

We test the preconditioned operators using an infinite cylinder in the z direction with radius 1. The wavelength is fixed to $\lambda = 2\pi/3$. The contour of the cross section is discretized with an uniform segment length h.

First, we compute the condition number of the operator T^{TM} with both P^0 and P^1 discretizations and we compare them with the condition number for the preconditioned versions. In figure 5.6 is presented the condition number with respect to the spectral index $1/h$. It is clear that $\mathbf{T}_0^{TM}$ and $\mathbf{T}_1^{TM}$ have an increasing condition number with $O(1/h)$, while the preconditioned operators present a constant condition number as was expected.

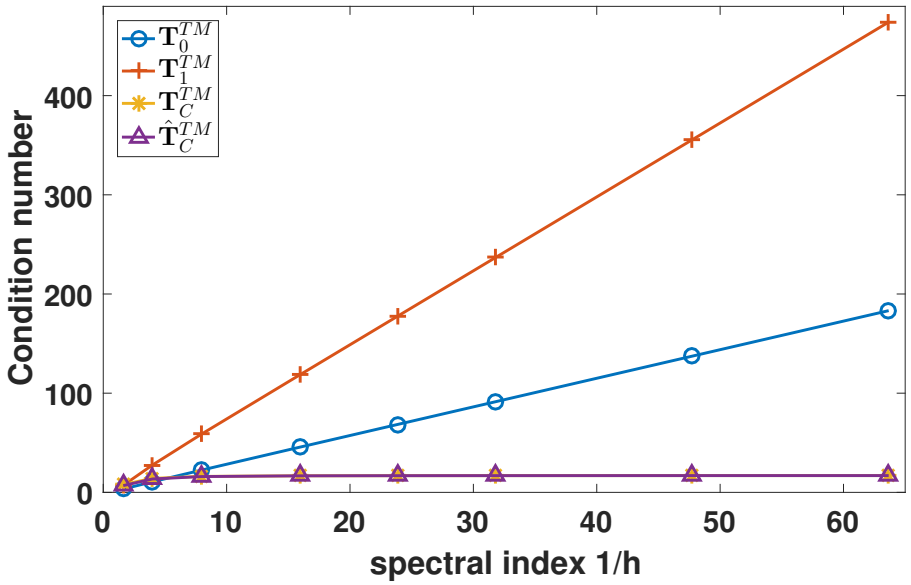

Figure 5.6: Condition number for TM operators when the mesh is refined

We follow the same procedure to test the operator T^{TE}. In figure 5.7 is shown the

condition number for different mesh refinements of the matrix operators $\mathbf{T}_1^{TE}$, $\mathbf{T}_C^{TE}$ and $\tilde{\mathbf{T}}_C^{TE}$. In this figure, it is shown that the ill-conditioned operator T^{TE} can be preconditioned using the T^{TM} operator with both discretizations.

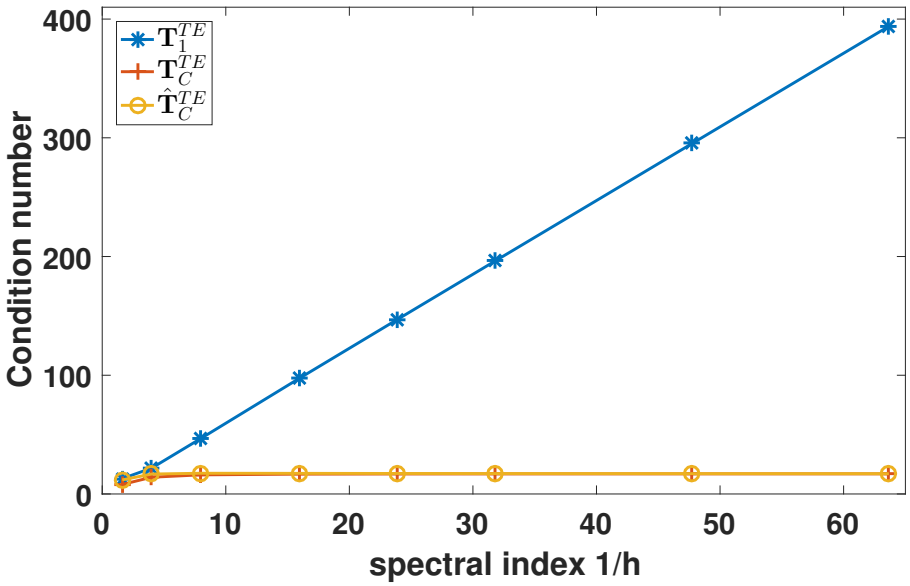

Figure 5.7: Condition number for TE operators when the mesh is refined

5.6 Conclusions

A new 2D library for electromagnetic formulations has been implemented, which will be the starting point for future research. The aim is to study the forward problem of the microwave tomography using the 2D-EFIE formulation. Using the new computational framework we have validated the Calderon preconditioning for the 2D-EFIE formulations. The numerical results show the correctness of this preconditioning strategies.

Chapter 6

Conclusion and Future Work

The work presented in this manuscript is the compendium of three years of investigation on new strategies to improve the boundary element formulations for electromagnetic problems. Two formulations were studied, the symmetric formulation for the EEG forward problem and the PMCHWT for penetrable objects.

In order to speed up the solution time for the symmetric formulation for high dense meshes, a new regularized symmetric formulation was presented, which solves both, high contrast conductivity and high mesh discretization, ill-conditioning problems. This new scheme was based on Calderon identities, which allow to build a preconditioner that, combined with the standard operator, results in a new second kind operator which is both stable and well-conditioned under all the above mentioned conditions. Thanks to the nature of the new strategy, the same computational technology required by the standard symmetric formulation can be used to compute the new preconditioner. To exploit the new regularized symmetric formulation, a fast solver was implemented. This fast solver is an adaptation of the ACA method for block operator matrices, which is based on a kernel free compression strategy.

In Chapter 4 was proved, theoretically and numerically, the effectiveness of hierarchical basis preconditioners to solve the ill-conditioning problems of the PMCHWT. A theoretical analysis of the effect of hierarchical bases on the PMCHWT operator was performed for

which the correct scaling factors and an effective preconditioner for both low frequencies and mesh refinements were obtained.

A propaedeutic discretization framework and associated computational library for 2D and the validation of the Calderon preconditioning for the 2D-EFIE were presented in Chapter 5. The results presented here prove the correct functioning of the Calderon identities in 2D .

The work presented in this manuscript settles the base for future investigations:

- First of all, the strategy used in Calderon-Symmetric formulation for nested domains can be extended to other formulations with similar features. In general, formulations for nested domains present the interaction of different interfaces, which yield an operator as the one of the symmetric formulation.

- Moreover, the ACA implementation presented in Chapter 3 can be extended to be used in any block operator with smooth kernels.

- The application of H2-matrices fast solver can also be studied for the symmetric formulation as well as fast direct solvers.

- The new fast method presented for the EEG forward problem can be merged with inverse source based BCI. The impact of using more detailed models to generate the lead-field matrix on inverse solutions can be studied in real scenarios.

- The application of projectors on the PMCHWT formulation can be studied to develop a new preconditioner based on the hierarchical preconditioner presented. The projectors allow to compute the global loops in an indirect fashion, which speeds up the preconditioner computation. A complete theoretical analysis on hierarchical projectors should be studied to create a well-grounded strategy.

- The new 2D framework for electromagnetic formulations will be the starting point of future research. The aim is to study complex structures and different 2D formulations used for biological tissues.

List of Publications

Journal Contributions

- John Erick Ortiz Guzman, Simon Adrian, Rajendra Mitharwal, Yves Beghein, Thomas Eibert, Kristof Cools, Francesco Andriulli, ”On the Hierarchical Preconditioning of the PMCHWT Integral Equation on Simply and Multiply Connected Geometries”, *IEEE Antennas and Wireless Propagation Letters*

- John Erick Ortiz Guzman, Axelle Pillain, Lyes Rahmouni, Francesco Andriulli, ”A Calderon Regularized Symmetric Formulation for the EEG Forward Problem”, *Submitted*

Conference Contributions

- John Eric Ortiz Guzman, Axelle Pillain, Lyes Rahmouni, and Francesco P. Andriulli, ”On the Preconditioning of the Symmetric Formulation for the EEG Forward Problem by Leveraging on Calderon Formulas”, *Biomedical Imaging (ISBI), 2016 IEEE 13th International Symposium. IEEE, 2016.*

- John Erick Ortiz Guzman, Simon Adrian, Rajendra Mitharwal, Yves Beghein, Thomas Eibert, Kristof Cools, Francesco Andriulli, ”Hierarchical Basis Preconditioners and Their Application to the PMWCHT Integral Equation”, *2016 10th European Conference on Antennas and Propagation (EuCAP)*

Bibliography

[1] Zeynep Akalin Acar and Scott Makeig. Effects of forward model errors on EEG source localization. *Brain topography*, 26(3):378–396, 2013.

[2] Geoffray Adde, Maureen Clerc, Olivier Faugeras, Renaud Keriven, Jan Kybic, and Théodore Papadopoulo. Symmetric BEM formulation for the M/EEG forward problem. In *Information Processing in Medical Imaging*, pages 524–535. Springer, 2003.

[3] Seppo P Ahlfors, Jooman Han, John W Belliveau, and Matti S Hämäläinen. Sensitivity of MEG and EEG to source orientation. *Brain topography*, 23(3):227–232, 2010.

[4] F.P. Andriulli. Loop-Star and Loop-Tree Decompositions: Analysis and Efficient Algorithms. *IEEE Transactions on Antennas and Propagation*, 60(5):2347–2356, May 2012.

[5] Francesco P. Andriulli, K. Cools, I. Bogaert, and E. Michielssen. On a Well-Conditioned Electric Field Integral Operator for Multiply Connected Geometries. *IEEE Transactions on Antennas and Propagation*, 61(4):2077–2087, April 2013.

[6] Francesco P. Andriulli, Kristof Cools, Hakan Bagci, Femke Olyslager, Annalisa Buffa, Snorre Christiansen, and Eric Michielssen. A Multiplicative Calderon Preconditioner for the Electric Field Integral Equation. *IEEE Transactions on Antennas and Propagation*, 56(8):2398–2412, August 2008.

[7] Francesco P Andriulli, Kristof Cools, Ignace Bogaert, and Eric Michielssen. On a well-conditioned electric field integral operator for multiply connected geometries. *IEEE transactions on antennas and propagation*, 61(4):2077–2087, 2013.

[8] Francesco P. Andriulli, Anita Tabacco, and Giuseppe Vecchi. Solving the EFIE at Low Frequencies with a Conditioning That Grows Only Logarithmically with the Number of Unknowns. *IEEE Transactions on Antennas and Propagation*, 58(5):1614–1624, May 2010.

[9] O Axelson. Iterative solution methods. 1996.

[10] Ümit Aydin, Johannes Vorwerk, Philipp Küpper, Marcel Heers, Harald Kugel, Andreas Galka, Laith Hamid, Jörg Wellmer, Christoph Kellinghaus, Stefan Rampp, et al. Combining EEG and MEG for the reconstruction of epileptic activity using a calibrated realistic volume conductor model. *PloS one*, 9(3):e93154, 2014.

[11] Mario Bebendorf. Approximation of boundary element matrices. *Numerische Mathematik*, 86(4):565–589, 2000.

[12] Annalisa Buffa and Snorre Christiansen. A dual finite element complex on the barycentric refinement. *Mathematics of Computation*, 76(260):1743–1769, 2007.

[13] Ru-Shan Chen, Jianjun Ding, D.Z. Ding, Z.H. Fan, and Daoxiang Wang. A Multiresolution Curvilinear Rao-Wilton-Glisson Basis Function for Fast Analysis of Electromagnetic Scattering. *IEEE Transactions on Antennas and Propagation*, 57(10):3179–3188, 2009.

[14] Siyuan Y. Chen, Weng Cho Chew, Jiming M. Song, and Jun-Sheng Zhao. Analysis of Low Frequency Scattering from Penetrable Scatterers. *IEEE Transactions on Geoscience and Remote Sensing*, 39(4):726–735, 2001.

[15] Jae-Hyun Cho, Johannes Vorwerk, Carsten H Wolters, and Thomas R Knösche. Influence of the head model on EEG and MEG source connectivity analyses. *Neuroimage*, 110:60–77, 2015.

[16] CJ Chu, N Tanaka, J Diaz, BL Edlow, O Wu, M Hämäläinen, S Stufflebeam, SS Cash, and MA Kramer. EEG functional connectivity is partially predicted by underlying white matter connectivity. *NeuroImage*, 108:23–33, 2015.

[17] K. Cools, F.P. Andriulli, F. Olyslager, and E. Michielssen. Nullspaces of MFIE and Calderón Preconditioned EFIE Operators Applied to Toroidal Surfaces. *IEEE Transactions on Antennas and Propagation*, 57(10):3205–3215, October 2009.

[18] Kristof Cools, Francesco P Andriulli, Femke Olyslager, and Eric Michielssen. Improving the MFIE's accuracy by using a mixed discretization. In *2009 IEEE Antennas and Propagation Society International Symposium*, pages 1–4. IEEE, 2009.

[19] B Neil Cuffin. EEG localization accuracy improvements using realistically shaped head models. *Biomedical Engineering, IEEE Transactions on*, 43(3):299–303, 1996.

[20] Sarang S Dalal, Johanna M Zumer, Adrian G Guggisberg, Michael Trumpis, Daniel DE Wong, Kensuke Sekihara, and Srikantan S Nagarajan. MEG/EEG source reconstruction, statistical evaluation, and visualization with NUTMEG. *Computational intelligence and neuroscience*, 2011, 2011.

[21] Moritz Dannhauer, Benjamin Lanfer, Carsten H Wolters, and Thomas R Knösche. Modeling of the human skull in EEG source analysis. *Human brain mapping*, 32(9):1383–1399, 2011.

[22] JC De Munck. The potential distribution in a layered anisotropic spheroidal volume conductor. *Journal of applied Physics*, 64(2):464–470, 1988.

[23] Florian Drechsler, Carsten H Wolters, Thomas Dierkes, Hang Si, and Lars Grasedyck. A full subtraction approach for finite element method based source analysis using constrained delaunay tetrahedralisation. *NeuroImage*, 46(4):1055–1065, 2009.

[24] M.A. Francavilla, M. Righero, G. Vecchi, and F. Vipiana. On dealing with low frequency problems using MoM and dielectrics in a simplified IEMI scenario. In *2014 International Symposium on Electromagnetic Compatibility (EMC Europe)*, pages 1228–1231, September 2014.

[25] Ann Franchois and Christian Pichot. Microwave imaging-complex permittivity reconstruction with a levenberg-marquardt method. *IEEE Transactions on Antennas and Propagation*, 45(2):203–215, 1997.

[26] Johan HM Frijns, Sander L De Snoo, and Ruurd Schoonhoven. Improving the accuracy of the boundary element method by the use of second-order interpolation functions [EEG modeling application]. *Biomedical Engineering, IEEE Transactions on*, 47(10):1336–1346, 2000.

[27] Manfred Fuchs, Ralf Drenckhahn, Hans-Aloys Wischmann, and Michael Wagner. An improved boundary element method for realistic volume-conductor modeling. *Biomedical Engineering, IEEE Transactions on*, 45(8):980–997, 1998.

[28] Manfred Fuchs, Michael Wagner, and Jörn Kastner. Boundary element method volume conductor models for EEG source reconstruction. *Clinical neurophysiology*, 112(8):1400–1407, 2001.

[29] M Gavaret, L Maillard, and J Jung. High-resolution EEG (HR-EEG) and magnetoencephalography (MEG). *Neurophysiologie Clinique/Clinical Neurophysiology*, 45(1):105–111, 2015.

[30] Nevzat G Gençer and Can E Acar. Sensitivity of EEG and MEG measurements to tissue conductivity. *Physics in medicine and biology*, 49(5):701, 2004.

[31] Alexandre Gramfort, Théodore Papadopoulo, Emmanuel Olivi, Maureen Clerc, et al. OpenMEEG: opensource software for quasistatic bioelectromagnetics. *Biomed. Eng. Online*, 9(1):45, 2010.

[32] Roberta Grech, Tracey Cassar, Joseph Muscat, Kenneth P Camilleri, Simon G Fabri, Michalis Zervakis, Petros Xanthopoulos, Vangelis Sakkalis, and Bart Vanrumste. Review on solving the inverse problem in EEG source analysis. *Journal of neuroengineering and rehabilitation*, 5(1):25, 2008.

[33] Wolfgang Hackbusch. *Hierarchical matrices: algorithms and analysis*, volume 49. Springer, 2015.

[34] Hans Hallez, Bart Vanrumste, Roberta Grech, Joseph Muscat, Wim De Clercq, Anneleen Vergult, Yves D'Asseler, Kenneth P Camilleri, Simon G Fabri, Sabine Van Huffel, et al. Review on solving the forward problem in EEG source analysis. *Journal of neuroengineering and rehabilitation*, 4(1):46, 2007.

[35] Matti S Hamalainen and Jukka Sarvas. Realistic conductivity geometry model of the human head for interpretation of neuromagnetic data. *Biomedical Engineering, IEEE Transactions on*, 36(2):165–171, 1989.

[36] David K Hammond, Benoit Scherrer, and Simon K Warfield. Cortical graph smoothing: a novel method for exploiting dwi-derived anatomical brain connectivity to improve EEG source estimation. *Medical Imaging, IEEE Transactions on*, 32(10):1952–1963, 2013.

[37] Roger F Harrington and Jan L Harrington. *Field computation by moment methods*. Oxford University Press, 1996.

[38] Jens Haueisen, Ceon Ramon, Michael Eiselt, Hartmut Brauer, and Hannes Nowak. Influence of tissue resistivities on neuromagnetic fields and electric potentials studied with a finite element model of the head. *IEEE Transactions on Biomedical Engineering*, 44(8):727–735, 1997.

[39] Harold V Henderson and Shayle R Searle. On deriving the inverse of a sum of matrices. *Siam Review*, 23(1):53–60, 1981.

[40] Ralf Hiptmair. Operator preconditioning. *Computers and mathematics with Applications*, 52(5):699–706, 2006.

[41] Jian-Ming Jin. *Theory and computation of electromagnetic fields*. John Wiley & Sons, 2011.

[42] Jian-Ming Jin. *Theory and Computation of Electromagnetic Fields*. John Wiley & Sons, Inc, Hoboken, New Jersey, 2015.

[43] Viktor K Jirsa, Kelly J Jantzen, Armin Fuchs, and J Kelso. Spatiotemporal forward solution of the EEG and MEG using network modeling. *Medical Imaging, IEEE Transactions on*, 21(5):493–504, 2002.

[44] J. Kybic, M. Clerc, T. Abboud, O. Faugeras, R. Keriven, and T. Papadopoulo. A common formalism for the Integral formulations of the forward EEG problem. 24(1):12–28.

[45] Jan Kybic, Maureen Clerc, Toufic Abboud, Olivier Faugeras, Renaud Keriven, and Théo Papadopoulo. A common formalism for the integral formulations of the forward EEG problem. *Medical Imaging, IEEE Transactions on*, 24(1):12–28, 2005.

[46] Jan Kybic, Maureen Clerc, Olivier Faugeras, Renaud Keriven, and Théo Papadopoulo. Fast multipole acceleration of the MEG/EEG boundary element method. 50(19):4695–4710.

[47] Y Lai, W Van Drongelen, L Ding, KE Hecox, VL Towle, DM Frim, and B He. Estimation of in vivo human brain-to-skull conductivity ratio from simultaneous extra-and intra-cranial electrical potential recordings. *Clinical neurophysiology*, 116(2):456–465, 2005.

[48] Seok Lew, Carsten H. Wolters, Alfred Anwander, Scott Makeig, and Rob S. MacLeod. Improved EEG source analysis using low-resolution conductivity estimation in a four-compartment finite element head model. *Human Brain Mapping*, 30, 2009.

[49] Gildas Marin, Christophe Guerin, Sylvain Baillet, Line Garnero, and Gérard Meunier. Influence of skull anisotropy for the forward and inverse problem in EEG: simulation studies using fem on realistic head models. *Human brain mapping*, 6(4):250–269, 1998.

[50] Joseph R Mautz and Roger F Harrington. Electromagnetic scattering from a homogeneous material body of revolution. *Archiv Elektronik und Uebertragungstechnik*, 33:71–80, 1979.

[51] Christoph M Michel and Micah M Murray. Towards the utilization of EEG as a brain imaging tool. *Neuroimage*, 61(2):371–385, 2012.

[52] Rajendra Mitharwal and Francesco P Andriulli. A regularised boundary element formulation for contactless sar evaluations within homogeneous and inhomogeneous head phantoms. *Comptes Rendus Physique*, 16(9):776–788, 2015.

[53] Victoria Montes-Restrepo, Pieter van Mierlo, Gregor Strobbe, Steven Staelens, Stefaan Vandenberghe, and Hans Hallez. Influence of skull modeling approaches on EEG source localization. *Brain topography*, 27(1):95–111, 2014.

[54] P.L. Nunez and R. Srinivasan. *Electric Fields of the Brain: The Neurophysics of EEG*. Oxford University Press, 2006.

[55] Robert Oostenveld, Pascal Fries, Eric Maris, and Jan-Mathijs Schoffelen. FieldTrip: open source software for advanced analysis of MEG, EEG, and invasive electrophysiological data. *Computational intelligence and neuroscience*, 2011, 2010.

[56] Robert Oostenveld and Thom F Oostendorp. Validating the boundary element method for forward and inverse EEG computations in the presence of a hole in the skull. *Human brain mapping*, 17(3):179–192, 2002.

[57] John Erick Ortiz, Axelle Pillain Lyes Rahmouni, and Francesco P. Andriulli. On the preconditioning of the symmetric formulation for the EEG forward problem by leveraging on calderon formulas. In *To be presented at IEEE International Symposium on Biomedical Imaging April 2016, Praque*.

[58] James W Phillips, Richard M Leahy, and John C Mosher. MEG-based imaging of focal neuronal current sources. *Medical Imaging, IEEE Transactions on*, 16(3):338–348, 1997.

[59] Joel R Phillips and Jacob K White. A precorrected-fft method for electrostatic analysis of complicated 3-d structures. *IEEE Transactions on Computer-Aided Design of Integrated Circuits and Systems*, 16(10):1059–1072, 1997.

[60] Axelle Pillain. *Line, Surface, and Volume Integral Equations for the Electromagnetic Modelling of the Electroencephalography Forward Problem*. PhD thesis, 2016. Thèse

de doctorat dirigée par Andriulli, Francesco Paolo Sciences de l'Ingénieur Télécom Bretagne 2016.

[61] Chris Plummer, A Simon Harvey, and Mark Cook. EEG source localization in focal epilepsy: where are we now? *Epilepsia*, 49(2):201–218, 2008.

[62] Ceon Ramon, P Schimpf, J Haueisen, M Holmes, and A Ishimaru. Role of soft bone, csf and gray matter in EEG simulations. *Brain topography*, 16(4):245–248, 2004.

[63] Michael Rullmann, Alfred Anwander, Moritz Dannhauer, Simon K Warfield, Frank H Duffy, and Carsten H Wolters. EEG source analysis of epileptiform activity using a 1 mm anisotropic hexahedra finite element head model. *NeuroImage*, 44(2):399–410, 2009.

[64] Jukka Sarvas. Basic mathematical and electromagnetic concepts of the biomagnetic inverse problem. *Physics in medicine and biology*, 32(1):11, 1987.

[65] Stefan A Sauter and Christoph Schwab. *Boundary element methods*. Springer, 2011.

[66] Uwe Schmitt, Alfred K Louis, Felix Darvas, Helmut Buchner, and Manfred Fuchs. Numerical aspects of spatio-temporal current density reconstruction from EEG-/MEG-data. *IEEE Trans. Med. Imaging*, 20(4):314–324, 2001.

[67] Jasmine Song, Colin Davey, Catherine Poulsen, Phan Luu, Sergei Turovets, Erik Anderson, Kai Li, and Don Tucker. EEG source localization: Sensor density and head surface coverage. 256:9–21.

[68] Jiming Song, Cai-Cheng Lu, and Weng Cho Chew. Multilevel fast multipole algorithm for electromagnetic scattering by large complex objects. *IEEE Transactions on Antennas and Propagation*, 45(10):1488–1493, 1997.

[69] Olaf Steinbach. *Numerical approximation methods for elliptic boundary value problems: finite and boundary elements*. Springer Science & Business Media, 2007.

[70] Matthew B Stephanson and Jin-Fa Lee. Preconditioned electric field integral equation using calderon identities and dual loop/star basis functions. *IEEE Transactions on Antennas and Propagation*, 57(4):1274–1279, 2009.

[71] François Tadel, Sylvain Baillet, John C Mosher, Dimitrios Pantazis, and Richard M Leahy. Brainstorm: a user-friendly application for MEG/EEG analysis. *Computational intelligence and neuroscience*, 2011:8, 2011.

[72] Federica Vatta, Fabio Meneghini, Fabrizio Esposito, Stefano Mininel, and Francesco Di Salle. Realistic and spherical head modeling for EEG forward problem solution: a comparative cortex-based analysis. *Computational intelligence and neuroscience*, 2010:13, 2010.

[73] G. Vecchi. Loop-Star Decomposition of Basis Functions in the Discretization of the EFIE. *IEEE Transactions on Antennas and Propagation*, 47(2):339–346, February 1999.

[74] Johannes Vorwerk, Jae-Hyun Cho, Stefan Rampp, Hajo Hamer, Thomas R Knösche, and Carsten H Wolters. A guideline for head volume conductor modeling in EEG and MEG. *NeuroImage*, 100:590–607, 2014.

[75] J Vorwerk[1], M Clerc, M Burger, and CH Wolters[1]. Comparison of boundary element and finite element approaches to the EEG forward problem. *Biomed Tech*, 57:1, 2012.

[76] Chao-Fu Wang, Feng Ling, Jiming Song, and Jian-Ming Jin. Adaptive integral solution of combined field integral equation. *Microwave and Optical Technology Letters*, 19(5):321–328, 1998.

[77] David Weinstein, Leonid Zhukov, and Chris Johnson. Lead-field bases for electroencephalography source imaging. *Annals of biomedical engineering*, 28(9):1059–1065, 2000.

[78] Carsten Hermann Wolters, Alfred Anwander, X Tricoche, D Weinstein, Martin A Koch, and Robert S Macleod. Influence of tissue conductivity anisotropy on EEG/MEG field and return current computation in a realistic head model: a simulation and visualization study using high-resolution finite element modeling. *NeuroImage*, 30(3):813–826, 2006.

[79] Su Yan, Jian-Ming Jin, and Zaiping Nie. Efie analysis of low-frequency problems with loop-star decomposition and calderón multiplicative preconditioner. *IEEE Transactions on Antennas and Propagation*, 58(3):857–867, 2010.

[80] B Yvert, O Bertrand, M Thevenet, JF Echallier, and J Pernier. A systematic evaluation of the spherical model accuracy in EEG dipole localization. *Electroencephalography and clinical neurophysiology*, 102(5):452–459, 1997.

[81] Yingchun Zhang, Wim van Drongelen, and Bin He. Estimation of in vivo brain-to-skull conductivity ratio in humans. *Applied physics letters*, 89(22):223903, 2006.

[82] Zhi Zhang. A fast method to compute surface potentials generated by dipoles within multilayer anisotropic spheres. *Physics in medicine and biology*, 40(3):335, 1995.

[83] K. Zhao, M.N. Vouvakis, and J.-F. Lee. The Adaptive Cross Approximation Algorithm for Accelerated Method of Moments Computations of EMC Problems. *IEEE Transactions on Electromagnetic Compatibility*, 47(4):763–773, November 2005.

[84] Kezhong Zhao, Marinos N Vouvakis, and Jin-Fa Lee. The adaptive cross approximation algorithm for accelerated method of moments computations of emc problems. *IEEE transactions on electromagnetic compatibility*, 47(4):763–773, 2005.

Résumé

Cette thèse présente plusieurs nouvelles techniques pour la convergence rapide des solutions aux éléments de frontière de problèmes électromagnétiques. Une attention spéciale a été dédiée aux formulations pertinentes pour les solutions aux problèmes électromagnétiques dans les tissus biologiques à haute et basse fréquence. Pour les basses fréquences, de nouveaux schémas pour préconditionner et accélérer le problème direct de l'électroencéphalographie sont présentés dans cette thèse. La stratégie de régularisation repose sur une nouvelle formule de Calderon, obtenue dans cette thèse, alors que l'accélération exploite le paradigme d'approximation adaptive croisée (ACA). En ce qui concerne le régime haute fréquence, en vue d'applications de dosimétrie, l'attention de ce travail a été concentrée sur l'étude de la régularisation de l'équation intégrale de Poggio-Miller-Chang-Harrington-Wu-Tsai (PMCHWT) à l'aide de techniques hiérarchiques. Le travail comprend une analyse complète de l'équation pour des géométries simplement et non-simplement connectées. Cela a permis de concevoir une nouvelle stratégie de régularisation avec une base hiérarchique permettant d'obtenir une équation pour les milieux pénétrable stable pour un large spectre de fréquence. Un cadre de travail propédeutique de discrétisation et une bibliothèque de calcul pour des thèmes de recherches sur les techniques de Calderon en 2D sont proposés en dernière partie de cette thèse. Cela permettra d'étendre nos recherches à l'imagerie par tomographie.

Mots clefs : Equations intégrales, électroencéphalographie, électromagnétisme numérique

Abstract

This thesis presents several new techniques for rapidly converging boundary element solutions of electromagnetic problems. A special focus has been given to formulations that are relevant for electromagnetic solutions in biological tissues both at low and high frequencies. More specifically, as pertains the low-frequency regime, this thesis presents new schemes for preconditioning and accelerating the Forward Problem in Electroencephalography (EEG). The regularization strategy leveraged on a new Calderon formula, obtained in this thesis work, while the acceleration leveraged on an Adaptive-Cross-Approximation paradigm. As pertains the higher frequency regime, with electromagnetic dosimetry applications in mind, the attention of this work focused on the study and regularization of the Poggio-Miller-Chang-Harrington-Wu-Tsai (PMCHWT) integral equation via hierarchical techniques. In this effort, a complete analysis of the equation for both simply and non-simply connected geometries has been obtained. This allowed to design a new hierarchical basis regularization strategy to obtain an equation for penetrable media which is stable in a wide spectrum of frequencies. A final part of this thesis work presents a propaedeutic discretization framework and associated computational library for 2D Calderon research which will enable our future investigations in tomographic imaging.

Keywords: Integral Equations, Electroencephalography, Computational Electromagnetics

N° d'ordre : 2017IMTA0051

IMT Atlantique
Bretagne-Pays de la Loire
École Mines-Télécom

IMT Atlantique Bretagne-Pays de la Loire - www.imt-atlantique.fr

Campus de Brest
Technopôle Brest-Iroise
CS 83818
29238 Brest Cedex 03
T +33 (0)2 29 00 11 11
F +33 (0)2 29 00 10 00

Campus de Nantes
4, rue Alfred Kastler - La Chantrerie
CS 20722
44307 Nantes Cedex 3
T +33 (0)2 51 85 81 00
F +33 (0)2 51 85 81 99

Campus de Rennes
2, rue de la Châtaigneraie
CS 17607
35576 Cesson Sévigné Cedex
T +33 (0)2 99 12 70 00
F +33 (0)2 99 12 70 08